Galactic disc dynamics in the Gaia era : perturbed distribution functions in the presence of non-axisymmetries

Hussein Al Kazwini

Université de Strasbourg

UNIVERSITÉ DE STRASBOURG

ÉCOLE DOCTORALE ED182

UMR 7550

THÈSE présentée par :

Hussein AL KAZWINI

soutenue le : **27 Septembre 2022**

pour obtenir le grade de : **Docteur de l'université de Strasbourg**

Discipline/ Spécialité : Astrophysique

Dynamique du disque galactique à l'ère de Gaïa

THÈSE dirigée par :

M. FAMAEY Benoit	Dr., université de Strasbourg (Invité)

RAPPORTEURS :

Mme VARRI Anna-Lisa	Dr., Université d'Edinburgh
Mme D'ONGHIA Elena	Dr., Université de Wisconsin–Madison

AUTRES MEMBRES DU JURY :

M. BOILY Christian	Dr., université de Strasbourg
M. BIENAYME Olivier	Dr., université de Strasbourg

UNIVERSITY OF STRASBOURG

Abstract

Astronomical Observatory of Strasbourg

Doctor of Philosophy

Galactic disc dynamics in the Gaia era: perturbed distribution functions in the presence of non-axisymmetries

by Hussein Al Kazwini

Cette thèse se proposait d'établir des modèles dynamiques de la Voie lactée, en prenant en compte les perturbations de son disque stellaire. Les données récentes fournies par la mission Gaia appellent de nouvelles méthodes pour aborder ce problème: un cadre adéquat pour tester les modèles de la Galaxie, englobant la barre galactique et les bras spiraux, constitue l'objectif de ce travail théorique.

Je me suis attelé à recalculer l'ensemble des prédictions d'une fonction de distribution perturbées en six-dimensions dans l'espace des phases hors des zones résonnantes et en prédisant l'emplacement des zones résonnantes. Nous avons également considéré la réponse de la fonction de distribution dans le cadre d'une perturbation dépendante du temps. Mon résultat majeur est que j'ai pu montrer que les emplacements des résonances sont déplacés vers des vitesses azimutales plus faibles lorsque l'on s'éloigne dans le direction verticale du plan de la Galaxie, ce qu'on n'arrivait pas à bien prendre en compte dans l'approximation épicyclique. Ainsi, la position des groupes mobiles dans le plan des vitesses uv en fonction de la hauteur z au-dessus du plan Galactique peut être un moyen puissant de contraindre la structure 3D du potentiel Galactique ainsi que les résonances à l'origine de ces groupes mobiles observés.

Acknowledgements

First, I would like to send special and warm thanks to my family and my friends who were always present to provide much needed solace and respite during the course of the thesis and for all their love and support which helped to motivate me on this endeavour.

I would like to thank my thesis director, Benoit Famaey, for all his help. I am delighted to have worked with him because, in addition to his scientific support, he has been there to support and guide me during this thesis. I would like to thank Giacomo Monari, co-supervisor of the thesis, for his presence and his precious and indispensable help and for all the time he has given me during these three years.

I would like to thank Pierre-Alain Duc, director of the Strasbourg Astronomical Observatory, and the entire management and staff of the Observatory and all fellow researchers of the institute for their friendliness and hospitality and for providing an adequate environment for scientific research despite the sanitary crisis and all the hardships that were present during this period.

Finally, I would like to thank Anna Varri, Elena D'Onghia, Olivier Bienayme and Christian Boily for accepting to be on my comity and evaluate the work that I have done.

Contents

Abstract iii

Acknowledgements v

1 Introduction 1
- 1.1 Galaxies: Historical overview . . . 1
- 1.2 Milky Way Galaxy . . . 2
  - 1.2.1 Stellar halo . . . 4
  - 1.2.2 Dark halo . . . 6
  - 1.2.3 Disc . . . 6
  - 1.2.4 Stellar velocity fields in the disc . . . 7
  - 1.2.5 Bulge/Bar . . . 8
- 1.3 Kinetic theory of self-gravitating systems . . . 8
  - 1.3.1 Collisionless Boltzmann equation . . . 8
  - 1.3.2 Action-angle variables . . . 10
  - 1.3.3 Jeans theorem . . . 10
  - 1.3.4 Epicyclic approximation . . . 11
  - 1.3.5 Torus Mapping and Stäckel fudge . . . 12
- 1.4 Outline of the thesis . . . 14

2 Perturbing potential and perturbed distribution function 15
- 2.1 Perturbed distribution functions . . . 15
- 2.2 Perturbing potential in actions and angles . . . 17
- 2.3 Bar potential . . . 18
- 2.4 Spiral potential . . . 21

3 Linear perturbations with accurate action estimates 23
- 3.1 Background equilibrium . . . 23
- 3.2 Resonant zones . . . 25
- 3.3 Comparing the perturbed DF for different action estimates . . . 28

4 Temporal evolution of the perturber 33
- 4.1 Time-varying amplitude function . . . 33
- 4.2 Time-dependent perturbed distribution function . . . 33

5 Trapping at resonances with accurate action estimates 37

6 A first application: locating moving groups with Gaia EDR3 43

7 Bar-disc perturbations in backward integration simulation for comparisons with Gaia DR3 49

8 Published articles **55**

9 Conclusions **87**

Bibliography **89**

List of Figures

1.1 The Hubble Classification scheme for galaxies 3
1.2 The Hubble-De Vaucouleurs galaxy morphology diagram 3
1.3 Artistic conception of the spiral structure of the Milky Way with two major stellar arms and a bar 4
1.4 Model rotation curve from Sofue, Honma, and Omodaka, 2009 compared with the observations. Thin lines represent the bulge, disk + rings, and dark halo components, and the thick line is the composite rotation curve. Data are as follows. Open triangles: HI tangent velocity method (Burton and Gordon, 1978); Rectangles: CO tangent (Clemens, 1985); Reverse triangles: HI tangent (Fich, Blitz, and Stark, 1989); Diamonds: CO and HII regions (Fich, Blitz, and Stark, 1989; Blitz, Fich, and Stark, 1982); filled triangles: Demers and Battinelli, 2007; Circles: HI thickness (Honma and Sofue, 1997a; Honma and Sofue, 1997b); Big circle at 13.1 kpc: VERA-parallax, proper motion and velocity (Honma et al., 2007). All data have been converted to (R0 , V0) = (8.0, 200.0 km/s). 5
1.5 Velocity plane of the stars in the solar neighbourhood. A 2D histogram of the velocity is shown with a bin of $1 kms^{-1}$, thus, the colour scale indicates the number of stars per $(kms^{-1})^2$. 7
1.6 Representation of epicyclic motion. 13

2.1 Variations in a few Fourier coefficients $\phi_{jml}(\boldsymbol{J})$ of the bar potential from Sect. 2.4 as J_R or J_φ increase separately at $J_z = 0$. The actions on the abscissa axis are in kpc km s^{-1}. The curves are very smooth, which justifies our use of the cubic splines method to interpolate. . . 19
2.2 Accuracy of the reconstruction of the bar potential . Left panel (top): Estimate of the bar potential from Sect. 2.4 at the Sun's position in the plane with 41 complex Fourier coefficients in Eq. 2.10 and the reconstruction using cubic splines. The vertical line denotes the true value. The value in the top right inset denotes the true value in physical units. The potential is always estimated at the same configuration space location (within the plane, at the Sun's position) but for different velocities. Left panel (bottom): Relative accuracy compared to the maximum value of the bar potential at the Sun's radius denoted in the top right inset. Right panel: Same, but at $z = 0.3$ kpc with 231 complex Fourier coefficients. The typical accuracy is well below the per cent level, although with a slight bias towards lower amplitudes (i.e. $|\Phi_{\mathrm{b\,estimated}}| < |\Phi_{\mathrm{b\,input}}|$) above the plane. 20

2.3 Accuracy of the reconstruction of the spiral arms potential. Left panel (top): Estimate of the spiral arms potential from Sect. 2.5 at the Sun's position in the plane with 41 complex Fourier coefficients in Eq. 2.10 and the reconstruction using cubic splines. The vertical line denotes the true value. The value in the top right inset denotes the true value in physical units. The potential is always estimated at the same configuration space location (within the plane, at the Sun's position) but for different velocities. Left panel (bottom): Relative accuracy compared to the maximum value of the spiral arms potential at the Sun's radius denoted in the top right inset. Right panel: Same, but at $z = 0.3$ kpc with 231 complex Fourier coefficients. The typical accuracy is again well below the per cent level in the plane, while it is around the per cent level above the plane. 21

3.1 Local uv-plane stellar velocity distribution at axisymmetric equilibrium and for $w = 0$, from Eq. 3.1 at $(R, z, \varphi) = (R_0, 0, 0)$. Left panel: Epicyclic approximation in the plane (top) and at $z = 0.3$ kpc (bottom). Right panel: Stäckel fudge with `AGAMA` in the plane (top) and at $z = 0.3$ kpc (bottom). 24

3.2 Values of $\log(\omega_{s,jml})$ in the (J_R, J_φ) plane with fixed $J_z = 10$ kpc km s^{-1}, for a few combinations of (j, l) indices giving rise to resonant zones in action space (recalling that $m = 2$). The pattern speed Ω_p here is $1.89\,\Omega_0$. The two actions are renormalized by the radial velocity dispersion of the thin disc and the circular velocity at the Sun, respectively. The deep blue lines correspond to resonant zones. For instance, the $(1, 0)$ case corresponds to the traditional OLR (for a non-zero J_z). Most other low-order combinations of indices did not give rise to any relevant resonant zone in the region of interest. . . . 25

3.3 Values of $\log(\omega_{s,jml})$ in the (J_R, J_z) plane with fixed $J_\varphi = 1759$ kpc km s^{-1} for different (j, l) resonances. The pattern speed Ω_p is that of our fiducial central bar fixed at $1.89\,\Omega_0$. The two actions are renormalized by the radial velocity dispersion and the vertical velocity dispersion of the thin disc at the Sun, respectively. The deep blue lines correspond to resonance zones. Most combinations of indices explored did not give rise to any relevant resonant zone in the region of interest. 26

3.4 Values of $log(\omega_{s,jml})$ in the uw-plane and vw-plane. Top row: Values of $log(\omega_{s,jml})$ at $z = 0$ in the uw-plane with fixed $J_\varphi = 1759$ kpc km s^{-1}, for the various vertical resonances relevant in the solar neighbourhood (the $l = 0$ resonances are treated in detail in Sect. 3.3). They all appear at relatively large values of w and are very concentrated in w, varying very quickly in u as a function of w. Bottom row: Values of $log(\omega_{s,jml})$ in the vw-plane with fixed $u = 0$ km s^{-1}. The pattern speed Ω_p is that of our fiducial central bar fixed at $1.89\,\Omega_0$. . 26

3.5 Same as Fig. 3.2, but with some combinations of indices giving rise to resonant zones for $\Omega_p = 0.84\,\Omega_0$. 27

3.6 Same as Fig. 3.3, but with some combinations of indices giving rise to resonant zones for $\Omega_p = 0.84\,\Omega_0$. 27

3.7 Distribution function from Fig. 3.1 in velocity space at the solar position within the Galactic plane, now perturbed to linear order by a bar (perturbing potential from Sect. 2.4) with pattern speeds $\Omega_b = 1.16\,\Omega_0$ (left) and $\Omega_b = 1.89\Omega_0$ (middle), or by a spiral pattern (perturbing potential from Sect. 2.5) with pattern speed $\Omega_{sp} = 0.84\,\Omega_0$ (right). The black dashed contours represent the zones where k is equal to or less than 1, k being a quantity computed in Monari et al. (2017a) that designates the region where the orbits are trapped at the main resonance (the computation used here in the Stäckel case will be presented in detail in Al Kazwini et al., in preparation). Top row: Epicyclic approximation. Bottom row: Stäckel fudge. 29

3.8 Local stellar velocity distribution perturbed to linear order at the solar galactocentric radius and azimuth at three different heights (left: $z = 0$ kpc, middle: $z = 0.3$ kpc, right: $z = 1$ kpc), when perturbed by a bar (perturbing potential of Sect. 2.4) with pattern speed $\Omega_b = 1.89\Omega_0$. Top row: Epicyclic approximation. Bottom row: Stäckel fudge. The scale of the colour bar is different in the upper and lower panels for $z = 1$ kpc. 29

3.9 Same as Fig. 3.8, in the Stäckel fudge case, but now for joint perturbation by a bar (perturbing potential of Sect. 2.4) with pattern speed $\Omega_b = 1.89\Omega_0$ and a spiral pattern (perturbing potential of Sect. 2.5) with pattern speed $\Omega_{sp} = 0.84\,\Omega_0$. 30

4.1 Local stellar velocity distribution perturbed to linear order in the Galactic plane by the bar of Sect. 2.4 with $\Omega_b = 1.89\Omega_0$ with the Stäckel fudge, and an amplitude of the bar growing as described in Sect. 4.1. The first 11 panels display the temporal evolution of the perturbation. The last panel displays the stationary case. The amplitude of the bar goes from 0 at $t = 0$ to its plateau ($g(t) = 1$) at $t = 0.5$ Gyr. 35

5.1 Constant distribution function contours at $R = 8\ kpc$ and at $\phi = 30°$ for the Outer Lindblad resonance (l = 1) in the epicyclic approximation. 40

5.2 The same as above in the AGAMA case. 41

6.1 Moving group detection in different neighbourhoods along the radial direction. For each moving group, we include a parabolic fitting of the substructures associated with each group in a thick grey line. Each moving group contains several structures, corresponding to different V_R bins. The largest structure in each group is used as its representative (dots with larger black contours and the moving group name on top). 44

6.2 Moving group detection in different neighbourhoods along the radial direction in the simulations, analog to Fig. 6.1. Top row: fast bar model. Bottom row: slow bar model. 45

6.3 Azimuthal velocity of the kinematic substructures in the radial direction, $\phi = 0, Z = 0\,kpc$, as a function of the radius, and coloured by their radial velocity. The dashed grey lines correspond to constant angular momentum lines, crossing the moving groups at solar radius. Top: Structures corresponding to the main peak of a moving group, tagged with the name in literature. Bottom: Secondary peaks of the moving groups. The usual way to observe this projection is using the number of stars or the mean V_R in each bin. Using our methodology we can observe the skeleton of the distribution and its complexity. For instance, the slope of the moving groups at different V_R can be very different and the groups cross each other or share close regions in the diagram. In addition, the extension of the range of exploration shows that the moving group deviate from the constant vertical angular momentum predicted for small epicyclic amplitudes. 46

6.4 Azimuthal velocity of the kinematic substructures in the radial direction $(\phi = 0, Z = 0\,kpc)$ for the test particle simulations, as a function of the radius, and coloured by their radial velocity. We include dashed grey lines corresponding to constant angular momentum lines as a guide. Top: Structures for the fast bar model. Bottom: Structures for the slow bar model. In the fast bar model, we are able to detect substructures related to the OLR and the $1:1$ resonance, in the slow bar we only detect structures related with the OLR. With our methodology, we are able to show the complex morphology of the arches in a single image. 47

7.1 Rotation curve of the best model and range of model variations for evaluation of systematics on top of the composite rotation curve measurements from Sofue, Honma, and Omodaka, 2009. Blue, yellow and red curves represent respectively the baryonic, dark matter and total rotation curve, assuming that the totality of the additional central mass is baryonic. 50

7.2 Rotation curve of our fitted model. Yellow, green and blue curves represent respectively the baryonic, dark matter and total rotation curve. 51

7.3 Median radial velocity map generated from the Gaia data. The isovelocity contours $V_R = 0\,kms^{-1}$ are pointed out as black lines. . . . 52

7.4 Median radial velocity map generated from our simulation with contours of constant radial velocity. 53

Chapter 1

Introduction

1.1 Galaxies: Historical overview

Astronomy is one of the oldest natural sciences. Early civilisations (Babylonians, Egyptians, Greeks, etc.) observed the night sky for diverse purposes such as celestial navigation, calendar making and divination among others. Until the time of Copernicus, the earth was supposed to be the center of the Universe in what is known as the Ptolemaic system. According to this view, the planets, the Sun and the moon each move on its own sphere and the outermost is the sphere of the fixed stars beyond which nothing exists.

Although some of the ancients speculated about the existence of stellar systems beyond the sphere of fixed stars, it would not be until the twentieth century that proof is given of the extent of the Universe. The stars seen at night are only part of a vast galaxy, the Milky Way, and this galaxy in its turn is just one out of many scattered throughout space. The total number of galaxies in the observable universe is estimated to be $\sim 10^{11}$ and a typical galaxy contains $\sim 10^{11}$ stars.

This outstanding breakthrough was made by Edwin Hubble (Hubble, 1926a) who discovered that the spiral nebula M33 is a stellar system independent from the Milky Way. Hubble then went on to classify extra-galactic nebulae (Hubble, 1926b) in what is known as the Hubble sequence or Hubble classification. The Hubble sequence is a morphological classification system, i.e. galaxies are divided according to their visual appearance into three classes: ellipticals (E) with a number added after the letter to indicate the degree of ellipticity (E0 $\rightarrow$ E7), spirals (S) with a letter designating how tightly wound the spiral arms are (a, b or c) and a letter B inserted if it is barred (the bar is an elongated stellar component rotating at the center of the galaxy) and irregulars (Irr). Hubble then added a fourth class to mark the transition between ellipticals and spirals. Galaxies pertaining to this class are called lenticulars (S0).

De Vaucouleurs then extended the Hubble sequence arguing that it does not adequately describe the range of observed morphologies. He used the notation SA to designate spirals without bars and retained the notation SB for barred spirals. He introduced however the notation SAB to refer to weakly barred spirals. Galaxies that possess ring-like structures are denoted with the letter (r) and those that don't with the letter (s) and he accounted for those in transition with (rs). Three further denominations were added to account for the variety in the spiral arms shape (Sd to denote diffuse spiral galaxies, Sm to denote "Magellanic" spiral galaxies after the Large Magellanic Cloud and Im to denote irregular galaxies). The Large Magellanic Cloud is of type SBm and the Small Magellanic Cloud of type Im (Vaucouleurs and Pence, 1978).

Elliptical galaxies are smooth, featureless stellar systems with an approximately ellipsoidal shape. They show little to no stellar disk and they possess little to no interstellar gas. The absence of gas means that star formation has stopped and that the present stars in these systems are old and their age is comparable to that of the universe.

Spiral galaxies on the other hands are stellar systems that have a disk containing spiral arms which are density waves where stars are continually being formed. In fact, the interstellar gas often extends to much larger radii than the stellar component. By exploiting this feature, the circular velocity curves could be traced well beyond the optical edge of the galaxy. We find out that the circular speed curve is nearly flat out to the largest radii measured and not dropping as one would expect if most of the mass were in stars. This leads out to the natural conclusion that at these radii, the largest contributor to the mass in the galaxy is the dark halo. A prominent feature of spiral galaxies is the bulge which is a concentration of stars at the center with a smooth or amorphous appearance very much like that of ellipticals. While the bulge is supposed to be a separate stellar component from the disk, many observed bulges in barred galaxies are actually "pseudo-bulges" and are actually part of the bar structure itself.

Lenticular galaxies are a transition link between ellipticals and spirals. They resemble ellipticals inasmuch as they are smooth, featureless and possessing little to no gas. On the other hand, they have a disk feature and a bulge albeit without a spiral structure. It should be noted however that the transition between ellipticals and spirals is continuous and some of these lenticulars might well be classified as ellipticals or conversely as spirals.

Finally, irregular galaxies are stellar systems that do not show a well delineated spiral structure. They are extremely gas-rich. They include ellipticals and spirals that have been violently distorted as well as galaxies that are undergoing an outburst of star formation overshadowing the regular denotation of the galaxy.

1.2 Milky Way Galaxy

The Milky Way is the galaxy that contains the Solar system. It is called as such due to its appearance as a band of light in the night sky. It was Galileo Galilei who first resolved this band of light into distinct stars in 1610. The Milky Way is a barred spiral galaxy of type Sb or Sc. It is assigned the symbol SABbc in Vaucouleurs and Pence, 1978, i.e. it has an intermediate classification between Sb and Sc and a weak bar. The dynamical effects of this weak bar as well as of the spiral arms on the disk kinematics will be the main topic of this PhD thesis. Together with the Andromeda Galaxy and their respective satellites, the Milky Way forms the Local group of galaxies with a diameter of almost 3 Mpc. There is still much controversy concerning the structure of the Milky Way. It is estimated to contain $\sim 10^{11}$ stars and have a mass of $\sim 10^{12} M_{\odot}$ (Peñarrubia et al., 2014; Deason et al., 2019; McMillan, 2017). These quantities however are quite uncertain (Monari et al., 2018). Figure 1.4 shows the Milky Way rotation curve obtained over the years using different methods. If the mass of the Milky Way were due only to its stellar and gas components, then the rotation curve should be decreasing with distance whereas we find out that it is almost constant at high radii. We therefore conclude that, if General relativity holds

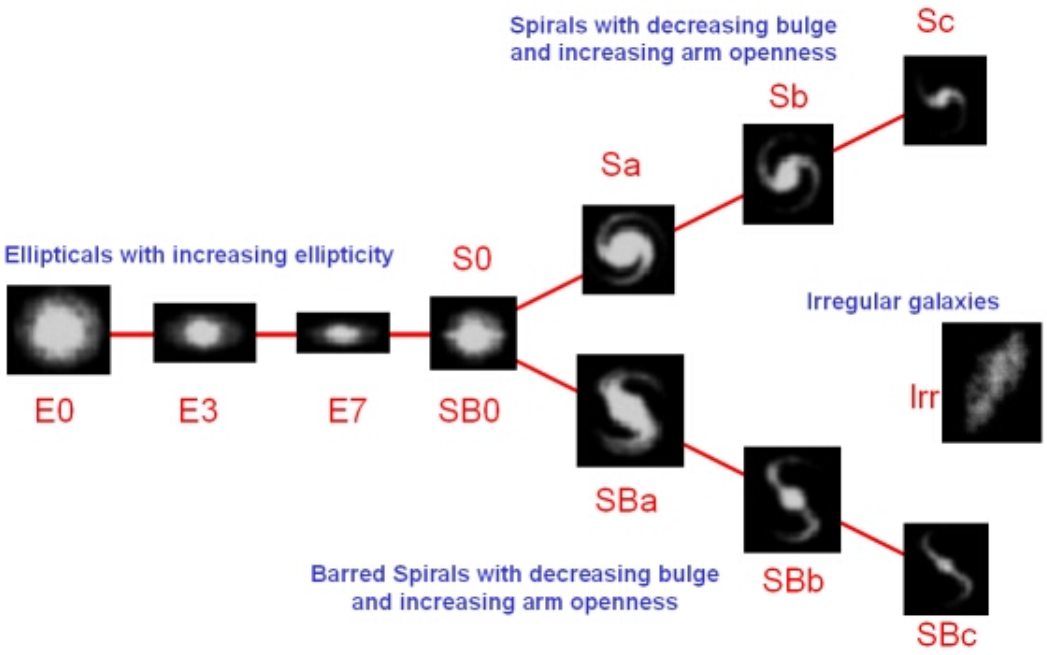

FIGURE 1.1: The Hubble Classification scheme for galaxies

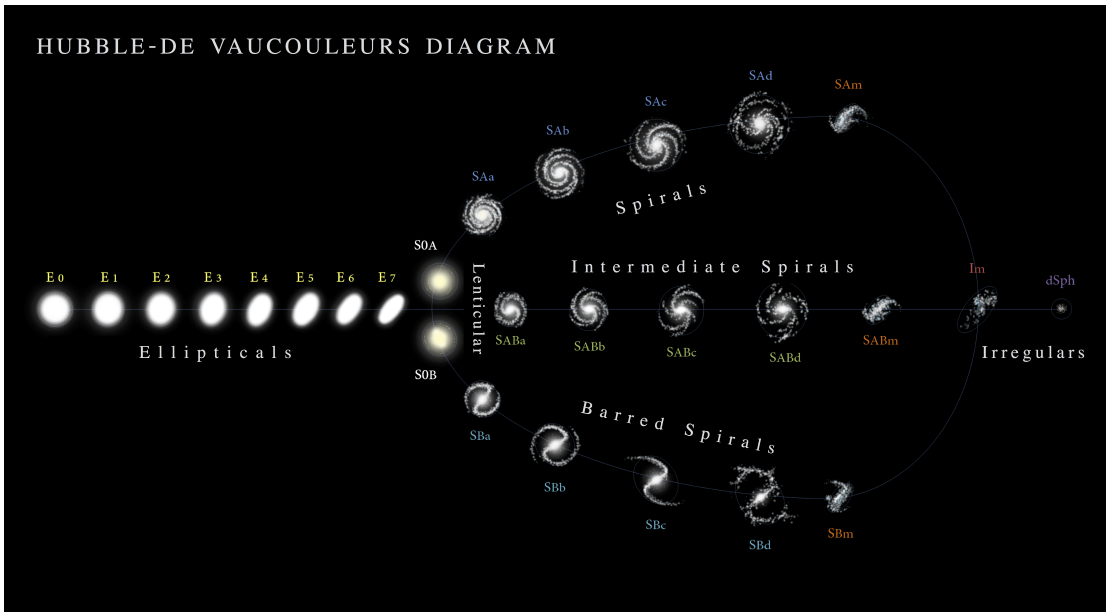

FIGURE 1.2: The Hubble-De Vaucouleurs galaxy morphology diagram

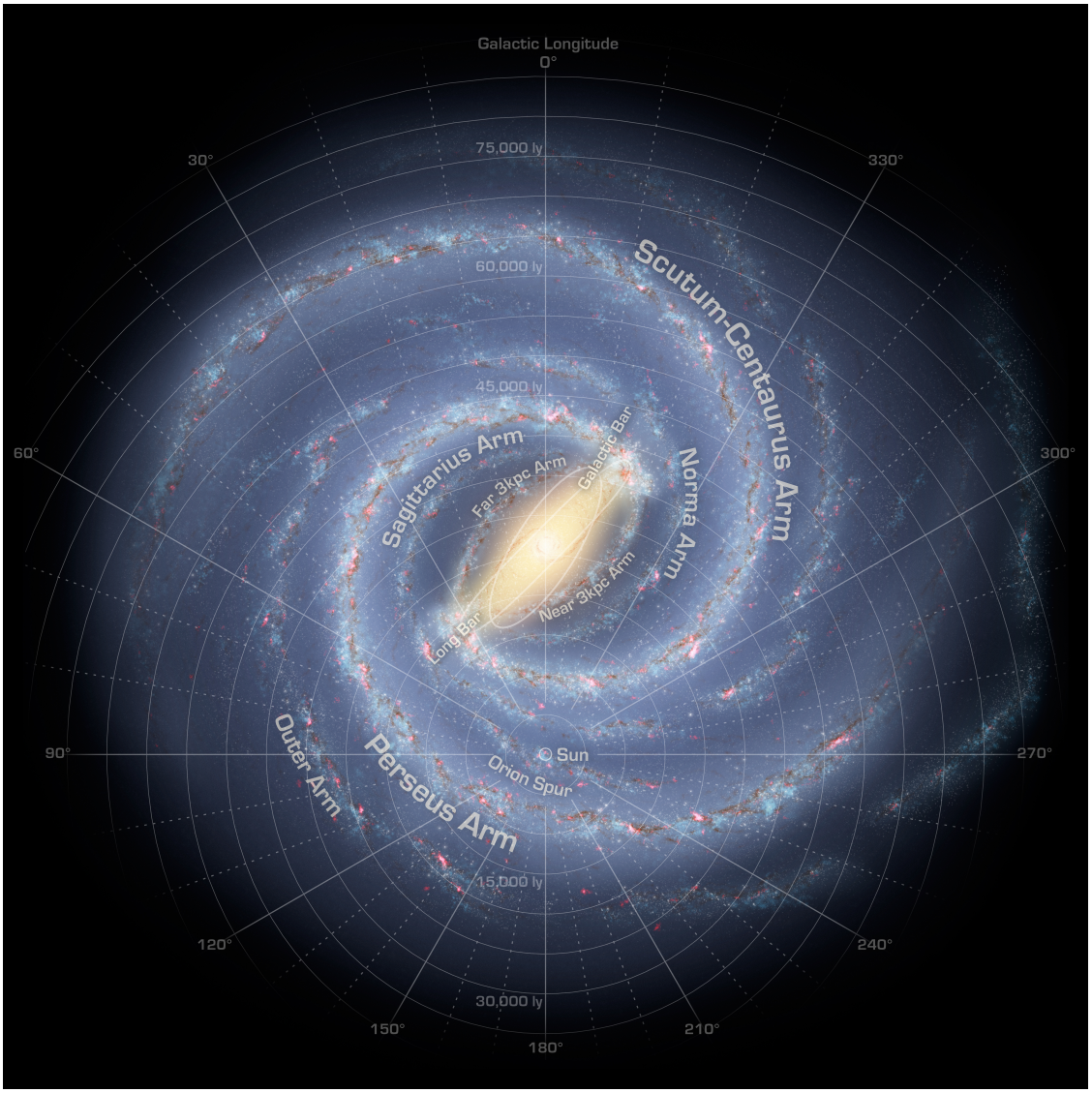

FIGURE 1.3: Artistic conception of the spiral structure of the Milky Way with two major stellar arms and a bar

(Famaey and McGaugh, 2012), the largest contributor to the mass of the Milky Way is dark matter. Besides the dark halo, the main components of the Milky Way are the bulge, the stellar halo and the thin and thick stellar disks.

1.2.1 Stellar halo

The Galaxy is surrounded with a spheroidal halo of old stars and globular clusters, most of which lie within 30 kpc from the Galactic Center. However, some have been found to lie at a distance of more than 100 kpc from the Galactic Center (Harris, 1996). Active star formation does not take place in the halo since there is little cold gas to collapse into stars. The halo is metal-poor with [Fe/H] $\sim$ -1.6 (Laird et al., 1988; Carollo et al., 2010) and contains of the order of 0.1-1% of the total stellar mass of the Milky Way (Cooper et al., 2010). Studies have decomposed the halo into two components: one inner region dominated by stars formed within the galaxy

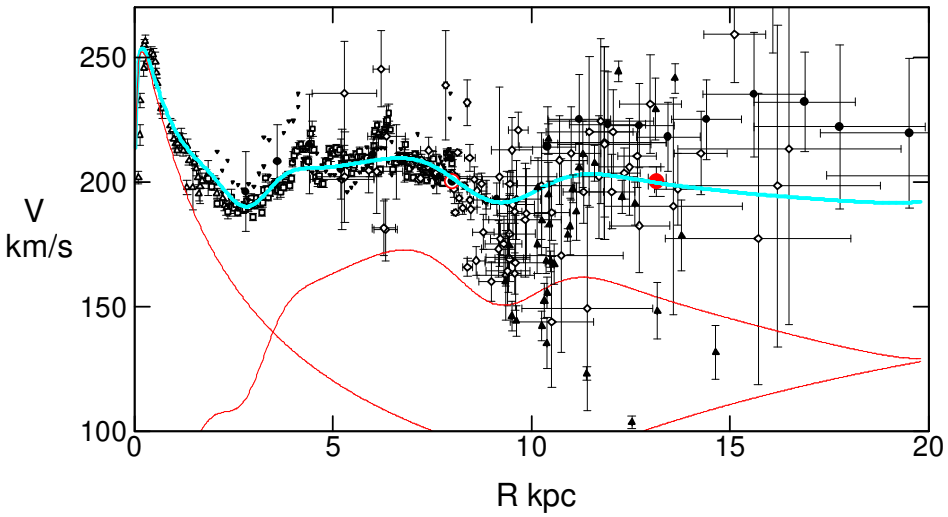

FIGURE 1.4: Model rotation curve from Sofue, Honma, and Omodaka, 2009 compared with the observations. Thin lines represent the bulge, disk + rings, and dark halo components, and the thick line is the composite rotation curve. Data are as follows. Open triangles: HI tangent velocity method (Burton and Gordon, 1978); Rectangles: CO tangent (Clemens, 1985); Reverse triangles: HI tangent (Fich, Blitz, and Stark, 1989); Diamonds: CO and HII regions (Fich, Blitz, and Stark, 1989; Blitz, Fich, and Stark, 1982); filled triangles: Demers and Battinelli, 2007; Circles: HI thickness (Honma and Sofue, 1997a; Honma and Sofue, 1997b); Big circle at 13.1 kpc: VERA-parallax, proper motion and velocity (Honma et al., 2007). All data have been converted to (R0 , V0) = (8.0, 200.0 km/s).

which could form a continuum with the thick disk and an outer region dominated by stars via accretion (McCarthy et al., 2012; Carollo et al., 2010; Helmi et al., 2018; Matteo et al., 2019; Naidu et al., 2020; Malhan et al., 2022). In addition to stars, X-ray observations gave evidence to the existence of a hot gas halo that extends to a radius over 100 kpc and well beyond the extent of the stellar halo. The mass of this halo is comparable to the total baryonic mass in the disk of the Galaxy (Gupta et al., 2012).

1.2.2 Dark halo

Besides the stellar halo, the Galaxy is embedded in a much larger roughly spherical halo of dark matter that reaches out as far as the halo of the Andromeda M31 galaxy. As stated before, the Milky Way rotation curve accounts for the existence of this halo (in case we do not adhere to the alternative theory of modified gravity to account for this feature). It appears that this dark matter does not interact with matter and energy in any way except gravity. Needless to say, current observation techniques have failed to detect dark matter. Monari et al., 2018 give estimations of $\sim 10^{12} M_{\odot}$ in mass of the dark matter.

1.2.3 Disc

It has been shown that the galactic disc is roughly axisymmetric (which means that non-axisymmetries can be treated by perturbation theory) with a radius of 15 to 20 kpc and consists of a thin disc with a dominant stellar mass and a second thicker disc (Gilmore and Reid, 1983). The scale height of the thick disc is between 600 pc and 1200 pc and contains 2-10% of the total local stellar mass (Pouliasis, Matteo, and Haywood, 2017). In comparison, the thin disc has a scale height of $\sim$ 300 pc (Recio-Blanco et al., 2014). According to Bensby et al., 2011, the scale length of the thick disc is shorter than that of the thin disc ($L_{thick} = 2kpc, L_{thin} = 3.8kpc$) but these values are still disputed. Robin et al., 2014 found a shorter scale height for the thick disc. The mass of the two disks is $\sim 5 * 10^{10} M\odot$.

Compared to the halo stars, those in the thin and thick discs have globally higher rotational velocities, of the order of 220 km/s for the stars in the solar neighbourhood. Because of the difference in height and age (Seabroke and Gilmore, 2007), the vertical velocity dispersion of the thick disc is greater ($\sim$ 40 km/s) than that of the thin disc ($\sim$ 20 km/s). The two discs are also distinguished by the nature of the stars that populate them. The stars in the thin disc are rich in metals (-0.5 < [Fe/H] < 0.5) and cover an age range of up to 8 billion years. The youngest stars are found in the spiral arms. The metallicity of the thick disk stars is lower (-2 < [Fe/H] < -0.3) for a population older than 10 billion years (Haywood et al., 2013). Furthermore, by comparing the metallicities of the two discs with their α abundance, it is possible to differentiate them clearly.

There is still uncertainty regarding the nature of the spiral arms and their number. Two spiral arms are traced by old stars whereas four spiral arms are traced by young ones (Drimmel, 2000; Urquhart et al., 2013). The reasons for these discrepancies are still unknown. There is further offset noted between stellar spiral arms and gas arms

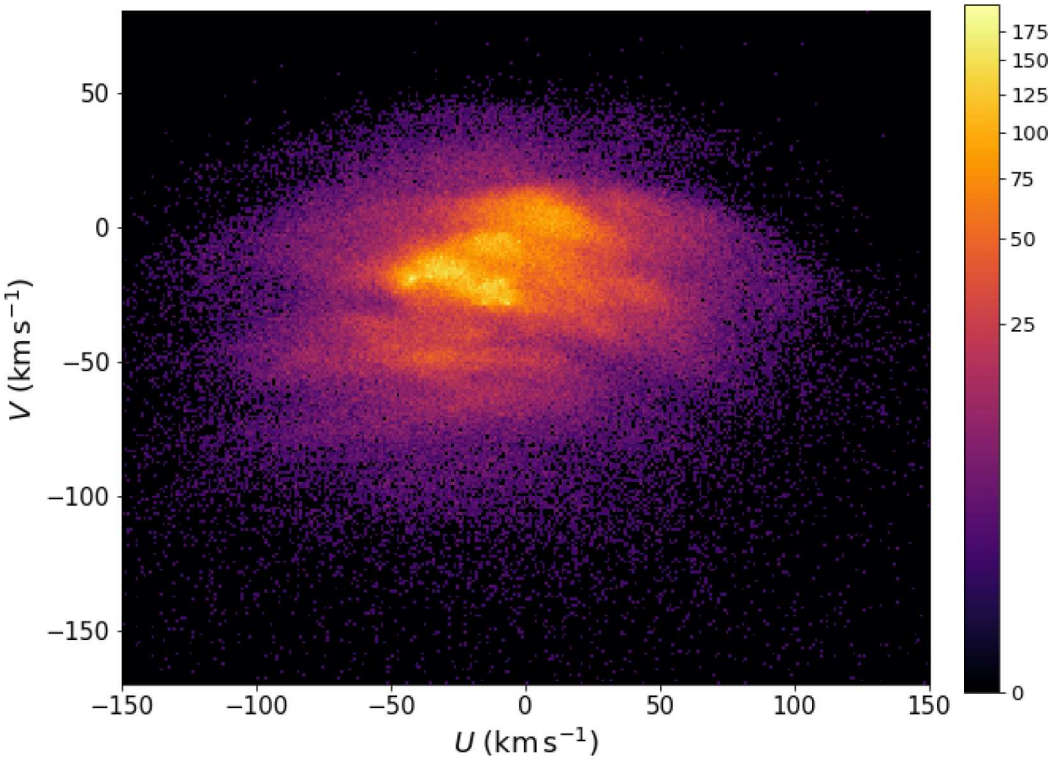

FIGURE 1.5: Velocity plane of the stars in the solar neighbourhood. A 2D histogram of the velocity is shown with a bin of $1 kms^{-1}$, thus, the colour scale indicates the number of stars per $(kms^{-1})^2$.

of the Milky Way as obvious displacements of gaseous bump peaks from the density peaks of old stars are detected (Hou and Han, 2015).

1.2.4 Stellar velocity fields in the disc

The velocity distribution in the disc in the solar neighbourhood appears highly structured. This could not be the case in a purely axisymmetric disc at equilibrium. Many nearly horizontal arch-like structures can be clearly observed in Figure 1.5. These observations courtesy of the Gaia mission provide more precision and shed light on many new features. The dynamical stream of Hercules for example, while previously restricted to one arch at negative U velocities and $V \simeq 50 kms^1$ (U and V being the in-plane Cartesian heliocentric radial and azimuthal velocities respectively), now appears to be split into two of these branches (at $V \simeq 38 kms^1$ and $V \simeq 50 kms^1$) and perhaps a third one at $V \simeq 70 kms^1$. These arches appear for the whole range of V. Additionally, there is a clear under-density of stars also with an arched shape that extends from $(U, V) \simeq (100, 25)$ to $(U, V) \simeq (75, 65) kms^{-1}$ immediately above the Hercules stream, which separates the velocity plane in two. Rounded structures at the center of the distribution correspond to known moving groups and dynamical streams (Gaia Collaboration et al., 2018a). These substructures are normally associated with the orbital resonances of the bar and spiral arms or alternatively with phase-mixing related to external perturbations or the formation of the bar.

This is particularly important in the context of the interpretation of recent data from the Gaia mission (Gaia Collaboration et al., 2018b; Gaia Collaboration et al.,

2021), which revealed in exquisite detail the fine structure of stellar action space (e.g. Trick, Coronado, and Rix, 2019; Monari et al., 2019a; Monari et al., 2019b). While the existence of moving groups of dynamical origin had been known for a long time in local velocity space around the Sun (e.g. Dehnen, 1998; Famaey et al., 2005), Gaia revealed their structure in exquisite detail (Ramos, Antoja, and Figueras, 2018) and also provided an estimate of their age distribution (Laporte et al., 2020), together with the shape of the global velocity field away from the Sun within the Galactic disc (Gaia Collaboration et al., 2018a). One additional major finding of Gaia is the existence of a local phase-spiral in vertical height versus vertical velocity in the solar neighbourhood (Antoja et al., 2018), which might be related to a vertical perturbation of the disc, for example by the Sagittarius dwarf galaxy (e.g. Laporte et al., 2019; Binney and Schönrich, 2018; Bland-Hawthorn and Tepper-García, 2021). Such an interaction of the disc with a vertical perturber also has a a global effect on the vertical dynamics of the disc (e.g. Poggio et al., 2021) and call for the developments of new methods to derive the vertical acceleration from the disc (Haines et al., 2019).

1.2.5 Bulge/Bar

The Galactic Bulge is an over-density around the center of the Galaxy that swells up from the plane of the disc. The metallicity distribution of the bulge can be separated into a metal-poor and a metal-rich components. The metal-rich component (mean [Fe/H] $\sim$ 0.3) is composed mostly by old stars but with a fraction of young stars. This component takes an elongated shape, what is commonly referred to as the bar with a size of about 3.1 to 3.5 kpc diameter. The metal-poor component (mean [Fe/H] $\sim$ -0.3) is composed predominantly by old stars and has a more spheroidal, centrally concentrated shape. While the box/peanut calls for a formation scenario via disc instabilities, the spheroidal component could account for a formation scenario via violent collapse. It could well be that the Galactic bulge is a composite bulge after all (Gonzalez and Gadotti, 2016). Portail et al., 2017 however point out that recent research has demonstrated that the galactic bulge smoothly segues into the long bar. Both the bulge and bar appear at a similar angle meaning that both are part of a single structure that became thick in its inner part.

At a distance of $\sim$ 8.2 kpc from the sun (Abuter et al., 2019) lies a compact radio source called Sagittarius A* of about 4 million solar masses (Ghez et al., 2008) which is conventionally taken to be the Galactic center.

1.3 Kinetic theory of self-gravitating systems

1.3.1 Collisionless Boltzmann equation

The gravitational force acting between the stars in a galaxy is long-range. In a system where the density of the stars is roughly uniform, the largest contribution to the net gravitational force at a point in the system is from the most distant stars. Consequently, each star may be supposed to accelerate smoothly through the force field that is generated by the galaxy as a whole. Rather than treating the system as a collection of point masses, we may describe it using a smooth distribution function. In fact, for a typical galaxy, the number of stars is of the order of 10^{11} and the relaxation time,

i.e. the time for a typical star moving in the galaxy to undergo a significant change in its velocity through gravitational encounters is much larger than the age of the galaxy (Binney and Tremaine, 2008).

For timescales smaller than the relaxation time, the dynamics of the system are those of a collisionless one where the gravitational field influencing the particles of the system is generated by a smooth distribution function. The distribution function f is defined such that $f(\mathbf{x},\mathbf{v},t)d^3\mathbf{x}d^3\mathbf{v}$ is the probability that at time t a randomly chosen star is present in the six-dimensional phase space volume $d^3\mathbf{x}d^3\mathbf{v}$ around the position $\mathbf{x}$ and velocity $\mathbf{v}$.

f is normalized such that the integral over all phase space

$$\int d^3\mathbf{x}d^3\mathbf{v}\, f(\mathbf{x},\mathbf{v},t) = 1 \tag{1.1}$$

The distribution function has the same numerical value at a given phase space point in any canonical coordinate system. We therefore take $\mathbf{w} = (\mathbf{q}, \mathbf{p})$ as an arbitrary system of canonical coordinates.

Just as a fluid mass that is conserved can be described using the equation

$$\frac{\partial \rho}{\partial t} + \frac{\partial}{\partial \mathbf{x}} \cdot (\rho \dot{\mathbf{x}}) = 0 \tag{1.2}$$

so is the probability in phase space described by the equation

$$\frac{\partial f}{\partial t} + \frac{\partial}{\partial \mathbf{w}} \cdot (f \dot{\mathbf{w}}) = 0 \tag{1.3}$$

Using Hamilton's equations

$$\frac{\partial}{\partial \mathbf{q}} \cdot (f\dot{\mathbf{q}}) + \frac{\partial}{\partial \mathbf{p}} \cdot (f\dot{\mathbf{p}}) = \frac{\partial}{\partial \mathbf{q}} \cdot (f\frac{\partial H}{\partial \mathbf{p}}) - \frac{\partial}{\partial \mathbf{p}} \cdot (f\frac{\partial H}{\partial \mathbf{q}}) = \frac{\partial f}{\partial \mathbf{q}} \cdot \frac{\partial H}{\partial \mathbf{p}}) - \frac{\partial f}{\partial \mathbf{p}} \cdot \frac{\partial H}{\partial \mathbf{q}} = \dot{\mathbf{q}} \cdot \frac{\partial f}{\partial \mathbf{q}} + \dot{\mathbf{p}} \cdot \frac{\partial f}{\partial \mathbf{p}} \tag{1.4}$$

this equation becomes the **collisionless Boltzmann equation**:

$$\frac{\partial f}{\partial t} + \dot{\mathbf{q}} \cdot \frac{\partial f}{\partial \mathbf{q}} + \dot{\mathbf{p}} \cdot \frac{\partial f}{\partial \mathbf{p}} = 0 \tag{1.5}$$

By defining the convective derivative in six dimensions

$$\frac{df}{dt} \equiv \frac{\partial f}{\partial t} + \dot{\mathbf{w}} \cdot \frac{\partial f}{\partial \mathbf{w}} \tag{1.6}$$

where this quantity represents the rate of change of the local probability density as seen by an observer moving along with the star, the collisionless Boltzmann equation simply becomes:

$$\frac{df}{dt} = 0 \tag{1.7}$$

This means that the flow through phase space of the probability fluid is incompressible and the density f of the fluid around a given star always remains the same as it moves through phase space.

1.3.2 Action-angle variables

An integral of motion $I(\mathbf{x},\mathbf{v})$ is any function of the phase space coordinates alone that is constant along an orbit:

$$I[\mathbf{x}(t_1),\mathbf{v}(t_1)] = I[\mathbf{x}(t_2),\mathbf{v}(t_2)] \tag{1.8}$$

One particular set of canonical coordinates that is of much interest to Galactic dynamics and perturbation theory is **action-angle** variables, where the three momenta $\boldsymbol{J}$ are called 'actions' and the conjugate coordinates are called 'angles'.

We denote the action-angle variables by $(\boldsymbol{J},\boldsymbol{\theta})$ where we have $\boldsymbol{J} = (J_1, J_2, J_3)$ and $\boldsymbol{\theta} = (\theta_1, \theta_2, \theta_3)$. By assuming that the actions are integrals of motion, we get from Hamilton's equations:

$$0 = \dot{J}_i = -\frac{\partial H}{\partial \theta_i} \tag{1.9}$$

The Hamiltonian is therefore independent of the coordinates θ_i and Hamilton's equations for the angles become:

$$\dot{\theta}_i = \frac{\partial H}{\partial J_i} \equiv \Omega_i(\boldsymbol{J}) \tag{1.10}$$

Consequently we can express θ_i as functions of time:

$$\theta_i(t) = \theta_i(0) + \Omega_i t \tag{1.11}$$

These canonical coordinates strictly exist only in integrable systems where there are as many integals of the motions as degrees of freedom, but galactic potentials turn out to be quasi-integrable which allows us to make use of these coordinates. Action-angle variables are extremely useful as the orbit of the star can be described by a triplet of actions in action space which is the space whose Cartesian coordinates are the actions. Orbits that possess this characteristic are called regular orbits. One potential for which this formalism is used is the Stäckel potential which is exactly integrable, meaning that all orbits are regular.

In general, the canonical phase-space action-angle variables ($\boldsymbol{J}$,$\boldsymbol{\theta}$) of an integrable system are obtained from a canonical transformation implicitly using Hamilton's characteristic function as a type 2 generating function. The actions $\boldsymbol{J}$ are defined as new generalized momenta corresponding to a closed path integral of the velocities along their corresponding canonically conjugate position variable, namely $J_i = \oint v_i \mathrm{d}x_i/(2\pi)$. Since this does not depend on time, these actions are integrals of motion, and the Hamiltonian can be expressed purely as a function of these actions.

1.3.3 Jeans theorem

Simple solutions of the collisionless Boltzmann equation can be written if the dependence of the distribution function on the phase space coordinates is only through integrals of motion.

If a function $I(\mathbf{x},\mathbf{v})$ is an integral of motion then:

$$\frac{dI}{dt}[\mathbf{x}(t),\mathbf{v}(t)] = 0 \tag{1.12}$$

Let f be a distribution function generated by n integrals of motion. Consequently, we get

$$\frac{df}{dt} = \sum_{i=1}^{n} \frac{\partial f}{\partial I_i} \frac{dI_i}{dt} = 0 \tag{1.13}$$

and f therefore satisfies the collisionless Boltzmann equation. This means that any function that depends on phase space coordinates only through integrals of the motion is automatically a solution of the collisionless Boltzmann equation. But in an integrable system, something much stronger can be proven:

Strong Jeans theorem The distribution function of a steady-state stellar system in which almost all orbits are regular with non-resonant frequencies is a function only of three independent isolating integrals, which may be taken to be the actions.

Particularly, this implies that in an axisymmetric system in equilibrium, the phase-space distribution function (DF) of any stellar (or dark matter) component can be expressed solely as a function of the actions that are labelling the actual orbits (e.g. Binney and Piffl, 2015; Cole and Binney, 2017). However, the effect of various perturbers of the potential (e.g. the Galactic bar and spiral arms) must be included in this process, together with the response of the distribution function. Within the resonant regions, to fully capture the behaviour of the DF, one needs to construct for each perturber new orbital tori, complete with a new system of action-angle variables (e.g. Monari et al., 2017a; Binney, 2020a; Binney, 2020b). Away from resonances, however, one can simply use the linearized Boltzmann equation. If $\Phi_1(J,\theta)$ is the potential of a small perturbation to the axisymmetric background potential Φ_0 of the Galaxy, then the total potential is $\Phi = \Phi_0 + \Phi_1$ and the distribution function becomes $f = f_0(J) + f_1(J,\theta)$ which would yield $\frac{df_1}{dt} = \frac{\partial f_0}{\partial J} \cdot \frac{\partial \Phi_1}{\partial \theta}$.

1.3.4 Epicyclic approximation

In an axisymmetric potential, the motion of the stars in three dimensions can be reduced to the motion of these stars in their meridian plane under the effective potential $\Phi_{eff}(R,z)$.

The equations of motion are

$$\ddot{R} = -\frac{\partial \Phi_{eff}}{\partial R} \tag{1.14}$$

$$\ddot{z} = -\frac{\partial \Phi_{eff}}{\partial z} \tag{1.15}$$

where

$$\Phi_{eff} = \Phi(R,z) + \frac{L_z^2}{2R^2} \tag{1.16}$$

Φ_{eff} reaches its minimum when its derivatives cancel which yields

$$z = 0 \tag{1.17}$$

$$\frac{\partial \Phi}{\partial R}(R_g, 0) = \frac{L_z^2}{R_g^3} = R_g(\dot{\phi})^2 \tag{1.18}$$

The described motion is then a circular orbit in the plane $z = 0$, of radius R_g, angular velocity $\dot{\phi}$ and angular momentum L_z.

Most orbits in spiral galaxies are very close to a circular orbit. By making the change of variable $x = R - R_g$, one gets

$$\Phi_{eff} \approx \frac{1}{2}(\frac{\partial^2 \Phi_{eff}}{\partial R^2})_{(R_g,0)} x^2 + \frac{1}{2}(\frac{\partial^2 \Phi_{eff}}{\partial z^2})_{(R_g,0)} z^2 \tag{1.19}$$

We define the epicyclic radial frequency

$$\kappa^2(R_g) = (\frac{\partial^2 \Phi_{eff}}{\partial R^2})_{(R_g,0)} \tag{1.20}$$

and the epicyclic vertical frequency

$$\nu^2(R_g) = (\frac{\partial^2 \Phi_{eff}}{\partial z^2})_{(R_g,0)} \tag{1.21}$$

Thus, we get

$$\ddot{x} = -\kappa^2 x \tag{1.22}$$

$$\ddot{z} = -\nu^2 z \tag{1.23}$$

These are the equations of motion of two non-coupled harmonic oscillators, one at frequency κ, the other at frequency ν. The stars loop around the position they would occupy if their orbits were strictly circular. Epicycles are ellipses with loops, whose eccentricity is related to the values of κ. The stars rotate in the direct direction on the circle, and in the retrograde direction on the epicycle. During this time, they also perform a periodic motion on either side of the plane of the galaxy related to ν. Within that approximation, the three actions $J_R, J_\phi and J_z$ can be written explicitly.

$$J_R \simeq \frac{1}{\pi} \int_{R_{min}}^{R_{max}} dR \sqrt{2(E_R - \Phi_{0,R})} = \frac{E_R}{\kappa} \tag{1.24}$$

$$J_p hi = \frac{1}{2\pi} \int_0^{2\pi} d\phi L_z = L_z \tag{1.25}$$

$$J_z \simeq \frac{1}{\pi} \int_{z_{min}}^{z_{max}} dz \sqrt{2(E_z - \Phi_{0,z})} = \frac{E_z}{\nu} \tag{1.26}$$

1.3.5 Torus Mapping and Stäckel fudge

Galactic potentials are close enough to integrable systems that actions can be estimated for them. For quasi-circular orbits close to the Galactic plane, with separable motion in the vertical and horizontal directions, one can locally approximate the radial and vertical motions of an orbit with harmonic motions, which is known as the epicyclic approximation. The radial and vertical actions then simply correspond to the radial and vertical energies divided by their respective (radial and vertical) epicyclic frequency as seen above. However, the epicyclic approximation is no longer valid when considering orbits with higher eccentricity, or with a large vertical

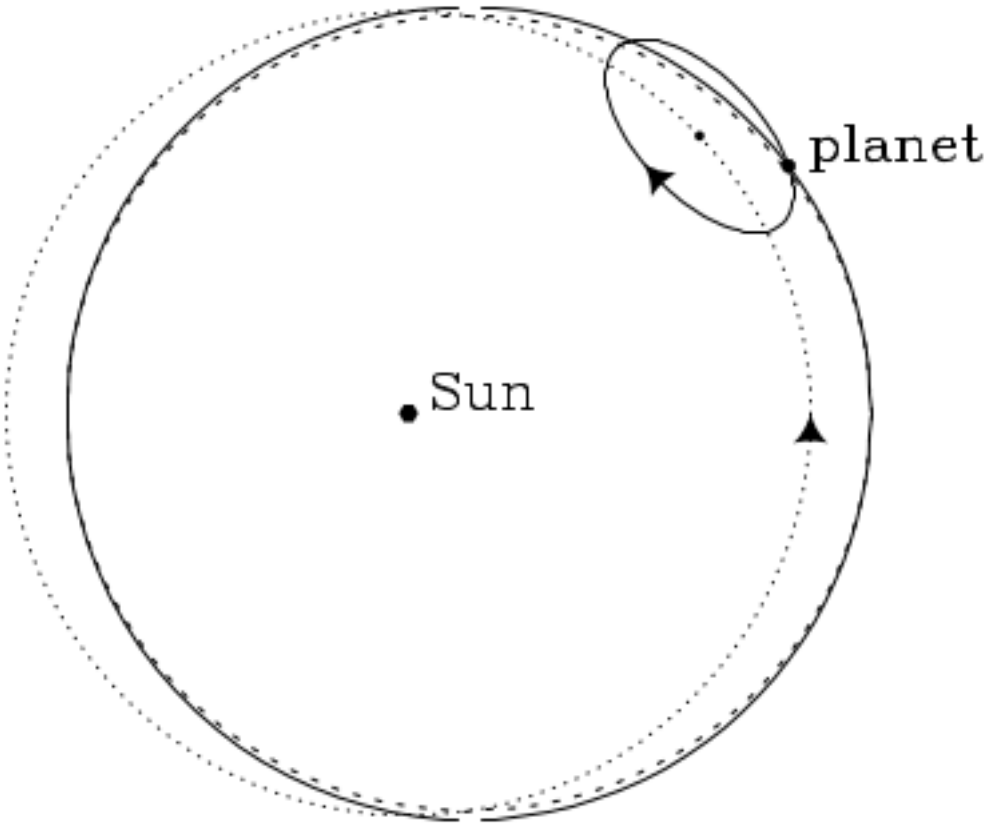

FIGURE 1.6: Representation of epicyclic motion.

amplitude. More precise ways of determining the action and angle coordinates have been devised. They typically differ depending on whether one wishes to transform angles and actions to positions and velocities or instead to make the reverse transformation from positions and velocities to actions and angles. In the first case a very efficient method is the torus mapping method first introduced by McGill and Binney, 1990 (see also Binney and McMillan 2016 for a recent overview), while in the second case a Stäckel fudge is generally used (Binney, 2012; Sanders and Binney, 2016).

The general idea of torus mapping is to first express the Hamiltonian in the action-angle coordinates $(\boldsymbol{J}_T, \boldsymbol{\theta}_T)$ of a toy potential, for which the transformation to positions and velocities is fully known analytically. The algorithm then searches for a type 2 generating function $G(\boldsymbol{\theta}_T, \boldsymbol{J})$ expressed as a Fourier series expansion on the toy angles $\boldsymbol{\theta}_T$, for which the Fourier coefficients are such that the Hamiltonian remains constant at constant $\boldsymbol{J}$. This generating function fully defines the canonical transformation from actions and angles to positions and velocities. For the inverse transformation, an estimate based on separable potentials can be used. These potentials are known as Stäckel potentials (e.g. Famaey and Dejonghe, 2003), for which each generalized momentum depends on its conjugated position through three isolating integrals of the motion. These potentials are expressed in spheroidal coordinates defined by a focal distance. For a Stäckel potential, this focal distance of the coordinate system is related to the first and second derivatives of the potential. One can thus use the true potential at any configuration space point to compute the equivalent focal distance as if the potential were of Stäckel form, and from there compute the corresponding isolating integrals of the motion and the actions.

1.4 Outline of the thesis

My thesis has used more accurately calculated 'angle-action' phase space coordinates than before to refine our dynamical models of the Milky Way, and in particular the effects of the bar and spiral arms of the Galaxy. I first set out, in the continuity of the work of Monari, Famaey, and Siebert, 2016 to recalculate the set of predictions of a perturbed six-dimensional distribution function in phase space outside the resonant zones and predicting the location of the resonant zones. We also considered the response of the distribution function under a time-dependent perturbation. This is presented in Chapters 2,3 and 4. This linearized treatment however diverges in the resonant zones. I then adapted the method of Monari et al., 2017b to compute the response in space of trapped orbits to a resonance of the bar. This is presented in Chapter 5. My results were used in a recent paper by Bernet et al.(2022) based on Gaia data, of which I am co-author. A small delineation of the paper is presented in Chapter 6. Lastly, we were able to predict radial velocity maps of stars in the disc of the Galaxy in the presence of a bar using Backwards orbit integrations, to be compared to the Gaia data. This is described in Chapter 7. Finally, Chapter 8 will present my two published papers as first author and co-author, and Chapter 9 summarizes the results and perspective of the present work.

Chapter 2

Perturbing potential and perturbed distribution function

We let $H_0(\boldsymbol{J})$ be the Hamiltonian of the axisymmetric and time-independent zeroth order gravitational potential Φ_0 of the Galaxy. The equations of motion connecting actions $\boldsymbol{J}$ and the canonically conjugate angles $\boldsymbol{\theta}$ are then simply

$$\dot{\boldsymbol{\theta}} = \frac{\partial H_0}{\partial \boldsymbol{J}} = \boldsymbol{\omega}(\boldsymbol{J}), \quad \dot{\boldsymbol{J}} = -\frac{\partial H_0}{\partial \boldsymbol{\theta}} = 0, \tag{2.1}$$

with $\boldsymbol{\omega}$ being the fundamental orbital frequencies. Thus, for a given orbit, the actions $\boldsymbol{J}$ are constant in time, defining an orbital torus on which the angles $\boldsymbol{\theta}$ evolve linearly with time, according to $\boldsymbol{\theta}(t) = \boldsymbol{\theta}_0 + \boldsymbol{\omega} t$. The Jeans theorem then tells us that the phase-space distribution function (DF) of an axisymmetric potential $f = f_0(\boldsymbol{J})$ is in equilibrium. In other words, f_0 is a solution of the collisionless Boltzmann equation:

$$\frac{\mathrm{d}f}{\mathrm{d}t} = 0. \tag{2.2}$$

2.1 Perturbed distribution functions

We now let Φ_1 be the potential of a small perturbation to the axisymmetric background potential Φ_0 of the Galaxy, with an amplitude relative to this axisymmetric background $\epsilon \ll 1$. Then the total potential is $\Phi = \Phi_0 + \Phi_1$ and the DF becomes, to first order in ϵ, $f = f_0 + f_1$, which is still a solution of the collisionless Boltzmann equation. Inserting $f = f_0 + f_1$ in Eq. (2.2), and keeping only the terms of order ϵ, leads to the *linearized* collisionless Boltzmann equation

$$\frac{\mathrm{d}f_1}{\mathrm{d}t} + [f_0, \Phi_1] = 0, \tag{2.3}$$

where [,] is the Poisson bracket. Integrating Eq. (2.3) over time, from $-\infty$ to the time t, leads to

$$f_1(\boldsymbol{J}, \boldsymbol{\theta}, t) = \int_{-\infty}^{t} \mathrm{d}t' \frac{\partial f_0}{\partial \boldsymbol{J}'}(\boldsymbol{J}') \cdot \frac{\partial \Phi_1}{\partial \boldsymbol{\theta}'}(\boldsymbol{J}', \boldsymbol{\theta}', t'), \tag{2.4}$$

where $\boldsymbol{J}'$ and $\boldsymbol{\theta}'$ correspond to the actions and angles in the unperturbed case as a function of time (i.e. constant actions $\boldsymbol{J}'$ and angles evolving linearly). Since any function of the angles is 2π-periodic in the angles, the perturbing potential Φ_1 can be

expanded in a Fourier series as

$$\Phi_1(\boldsymbol{J},\boldsymbol{\theta},t) = \mathrm{Re}\left\{\sum_{\boldsymbol{n}} \phi_{\boldsymbol{n}}(\boldsymbol{J},t)\,\mathrm{e}^{\mathrm{i}\boldsymbol{n}\cdot\boldsymbol{\theta}}\right\}. \tag{2.5}$$

Hereafter we consider in-plane perturbations such as spiral arms, meaning that we can write the time-varying Fourier coefficients in a non-rotating frame as $\phi_{\boldsymbol{n}}(\boldsymbol{J},t) = g(t)\,h(t)\,\phi_{\boldsymbol{n}}(\boldsymbol{J})$, where $g(t)$ controls the amplitude of the perturbation and $h(t)$ controls its pattern speed, with $h(t) = \mathrm{e}^{-\mathrm{i}m\Omega_\mathrm{p}t}$, where Ω_p is the pattern speed of the perturbation and m its azimuthal wave number (i.e. its multiplicity). Hereafter we mainly consider $m = 2$ perturbations. The vector index $\boldsymbol{n}$ is a triplet of scalar integer indices (j,k,l) running in principle from $-\infty$ to ∞, but in practice limited to a given range sufficient to approximate the perturbing potential. In the case of an m-fold in-plane perturbation, it is sufficient to take $k = m$. The main goal of this section is to express typical non-axisymmetric perturbing potentials originally expressed in configuration space as such a Fourier series in action-angle space. The algorithm that we present in Sect. 2.3 can be applied to any perturbing potential, however, including non-plane symmetric vertical perturbations. Once the potential is expressed as a function of angles and actions as in Eq. (2.5), then Eq. (2.4) becomes

$$f_1(\boldsymbol{J},\boldsymbol{\theta},t) = \mathrm{Re}\left\{\mathrm{i}\frac{\partial f_0}{\partial \boldsymbol{J}}(\boldsymbol{J})\cdot\sum_{\boldsymbol{n}}\boldsymbol{n}\int_{-\infty}^{t}\mathrm{d}t'\phi_{\boldsymbol{n}}(\boldsymbol{J}',t')\,\mathrm{e}^{\mathrm{i}\boldsymbol{n}\cdot\boldsymbol{\theta}'(t')}\right\}. \tag{2.6}$$

In M16, assuming $\phi_{\boldsymbol{n}}(\boldsymbol{J}',t') = g(t')\,h(t')\,\phi_{\boldsymbol{n}}(\boldsymbol{J})$, with $h(t') = \mathrm{e}^{-\mathrm{i}m\Omega_\mathrm{p}t'}$, and the amplitude of the perturbing potential constant in time at present time ($g(t) = 1$), and zero and constant in time at $-\infty$, led to the following explicit solution for $f_1(\boldsymbol{J},\boldsymbol{\theta},t)$,

$$f_1(\boldsymbol{J},\boldsymbol{\theta},t) = \mathrm{Re}\left\{\frac{\partial f_0}{\partial \boldsymbol{J}}(\boldsymbol{J})\cdot\sum_{\boldsymbol{n}}\boldsymbol{n}\phi_{\boldsymbol{n}}(\boldsymbol{J})\frac{\mathrm{e}^{\mathrm{i}\theta_{\mathrm{s},\boldsymbol{n}}}}{\omega_{\mathrm{s},\boldsymbol{n}}}\right\}, \tag{2.7}$$

where we defined

$$\theta_{\mathrm{s},\boldsymbol{n}} = \boldsymbol{n}\cdot\boldsymbol{\theta} - m\Omega_\mathrm{p}t, \tag{2.8}$$

$$\omega_{\mathrm{s},\boldsymbol{n}} = \boldsymbol{n}\cdot\boldsymbol{\omega} - m\Omega_\mathrm{p}. \tag{2.9}$$

The subscript 's' stands for slow, because in the proximity of a resonance of the type $\omega_{\mathrm{s},\boldsymbol{n}} = 0$, the angle $\theta_{\mathrm{s},\boldsymbol{n}}$ evolves very slowly. One can also immediately see that the linearized solution above is valid only away from such resonances since it diverges for these orbits. Orbits near these resonances are actually trapped, and for them the determination of the linearly perturbed DF becomes inappropriate. Specific treatment for these resonant regions is required, which was addressed in Monari et al. (2017a) within the epicyclic approximation, and by Binney (2020a) in a more general context.

Using the epicyclic approximation the Fourier coefficients of a spiral potential have been computed analytically in M16 with indices $\boldsymbol{n} = (j,k,l)$ running over the values $j = \{-1,0,1\}$, $k = m = 2$, and $l = \{-2,0,2\}$, and the perturbed distribution function away from resonances was then computed. In the following we extend the results of M16 to a more general estimate of the action-angle variables through the torus mapping method. The resulting DF is plotted in velocity space by making

use of the Stäckel fudge. For both transformations we use the Action-based Galaxy Modelling Architecture (`AGAMA`; Vasiliev, 2019; Vasiliev, 2018).

2.2 Perturbing potential in actions and angles

In previous work, M16 worked in the epicyclic approximation as it provides an analytical expression for evaluating actions and angles from cylindrical coordinates. The Fourier coefficients of the Fourier series expansion of the perturbing potentials were then also determined analytically within this approximation. Approximating the vertical component of the perturbing potential by a harmonic oscillator, the nine Fourier coefficients ϕ_{jml} were then limited to the range $j = \{-1, 0, 1\}$, corresponding to the θ_R oscillations of the potential, and $l = \{-2, 0, 2\}$, corresponding to the θ_z oscillations of the potential close to the Galactic plane.

However, the epicyclic approximation is only valid for nearly circular orbits, but not when considering eccentric orbits. Hereafter the transformations from angles and actions to positions and velocities (and reciprocally) are instead evaluated numerically with `AGAMA` (Vasiliev, 2018). The code makes use of torus mapping to go from action-angle to position-velocity, and uses the Stäckel fudge for the inverse transformation. Our goal now is to obtain the Fourier coefficients of a known perturbing potential using these numerically computed actions (instead of epicyclic).

We proceed in the following way to evaluate Fourier coefficients of the perturbing potential in Eq. (2.5). The first step is to choose a set of actions within a range representing all the orbits of interest in the axisymmetric background configuration, each triplet of actions representing one of the orbits. For instance, in the solar neighbourhood we consider radial actions ranging from 0 to 220 kpc km s^{-1}, azimuthal actions ranging from 1200 to 2160 kpc km s^{-1}, and vertical actions ranging from 0 to 26 kpc km s^{-1} depending on the height above the Galactic plane. For each orbit, we then define an array of angles $(\theta_R, \theta_\varphi, \theta_z)$. These actions and angles can then all be converted to positions thanks to the torus machinery in `AGAMA`. For each triplet of actions, a range of positions (R, φ, z) is covered by the angles, and we look for the best-fitting coefficients $\phi_{jml}(J_R, J_z, J_\varphi)$, satisfying the following equation (setting $t = 0$ for the time being):

$$\Phi_1(R, \varphi, z) = \mathrm{Re}\left\{\sum_{j,l} \phi_{jml}(J_R, J_z, J_\varphi) \mathrm{e}^{\mathrm{i}(j\theta_R + m\theta_\varphi + l\theta_z)}\right\}. \tag{2.10}$$

This is performed with the method of linear least squares using singular value decomposition, as proposed in chapter 15.4 of Press et al. (1992). We then interpolate the value of the coefficient ϕ_{jml} with cubic splines, also proposed in Press et al. (1992), chapter 3.3. The number of Fourier coefficients is chosen to be high enough to ensure that all orbits passing through a given configuration space point yield the same value of the potential at this point within a relative accuracy of less than 1%.

Concretely, we apply this hereafter to the potential of a central bar and of a two-armed spiral pattern. The background axisymmetric potential is chosen to be Model I from Binney and Tremaine (2008). This potential has a bulge described by a truncated oblate spheroidal power law; a gaseous disc with a hole at the centre; a stellar thin disc and a stellar thick disc, both with a scale-length of 2 kpc; and a dark halo

with an oblate two-power-law profile. The galactocentric radius of the Sun is set at $R_0 = 8$ kpc, and the local circular velocity is $v_0 = 220$ km s^{-1}.

2.3 Bar potential

The potential we choose for the bar is a simple quadrupole potential (Weinberg, 1994; Dehnen, 2000) with

$$\Phi_{1,\mathrm{b}}(R,z,\varphi,t) = \mathrm{Re}\left\{\Phi_{\mathrm{a,b}}(R,z)\mathrm{e}^{\mathrm{i}m(\varphi-\varphi_\mathrm{b}-\Omega_\mathrm{b}t)}\right\}, \tag{2.11}$$

where $m = 2$, Ω_b is the pattern speed of the bar (expressed hereafter in multiples of the angular frequency at the Sun $\Omega_0 = v_0/R_0$, where v_0 is the local circular velocity at the galactocentric radius of the Sun R_0), and the azimuth is defined with respect to a line corresponding to the Galactic centre-Sun direction in the Milky Way, φ_b thus being the angle between the Sun and the long axis of the bar. We also choose

$$\Phi_{\mathrm{a,b}}(R,z) = -\alpha_\mathrm{b}\frac{v_0^2}{3}\left(\frac{R_0}{R_\mathrm{b}}\right)^3\left(\frac{R}{r}\right)^2\begin{cases}\left(\dfrac{r}{R_\mathrm{b}}\right)^{-3} & R \geq R_\mathrm{b},\\ 2-\left(\dfrac{r}{R_\mathrm{b}}\right)^3 & R < R_\mathrm{b},\end{cases} \tag{2.12}$$

where $r^2 = R^2 + z^2$ is the spherical radius, R_b is the length of the bar, and α_b represents the maximum ratio between the bar and axisymmetric background radial forces at the Sun's galactocentric radius $R = R_0$. We use hereafter, as a representative example, $R_\mathrm{b} = 0.625\,R_0$, $\varphi_\mathrm{b} = 25^\mathrm{o}$, and $\alpha_\mathrm{b} = 0.01$. We also consider two typical pattern speeds: $\Omega_\mathrm{b} = 1.89\,\Omega_0$ and $\Omega_\mathrm{b} = 1.16\,\Omega_0$.

The bar potential is quite easy to reproduce using Fourier coefficients since it varies smoothly on orbits. Thus, for a study in the Galactic plane, 41 complex Fourier coefficients for each triplet of actions are sufficient to approximate the value of the potential with an accuracy much better than 1%. Here it should be noted that the potential of the bar oscillates along the azimuth at a given radius and that the relative accuracy can be ill-defined when the potential passes through zero. Therefore, we define here the relative accuracy with respect to the amplitude (i.e. the maximum value) of the bar potential at a given radius. The Fourier coefficients themselves vary smoothly, as illustrated in Fig. 2.1, which shows the variations of a few Fourier coefficients as J_R and J_φ increase separately, justifying the use of cubic-spline interpolation to get the value of the potential at a specific position. Figure 2.2 demonstrates the accuracy of our method in reproducing the bar potential in the solar neighbourhood for different values of the local velocities. The potential is estimated at the same configuration space location for the whole range of relevant velocities, with a typical accuracy at the per cent level both in the plane and at $z = 0.3$ kpc. The accuracy remains very good above the plane, although with a slight bias towards lower amplitudes than the true value. More complex Fourier coefficients are needed outside

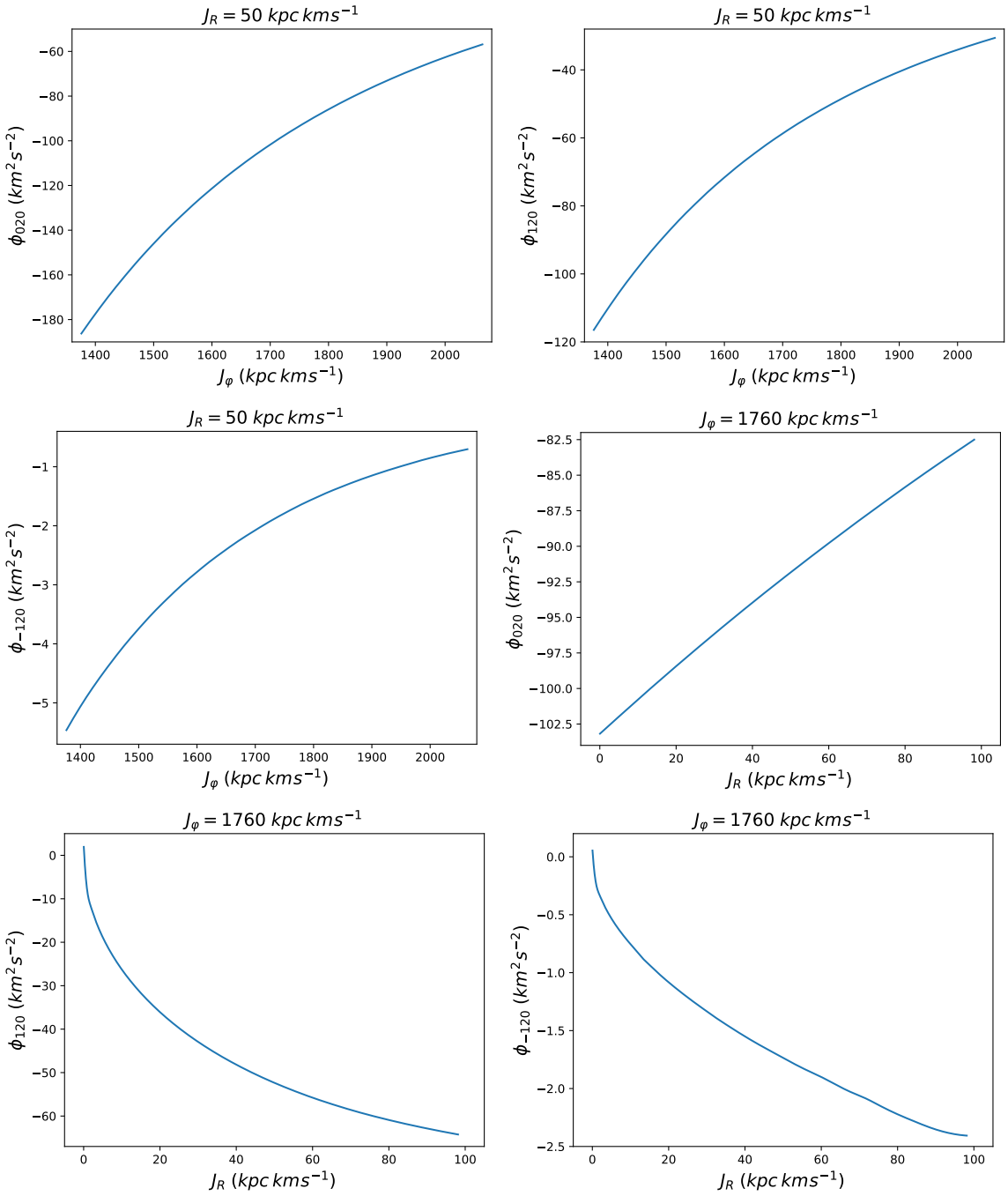

FIGURE 2.1: Variations in a few Fourier coefficients $\phi_{jml}(\boldsymbol{J})$ of the bar potential from Sect. 2.4 as J_R or J_φ increase separately at $J_z = 0$. The actions on the abscissa axis are in kpc km s^{-1}. The curves are very smooth, which justifies our use of the cubic splines method to interpolate.

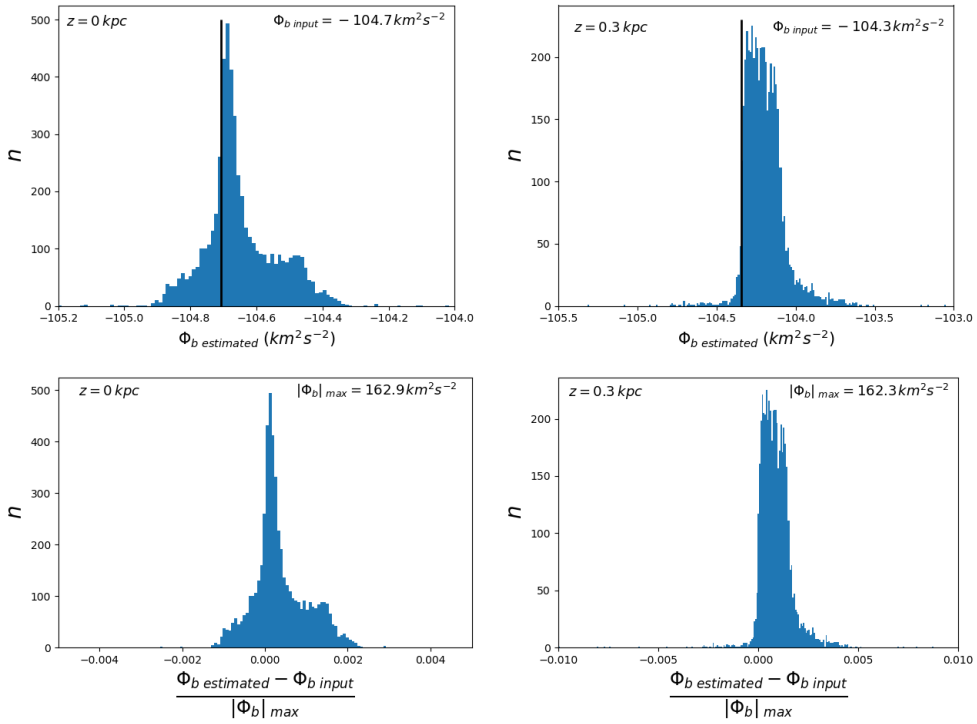

FIGURE 2.2: Accuracy of the reconstruction of the bar potential . Left panel (top): Estimate of the bar potential from Sect. 2.4 at the Sun's position in the plane with 41 complex Fourier coefficients in Eq. 2.10 and the reconstruction using cubic splines. The vertical line denotes the true value. The value in the top right inset denotes the true value in physical units. The potential is always estimated at the same configuration space location (within the plane, at the Sun's position) but for different velocities. Left panel (bottom): Relative accuracy compared to the maximum value of the bar potential at the Sun's radius denoted in the top right inset. Right panel: Same, but at $z = 0.3$ kpc with 231 complex Fourier coefficients. The typical accuracy is well below the per cent level, although with a slight bias towards lower amplitudes (i.e. $|\Phi_{\mathrm{b\,estimated}}| < |\Phi_{\mathrm{b\,input}}|$) above the plane.

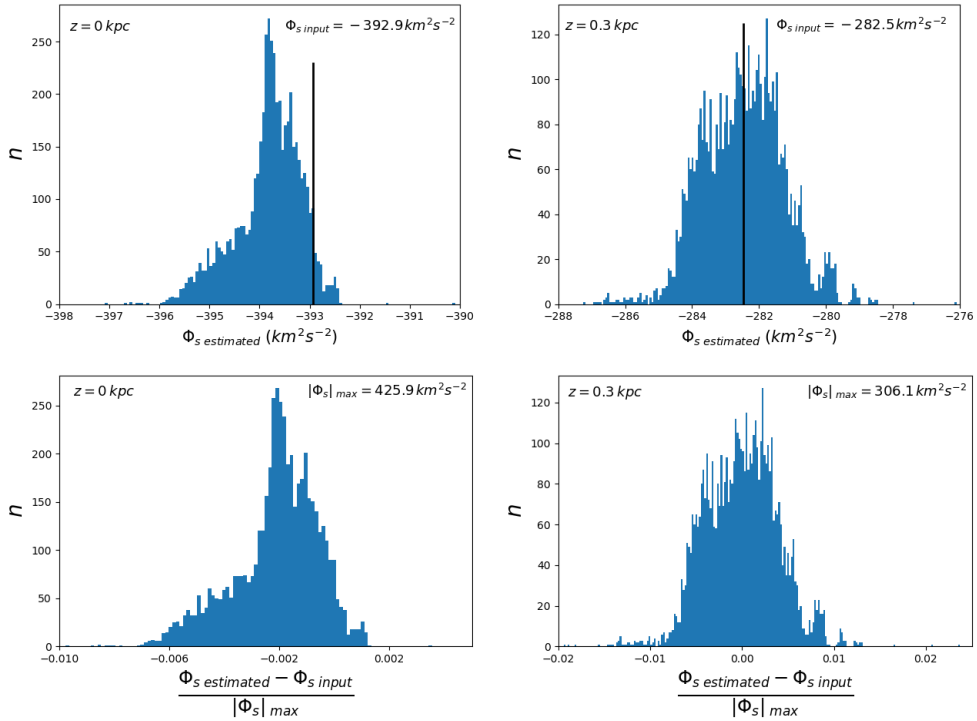

FIGURE 2.3: Accuracy of the reconstruction of the spiral arms potential. Left panel (top): Estimate of the spiral arms potential from Sect. 2.5 at the Sun's position in the plane with 41 complex Fourier coefficients in Eq. 2.10 and the reconstruction using cubic splines. The vertical line denotes the true value. The value in the top right inset denotes the true value in physical units. The potential is always estimated at the same configuration space location (within the plane, at the Sun's position) but for different velocities. Left panel (bottom): Relative accuracy compared to the maximum value of the spiral arms potential at the Sun's radius denoted in the top right inset. Right panel: Same, but at $z = 0.3$ kpc with 231 complex Fourier coefficients. The typical accuracy is again well below the per cent level in the plane, while it is around the per cent level above the plane.

of the plane. This tool is of course not limited to any specific form of the perturbing potential, the only adjustable parameter being the number of Fourier coefficients necessary to recover a given perturbing potential with a per cent-level accuracy.

2.4 Spiral potential

The potential we use for the spiral arms is the following (Cox and Gómez, 2002; Monari, Famaey, and Siebert, 2016)

$$\Phi_{1,\mathrm{sp}}(R,z,\varphi,t) = \mathrm{Re}\left\{\Phi_{\mathrm{a,sp}}(R,z)\,\mathrm{e}^{im(\varphi-\varphi_{\mathrm{sp}}-\Omega_{\mathrm{sp}}t)}\right\}, \tag{2.13}$$

where $m = 2$, $\Omega_{\rm sp}$ is the pattern speed of the spiral arms, and

$$\Phi_{\rm a,sp}(R,z) = -\frac{A}{R_{\rm sp}KD} {\rm e}^{{\rm i}m\frac{\ln(R/R_{\rm sp})}{\tan(p)}} \left[\mathrm{sech}\left(\frac{Kz}{\beta}\right)\right]^{\beta}, \tag{2.14}$$

where

$$\begin{aligned} K(R) &= \frac{2}{R\sin(p)}, \quad \beta(R) = K(R)h_{\rm sp}[1+0.4K(R)h_{\rm sp}], \\ D(R) &= \frac{1+K(R)h_{\rm sp}+0.3[K(R)h_{\rm sp}]^2}{1+0.3K(R)h_{\rm sp}}. \end{aligned} \tag{2.15}$$

Here $R_{\rm sp} = 1\,$kpc is the length parameter of the logarithmic spiral potential, $h_{\rm sp} = 0.1\,$kpc the height parameter, $p = -9.9^{\rm o}$ the pitch angle, $\varphi_{\rm sp} = -26^{\rm o}$ the phase, and $A = 683.4\,{\rm km^2\,s^{-2}}$ the amplitude. Hereafter, we adopt a pattern speed $\Omega_{\rm sp} = 0.84\,\Omega_0$, placing the main resonances away from (or at high azimuthal velocities in) the solar neighbourhood.

Within the Galactic plane, the top panel of Fig. 2.3 shows our reconstruction of the spiral potential at the Sun's position, again with 41 complex Fourier coefficients. The accuracy is again below the per cent level as in the bar case, although in the spiral case there is a slight bias towards higher amplitudes with respect to the input spiral potential. This bias is very small, however, and does not affect our results. At $z = 0.3$ kpc, more complex Fourier coefficients are again needed (Fig. 2.3, bottom panel), and the accuracy reaches the per cent level, this time without bias.

Chapter 3

Linear perturbations with accurate action estimates

3.1 Background equilibrium

From here on we work with a background axisymmetric DF f_0 as a sum of two quasi-isothermal DFs (Binney and McMillan, 2011) for the thin and thick disc:

$$f_0(J_R, J_z, J_\varphi) = f_{\rm thin} + 0.075 f_{\rm thick}. \tag{3.1}$$

The form of each DF is

$$f(J_R, J_z, J_\varphi) = \frac{\Omega \exp(-R_{\rm g}/h_R)}{2\,(2\pi)^{3/2}\,\kappa\,\tilde{\sigma}_R^2\,\tilde{\sigma}_z\,z_0} \exp\left(-\frac{J_R\kappa}{\tilde{\sigma}_R^2} - \frac{J_z\nu}{\tilde{\sigma}_z^2}\right), \tag{3.2}$$

where $R_{\rm g}$, Ω, κ, and ν are all functions of J_φ, and

$$\begin{aligned} \tilde{\sigma}_R(R_{\rm g}) &= \tilde{\sigma}_R(R_0) \exp\left(-\frac{R_{\rm g} - R_0}{h_{\sigma_R}}\right), \\ \tilde{\sigma}_z(R_{\rm g}) &= \tilde{\sigma}_z(R_0) \exp\left(-\frac{R_{\rm g} - R_0}{h_{\sigma_z}}\right). \end{aligned} \tag{3.3}$$

For the thin disc DF $f_{\rm thin}$, we choose $h_R = 2$ kpc, $z_0 = 0.3$ kpc, $h_{\sigma_R} = h_{\sigma_z} = 10$ kpc, $\tilde{\sigma}_R(R_0) = 35$ km s^{-1}, and $\tilde{\sigma}_z(R_0) = 15$ km s^{-1}. For the thick disc DF $f_{\rm thick}$, we choose $h_R = 2$ kpc, $z_0 = 1$ kpc, $h_{\sigma_R} = 10$ kpc, $h_{\sigma_z} = 5$ kpc, $\tilde{\sigma}_R(R_0) = 50$ km s^{-1}, and $\tilde{\sigma}_z(R_0) = 50$ km s^{-1}. Since we normalize the central surface densities of the thin and thick disc to 1, our densities can be multiplied by the appropriate surface density of the relevant stellar population to obtain physical units. The background axisymmetric potential is chosen to be Model I from Binney and Tremaine (2008), in which the above equilibrium DF f_0 is a good representation of the thin and thick disc components. In this model one has $R_0 = 8$ kpc and $v_0 = 220$ km s^{-1}.

The top panels of Fig. 3.1 display the (u, v)-plane in the solar neighbourhood within the $z = 0$ plane (and for $w = -v_z = 0$) for this f_0 axisymmetric background, where $u = -v_R$ and $v = v_\varphi - v_0$, obtained by converting velocity-space into action-space through the epicyclic approximation and the Stäckel fudge from `AGAMA`. The velocity distributions are quite similar. However, as can be seen in the bottom panels of Fig. 3.1, the epicyclic approximation quickly becomes imprecise outside of the

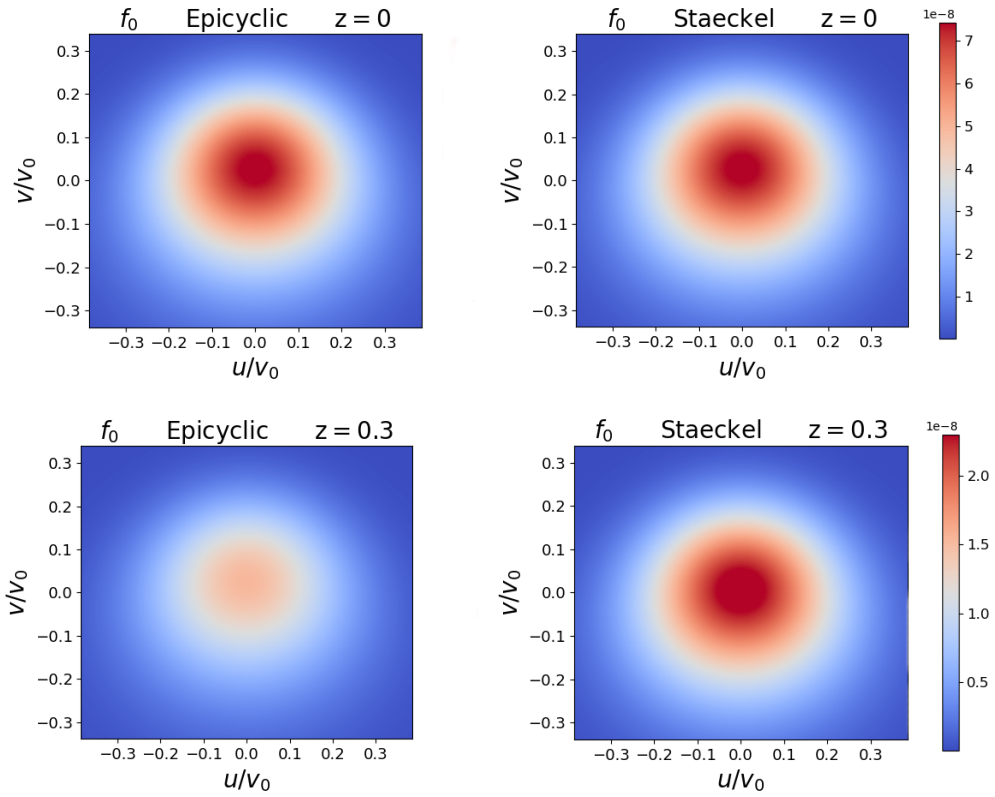

FIGURE 3.1: Local uv-plane stellar velocity distribution at axisymmetric equilibrium and for $w = 0$, from Eq. 3.1 at $(R, z, \varphi) = (R_0, 0, 0)$. Left panel: Epicyclic approximation in the plane (top) and at $z = 0.3$ kpc (bottom). Right panel: Stäckel fudge with `AGAMA` in the plane (top) and at $z = 0.3$ kpc (bottom).

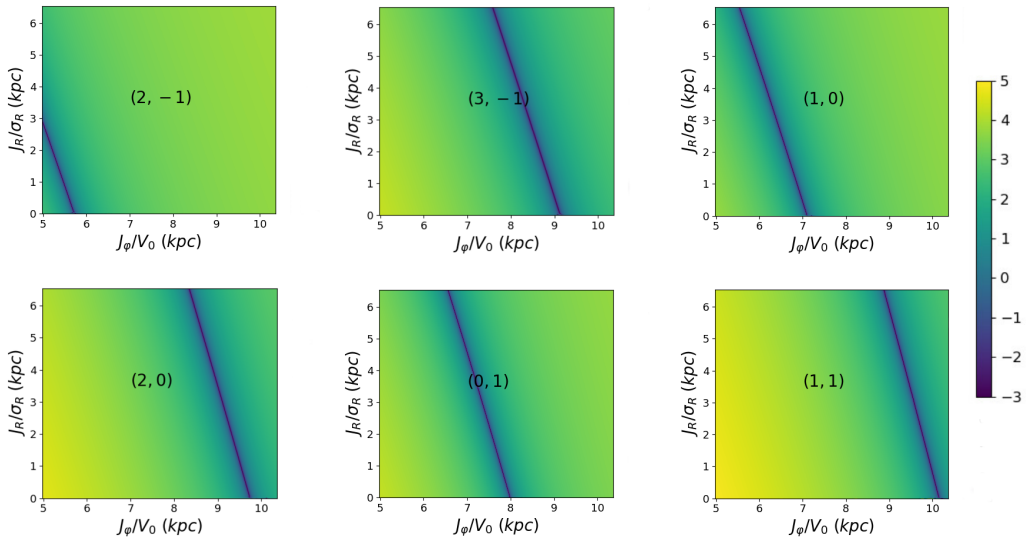

FIGURE 3.2: Values of $\log(\omega_{s,jml})$ in the (J_R, J_φ) plane with fixed $J_z = 10$ kpc km s^{-1}, for a few combinations of (j,l) indices giving rise to resonant zones in action space (recalling that $m = 2$). The pattern speed Ω_p here is $1.89\,\Omega_0$. The two actions are renormalized by the radial velocity dispersion of the thin disc and the circular velocity at the Sun, respectively. The deep blue lines correspond to resonant zones. For instance, the $(1,0)$ case corresponds to the traditional OLR (for a non-zero J_z). Most other low-order combinations of indices did not give rise to any relevant resonant zone in the region of interest.

plane as it implies a sharper falloff of the density compared to the better Stäckel action estimates.

3.2 Resonant zones

In the case of a perturbation with quasi-static amplitude that has reached its plateau, once the Fourier coefficients representing the perturbing potential have been computed (from the epicyclic approximation or from Eq. 2.10) the expression for the perturbed DF can be simply expressed away from resonances with Eq. 2.7 as

$$f_1(\boldsymbol{J},\boldsymbol{\theta},t) = \mathrm{Re}\left\{\sum_{j,l=-n}^{n} f_{jml}\, \mathrm{e}^{\mathrm{i}[j\theta_R + m(\theta_\varphi - \Omega_p t) + l\theta_z]}\right\}, \tag{3.4}$$

with n the order of the Fourier series (in this paper, $m = 2$ in both the bar and spiral cases), and

$$f_{jml} = \phi_{jml} \times \frac{j\frac{\partial f_0}{\partial J_R} + m\frac{\partial f_0}{\partial J_\varphi} + l\frac{\partial f_0}{\partial J_z}}{j\omega_R + m(\omega_\varphi - \Omega_p) + l\omega_z}, \tag{3.5}$$

where ω_R, ω_φ, and ω_z can be approximated as epicyclic frequencies in the epicyclic case or can be determined with `AGAMA`. The denominator of f_{jml} may lead to a divergence in the DF when it approaches zero. Following our notation in Eq. 2.9, it can

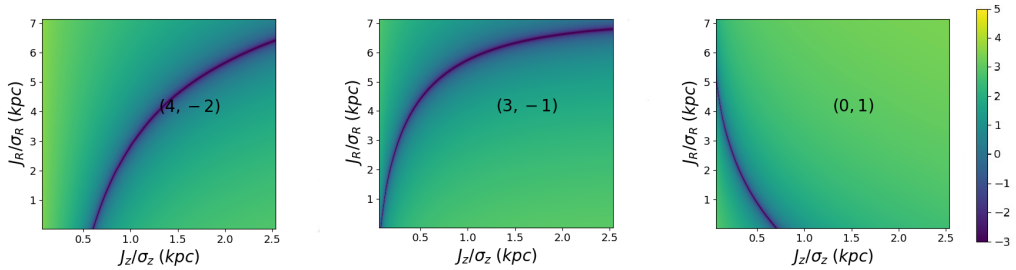

FIGURE 3.3: Values of $\log(\omega_{s,jml})$ in the (J_R,J_z) plane with fixed $J_\varphi = 1759$ kpc km s^{-1} for different (j,l) resonances. The pattern speed Ω_p is that of our fiducial central bar fixed at $1.89\,\Omega_0$. The two actions are renormalized by the radial velocity dispersion and the vertical velocity dispersion of the thin disc at the Sun, respectively. The deep blue lines correspond to resonance zones. Most combinations of indices explored did not give rise to any relevant resonant zone in the region of interest.

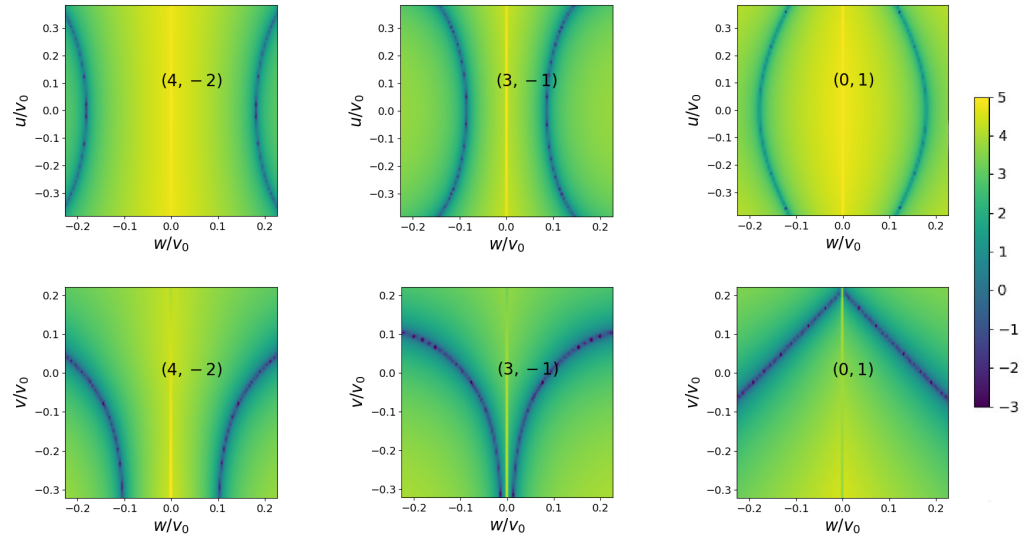

FIGURE 3.4: Values of $log(\omega_{s,jml})$ in the uw-plane and vw-plane. Top row: Values of $log(\omega_{s,jml})$ at $z = 0$ in the uw-plane with fixed $J_\varphi = 1759$ kpc km s^{-1}, for the various vertical resonances relevant in the solar neighbourhood (the $l = 0$ resonances are treated in detail in Sect. 3.3). They all appear at relatively large values of w and are very concentrated in w, varying very quickly in u as a function of w. Bottom row: Values of $log(\omega_{s,jml})$ in the vw-plane with fixed $u = 0$ km s^{-1}. The pattern speed Ω_p is that of our fiducial central bar fixed at $1.89\,\Omega_0$.

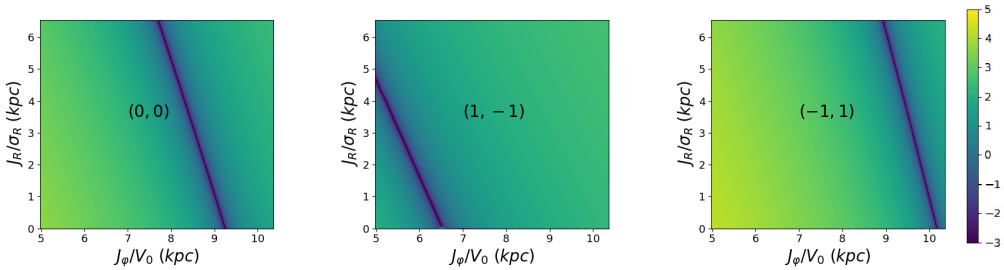

FIGURE 3.5: Same as Fig. 3.2, but with some combinations of indices giving rise to resonant zones for $\Omega_p = 0.84\,\Omega_0$.

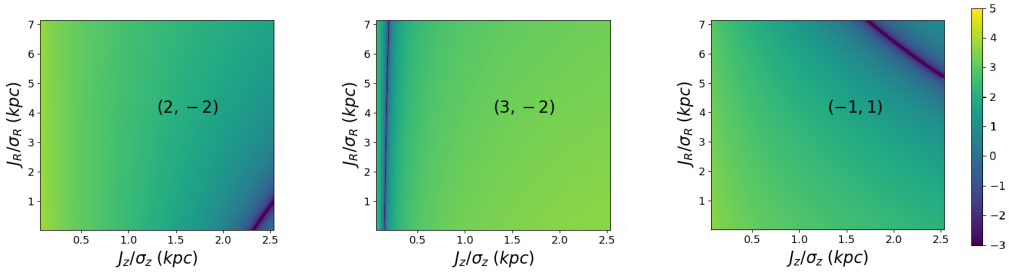

FIGURE 3.6: Same as Fig. 3.3, but with some combinations of indices giving rise to resonant zones for $\Omega_p = 0.84\,\Omega_0$.

be expressed as

$$\omega_{s,jml}(J_R, J_\varphi, J_z) = j\omega_R + m(\omega_\varphi - \Omega_p) + l\omega_z. \tag{3.6}$$

The amount of the resonances is limited in the epicyclic case because, by construction, indices run only over the values $j = \{-1, 0, 1\}$ and $l = \{-2, 0, 2\}$, but they can be much more numerous in the more accurate `AGAMA` case. For the bar potential of Eq. 2.11 and Eq. 2.12, and choosing a pattern speed $\Omega_p = 1.89\Omega_0$ as for our fiducial bar model, we explore in Fig. 3.2 and Fig. 3.3, the values of $\omega_{s,jml}(J_R, J_\varphi, J_z)$ in action space when varying the pair of integer indices (j, l). The actions are renormalized by the radial velocity dispersion of the thin disc, circular velocity, and vertical velocity dispersion of the thin disc at the Sun, respectively, to only display a relevant range of actions. Exploring indices in the range $[-4, +4]$, it is clear that most combinations do not induce a resonance that is relevant to the dynamics of the solar neighbourhood. We only display in Fig. 3.2 and Fig. 3.3 the combination of indices (in addition to the corotation) for which a resonant zone appears in the plotted region of action space. It is clear that very few low-order resonances are indeed present in the range of actions that are truly relevant for the solar neighbourhood.

To date our method has not been adapted to the projection of the DF on a plane in action space or local velocity space, and therefore works best in 3D. Therefore, we show in Fig. 3.4 some slices in velocity space at $z = 0$, denoting the location of the vertical resonances (i.e. resonances involving a non-zero l, hence involving the vertical frequency) either for a fixed value of the azimuthal velocity (and action) or for a fixed value of the radial velocity. Identifying such resonances in the vw-plane and uw-plane should allow new types of constraints to be put on the pattern speed of internal perturbers and the vertical shape of the potential of the Galaxy.

Interestingly, most of these resonances are very concentrated in w and vary quickly both in u and v as a function of w, making them elusive to find when stacking tracer stars in any 2D plane of velocity space, but in principle they stand out in thin slices of velocity space. Concretely, when considering a change of 10 km s^{-1} in vertical velocity from 5 to 15 km s^{-1}, the corresponding change in the location of the vertical resonance in v within the uv-plane is always larger than 10 km s^{-1} and typically larger (sometimes much larger) than 30 km s^{-1}.

Moreover, the signature of these vertical resonances in the uv-plane is rather thin, typically of the order of the km s^{-1}, hence much thinner than the displacement of the resonance with w. This means that, when investigating the uv-plane, vertical resonances should mostly be washed out as soon as the investigated slice is thick enough. Therefore, when investigating the DF in the uv-plane in the next subsection, we limit ourselves to the effect of $l = 0$ resonances.

As displayed in Fig. 3.5 and Fig. 3.6, for a lower pattern speed $\Omega_p = 0.84\,\Omega_0$, corresponding to the pattern speed of our fiducial spiral potential, a smaller number of vertical resonances are prominent in the solar neighbourhood.

While a specific treatment is needed in these resonant zones (e.g. Monari et al., 2017a), the signature of the resonances (and thus their location in velocity space) can clearly be identified with our linear perturbation method, and the linear perturbation treatment hereafter should accurately describe the deformations of velocity space outside of these resonant zones.

3.3 Comparing the perturbed DF for different action estimates

We are now in a position to compare the linear deformation of local velocity space for different action estimates, namely the epicyclic case used in previous works and the more accurate `AGAMA` action estimates. Since our method works best for now in 3D velocity space, we limit ourselves to slices of zero vertical velocity at different heights and to $l = 0$ resonances.

Figure 3.7 displays the $f_0 + f_1$ linearly perturbed distribution function at the position of the Sun in the Galactic plane for the bar potential of Sect. 2.4 and two different pattern speeds, and for the spiral potential of Sect. 2.5. As in Monari et al. (2017b), whenever $f_1 > f_0$, we cap f_1 at the value of f_0 to roughly represent the resonant zone. The more rigorous approach, which we leave to further work in the context of `AGAMA` actions (Al Kazwini et al., in prep.), is to treat the DF with the method of Monari et al. (2017a) in these regions. However, while the DF within the resonant zone is not well modelled by the present method, the *location* and global shape of resonances should be well reproduced. We indeed highlight in Fig. 3.7 the zone occupied by trapped orbits at the corotation ($\Omega_b = 1.16\,\Omega_0$) and OLR ($\Omega_b = 1.89\Omega_0$) of the bar, as determined with the method of Monari et al. (2017a) both in the epicyclic and `AGAMA` cases (Al Kazwini et al. in prep.). While the *quantitative* enhancement of the DF will be slightly different from our linear treatment in these trapping zones, it is clear that the location of the resonant deformation is well captured by the method, as expected. The linear deformation outside of the resonant zones should be well described by our method as well. Interestingly enough, the linear deformation due to

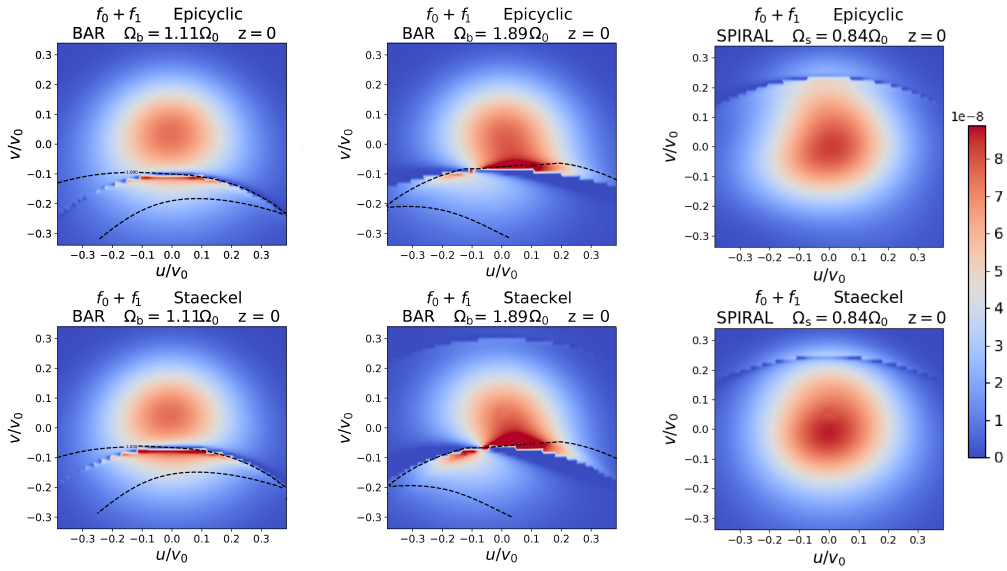

FIGURE 3.7: Distribution function from Fig. 3.1 in velocity space at the solar position within the Galactic plane, now perturbed to linear order by a bar (perturbing potential from Sect. 2.4) with pattern speeds $\Omega_b = 1.16\,\Omega_0$ (left) and $\Omega_b = 1.89\Omega_0$ (middle), or by a spiral pattern (perturbing potential from Sect. 2.5) with pattern speed $\Omega_{sp} = 0.84\,\Omega_0$ (right). The black dashed contours represent the zones where k is equal to or less than 1, k being a quantity computed in Monari et al. (2017a) that designates the region where the orbits are trapped at the main resonance (the computation used here in the Stäckel case will be presented in detail in Al Kazwini et al., in preparation). Top row: Epicyclic approximation. Bottom row: Stäckel fudge.

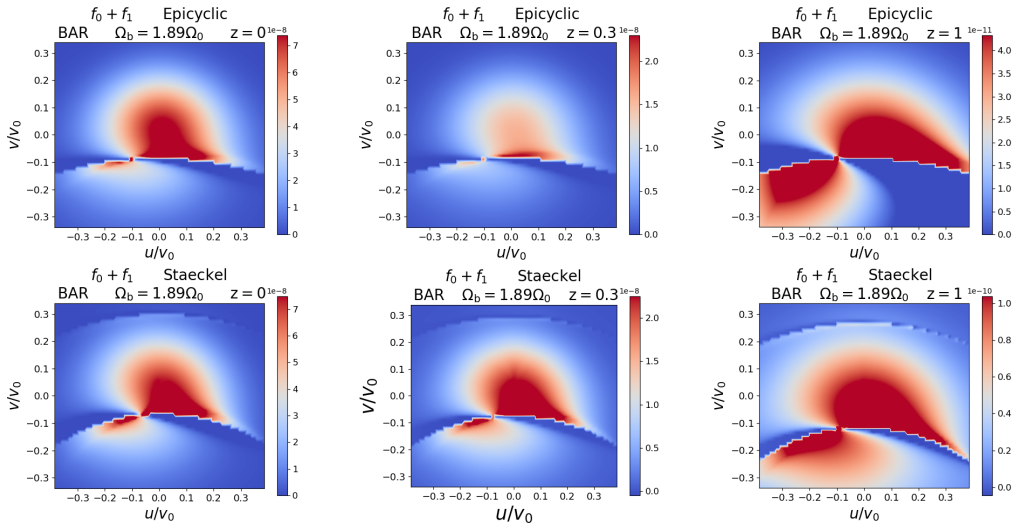

FIGURE 3.8: Local stellar velocity distribution perturbed to linear order at the solar galactocentric radius and azimuth at three different heights (left: $z = 0$ kpc, middle: $z = 0.3$ kpc, right: $z = 1$ kpc), when perturbed by a bar (perturbing potential of Sect. 2.4) with pattern speed $\Omega_b = 1.89\Omega_0$. Top row: Epicyclic approximation. Bottom row: Stäckel fudge. The scale of the colour bar is different in the upper and lower panels for $z = 1$ kpc.

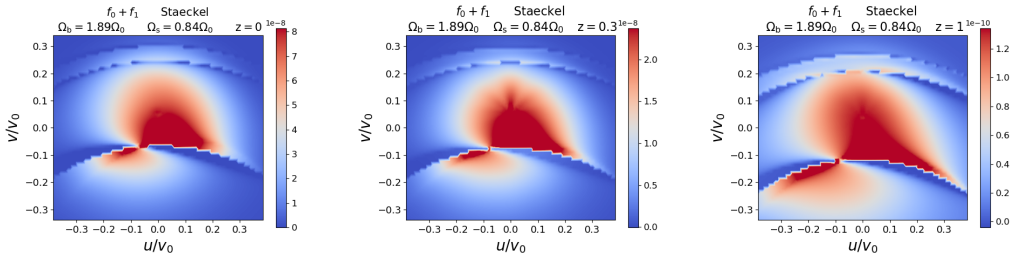

FIGURE 3.9: Same as Fig. 3.8, in the Stäckel fudge case, but now for joint perturbation by a bar (perturbing potential of Sect. 2.4) with pattern speed $\Omega_b = 1.89\Omega_0$ and a spiral pattern (perturbing potential of Sect. 2.5) with pattern speed $\Omega_{\rm sp} = 0.84\,\Omega_0$.

the bar is generally stronger in the AGAMA case, and that due to the spiral is weaker in the AGAMA case. This means that reproducing the effect of spiral arms on the local velocity distribution might require a higher amplitude when considering an accurate estimate of the action-angle variables rather than the epicyclic approximation. We speculate that this is related to the inaccuracy of the reconstruction of the potential in the epicyclic case, which causes different biases in the spiral and bar cases.

The case of the pattern speed of the bar being $1.89\,\Omega_0$ would correspond to a configuration where the Hercules stream at negative u and negative v corresponds to the $2:1$ outer Lindblad resonance of the bar (e.g. Dehnen, 2000; Minchev, Nordhaus, and Quillen, 2007; Monari et al., 2017b; Fragkoudi et al., 2019). Although this happens in the resonant zone, it is interesting to note that this feature is less squashed in the more realistic AGAMA case. Moreover, a resonance unnoticed within the epicyclic approximation appears at high azimuthal velocities: we can identify this resonance as the outer $1:1$ resonance of the bar (Dehnen, 2000). In the spiral case, the resonant ridge at large azimuthal velocities can be identified as the corotation of the spiral pattern.

Figure 3.8 displays the linear deformation due to the bar, for the case of pattern speed of $1.89\,\Omega_0$, at different heights above the Galactic plane, both in the epicyclic and AGAMA cases. We again restrict ourselves to a zero vertical velocity slice and $l = 0$ resonances. As can be seen in this figure, the epicyclic approximation quickly becomes imprecise at large heights because it implies a stronger falloff of the density with height (as already noted in Fig. 3.1) while not changing the azimuthal velocity distribution (and the location of resonances in v) due to the hypothesis of complete decoupling of vertical motions.

In the AGAMA case the azimuthal velocity distribution is affected by a larger asymmetric drift at large heights, and the location of the outer Lindblad resonance of the bar in the uv-plane is also displaced to lower azimuthal v at larger heights. This occurs because at fixed J_φ the azimuthal and radial frequencies computed with AGAMA are lower at higher z, meaning that one needs to reach lower J_φ (corresponding to orbits whose guiding radii are in the inner Galaxy) to reach the resonance.

This trend is most clearly visible at $z = 1$ kpc, where the epicyclic approximation does not accurately represent the location of the Hercules feature compared to the AGAMA case. Interestingly, comparing the displacement with height of the OLR in the case of a bar with pattern speed $1.89\,\Omega_0$ with that of the corotation in the case of a $1.16\,\Omega_0$ pattern speed, we noted that the corotation location in the uv-plane is

more displaced than the OLR. This is because the corotation only depends on the azimuthal frequency, while the OLR depends on a combination of the azimuthal and radial frequencies. On the other hand, with the presently assumed background potential, we found that the displacement with height was rather independent of the pattern speed and therefore of the location of the resonance in local velocity space. We found a gradient in v of 8 $\mathrm{kms}^{-1}\mathrm{kpc}^{-1}$ for the corotation, 6 $\mathrm{kms}^{-1}\mathrm{kpc}^{-1}$ for the OLR, and 4 $\mathrm{kms}^{-1}\mathrm{kpc}^{-1}$ for the $1:1$ resonance. This different displacement can also be seen when linearly adding the effect of the bar and spiral in Fig. 3.9, where the spacing between the $1:1$ resonance of the bar and that of the corotation of the spiral increases with height.

Quantitatively, these displacements depend strongly on the background Galactic potential. This means that once the resonances potentially responsible for moving groups in the solar neighbourhood have been identified, studying their position in the uv-plane as a function of z can in principle be a powerful new way to constrain the 3D structure of the Galactic potential. This cannot be done within the epicyclic approximation. We note that marginalizing over vertical velocities instead of taking a zero-velocity slice would not compensate for these variations of the location of resonances with height but would only enhance the effect. In practice, we investigated the displacement of the location of the in-plane OLR with vertical velocities. For $w = 50$ km s^{-1} the displacement compared to $w = 0$ km s^{-1} in terms of the v-location of the resonance at $z = 1$ kpc is 8 km s^{-1} , always towards lower azimuthal velocities; however, the signal will always be dominated by the lowest w values due to the vertical orbital structure of the disc.

Chapter 4

Temporal evolution of the perturber

Previously, we always considered a constant amplitude for the perturbing potential in order to determine an analytical expression for the perturbed DF. Here, we investigate the time dependence of the DF by choosing a time-varying amplitude for the perturbing potential.

4.1 Time-varying amplitude function

The expression we use for the time-dependent function g controlling the amplitude of the perturbation during its growth is

$$g(t) = \frac{1 - \cos\left(\pi t / t_\mathrm{f}\right)}{2}, \tag{4.1}$$

where t_f is the time at which the perturbation is completely formed, expressed in Gyr. We consider $t_\mathrm{f} = 0.5$ Gyr.

The motivation for this choice of growth function is its analytic simplicity, having a function starting from exactly zero at the origin, and smooth over the whole considered range. The first derivative, $\left[\pi/\left(2t_\mathrm{f}\right)\right]\sin\left(\pi t/t_\mathrm{f}\right)$, assures the continuity at 0 and t_f with both stages, fixed at 0 for $t \leq 0$ and at 1 for $t \geq t_\mathrm{f}$ (the first derivative is thus equal to 0 at 0 and t_f).

4.2 Time-dependent perturbed distribution function

We now take the integral of Eq. (2.6), restricted to $[0, t]$ (because the g function is equal to 0 on $]-\infty, 0]$) and integrate by parts. We take $\phi_{\boldsymbol{n}}(\boldsymbol{J}', t') = g(t')\, h(t')\, \phi_{\boldsymbol{n}}(\boldsymbol{J})$, with $h(t') = \mathrm{e}^{-\mathrm{i}m\Omega_\mathrm{p}t'}$, and we define

$$\eta(t) \equiv \frac{\mathrm{e}^{\mathrm{i}\theta_{\mathrm{s},\boldsymbol{n}}(t)}}{\mathrm{i}\omega_{\mathrm{s},\boldsymbol{n}}} \rightarrow \mathrm{d}\eta = \mathrm{e}^{\mathrm{i}\theta_{\mathrm{s},\boldsymbol{n}}(t)}\mathrm{d}t, \tag{4.2}$$

allowing us to rewrite Eq. (2.6) as

$$f_1(\boldsymbol{J}, \boldsymbol{\theta}, t) = \mathrm{Re}\left\{ \mathrm{i}\frac{\partial f_0}{\partial \boldsymbol{J}}(\boldsymbol{J}) \cdot \sum_{\boldsymbol{n}} \boldsymbol{n}\phi_{\boldsymbol{n}}(\boldsymbol{J}) \int_0^t g(t')\frac{\mathrm{d}\eta}{\mathrm{d}t'}(t')\,\mathrm{d}t' \right\}. \tag{4.3}$$

We can now integrate by parts

$$\int_0^t g(t')\frac{\mathrm{d}\eta}{\mathrm{d}t'}(t')\,\mathrm{d}t' = [g(t')\eta(t')]_0^t - \int_0^t \frac{\mathrm{d}g}{\mathrm{d}t'}(t')\,\eta(t')\,\mathrm{d}t', \tag{4.4}$$

and since $g(0) = 0$,

$$[g(t')\eta(t')]_0^t = g(t)\eta(t). \tag{4.5}$$

To calculate the second part of the integral, since $\mathrm{d}g(t)/\mathrm{d}t = \pi/(2t_\mathrm{f})\sin(\pi t/t_\mathrm{f})$, we write,

$$\int_0^t \frac{\mathrm{d}g}{\mathrm{d}t'}(t')\eta(t')\mathrm{d}t' = \frac{\pi}{2t_\mathrm{f}}\frac{1}{\mathrm{i}\omega_{\mathrm{s},\boldsymbol{n}}}\int_0^t \sin\left(\frac{\pi t'}{t_\mathrm{f}}\right)\mathrm{e}^{\mathrm{i}\theta_{\mathrm{s},\boldsymbol{n}}(t')}\mathrm{d}t'. \tag{4.6}$$

We look for a primitive G of $\sin(\pi t/t_\mathrm{f})\mathrm{e}^{\mathrm{i}\theta_{\mathrm{s},\boldsymbol{n}}(t)}$ of the form

$$G(t) = \left[A\cos\left(\frac{\pi t}{t_\mathrm{f}}\right) + B\sin\left(\frac{\pi t}{t_\mathrm{f}}\right)\right]\mathrm{e}^{\mathrm{i}\theta_{\mathrm{s},\boldsymbol{n}}(t)}. \tag{4.7}$$

Deriving $G(t)$ with respect to t, and equating it to the integrand in Eq. 4.6 we get

$$B\frac{\pi}{t_\mathrm{f}} + A\,\mathrm{i}\omega_{\mathrm{s},\boldsymbol{n}} = 0 \quad \text{and} \quad B\,\mathrm{i}\omega_{\mathrm{s},\boldsymbol{n}} - A\frac{\pi}{t_\mathrm{f}} = 1, \tag{4.8}$$

which leads to

$$A = \frac{\pi/t_\mathrm{f}}{\omega_{\mathrm{s},\boldsymbol{n}}^2 - (\pi/t_\mathrm{f})^2} \quad \text{and} \quad B = \frac{-\mathrm{i}\omega_{\mathrm{s},\boldsymbol{n}}}{\omega_{\mathrm{s},\boldsymbol{n}}^2 - (\pi/t_\mathrm{f})^2}. \tag{4.9}$$

Substituting the Eqs. (4.5) and (4.7) into Eq. (4.4) results in the following expression for the perturbed DF

$$\begin{aligned} f_1(\boldsymbol{J},\boldsymbol{\theta},t) = \mathrm{Re}\Bigg\{ & \frac{\partial f_0}{\partial \boldsymbol{J}}(\boldsymbol{J})\cdot\sum_{\boldsymbol{n}}\boldsymbol{n}\,\phi_{\boldsymbol{n}}(\boldsymbol{J})\times \\ & \Bigg[\frac{1}{2}\left(1-\cos\left(\frac{\pi t}{t_\mathrm{f}}\right)\right)\frac{\mathrm{e}^{\mathrm{i}\theta_{\mathrm{s},\boldsymbol{n}}}}{\omega_{\mathrm{s},\boldsymbol{n}}} - \frac{\pi}{2t_\mathrm{f}}\frac{1}{\omega_{\mathrm{s},\boldsymbol{n}}}\frac{1}{\omega_{\mathrm{s},\boldsymbol{n}}^2-(\pi/t_\mathrm{f})^2}\times \\ & \left(\left(\frac{\pi}{t_\mathrm{f}}\cos\left(\frac{\pi t}{t_\mathrm{f}}\right) - \mathrm{i}\omega_{\mathrm{s},\boldsymbol{n}}\sin\left(\frac{\pi t}{t_\mathrm{f}}\right)\right)\mathrm{e}^{\mathrm{i}\theta_{\mathrm{s},\boldsymbol{n}}} - \frac{\pi}{t_\mathrm{f}}\,\mathrm{e}^{\mathrm{i}(\theta_{\mathrm{s},\boldsymbol{n}}-\omega_{\mathrm{s},\boldsymbol{n}}t)}\right)\Bigg]\Bigg\}. \end{aligned} \tag{4.10}$$

It should be noted that we do not exactly recover the static case at $t = t_f$ because not *all* derivatives of $g(t)$ are strictly zero at the initial and final time, as assumed in M16. If a true plateau is reached after t_f in an analytic fashion, the function would nevertheless converge towards the static case. How quickly this would happen is not trivial to compute. We can however compute an upper limit based on the formalism of Monari et al. (2017a). Considering that the most trapped orbits have their slow variables following the behaviour of a harmonic oscillator, and taking 2π over the frequency of this harmonic oscillator as a characteristic time for phase-mixing, we obtain a characteristic time of the order of 2 Gyr.

Now we can study analytically how the linear response to a fiducial bar with

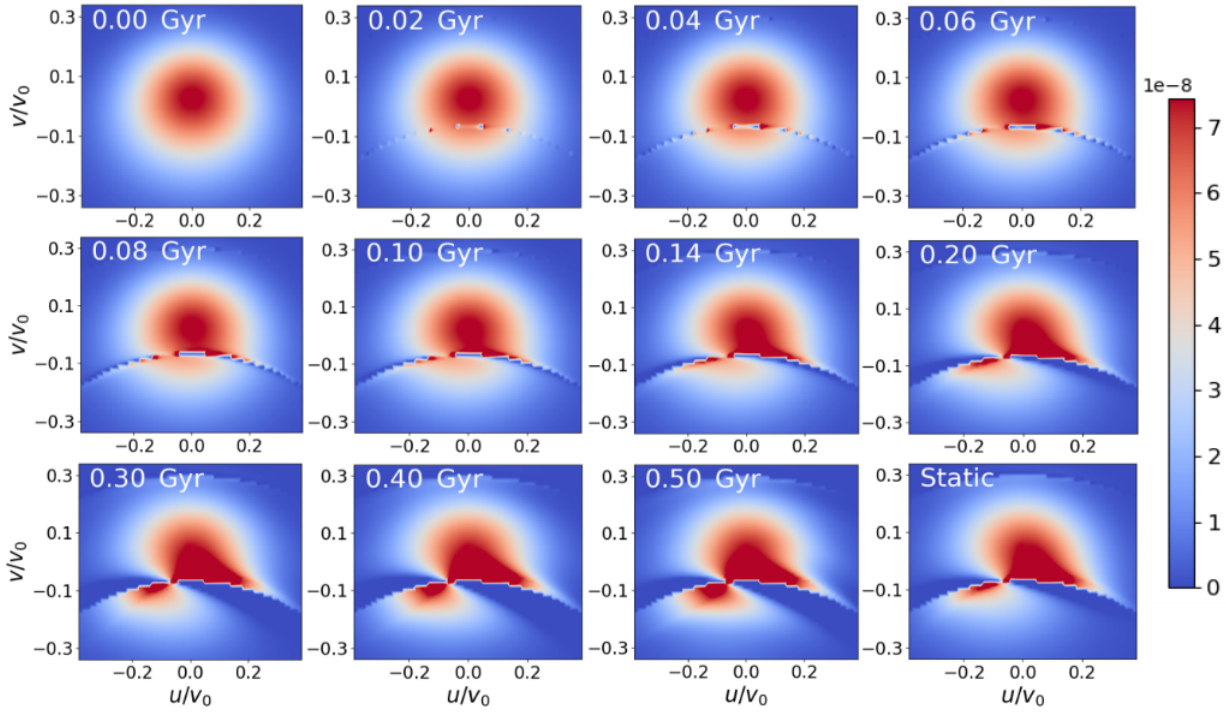

FIGURE 4.1: Local stellar velocity distribution perturbed to linear order in the Galactic plane by the bar of Sect. 2.4 with $\Omega_b = 1.89\Omega_0$ with the Stäckel fudge, and an amplitude of the bar growing as described in Sect. 4.1. The first 11 panels display the temporal evolution of the perturbation. The last panel displays the stationary case. The amplitude of the bar goes from 0 at $t = 0$ to its plateau ($g(t) = 1$) at $t = 0.5$ Gyr.

$\Omega_b = 1.89\Omega_0$ evolves with time. As before the method is not strictly valid at resonances, where a treatment like that used in Monari et al. (2017a) must be applied (see also Binney, 2020a; Binney, 2020b). It is nevertheless interesting to see in Fig. 4.1 how the linear deformation of the velocity plane evolves with time near resonances (in a patch co-moving with the bar, hence at a constant azimuthal angle to the bar), while the amplitude of the perturbation grows. The effect of the OLR appears as soon as the perturbation starts to grow. As it progressively grows, the two linear modes in the DF separate and lead to a velocity plane already very much resembling the stationary form of the perturbed DF after 0.25 Gyr, that is when $g(t) = 0.5$ and the perturbation is half-formed. In the absence of a pattern speed variation, it is therefore not necessarily obvious to disentangle the effect of a bar whose amplitude is growing from that of a fully formed bar with larger and constant amplitude.

Chapter 5

Trapping at resonances with accurate action estimates

In the previous chapters, we treated explicit distribution functions for the disc as a function of the actions and angles of the unperturbed axisymmetric system. An Eulerian approach was assumed which allowed us to probe the effect of the bar and stationary spiral arms away from the main resonances. Although this 'Eulerian' approach (keeping the actions and angles of the unperturbed systems) allowed us to gain qualitative insights on the effects of non-axisymmetries near resonances, no quantitative assessments within resonant zones can be made because the linear treatment diverges at resonances.

To go further, we adopt now the 'Lagrangian' formalism presented in Monari et al., 2017b (deforming the tori to define a new system of angles and actions coordinates in the resonant zones). However, the results in Monari et al., 2017b were obtained using the epicyclic approximation whereas here we use the Stäckel approach using Agama.

This problem is tackled here by adjusting the Lagrangian approach to the impact of non-axisymmetries at resonances. The deformation of the orbital tori is modeled outside of the trapping region, and new tori are constructed, with an adequate system of angle-action variables, within the trapping region. The unperturbed distribution function is then phase-averaged over the new tori.

The background axisymmetric potential is again chosen to be Model I from Binney and Tremaine (2008). The potential for the bar is again the same simple quadrupole potential (Weinberg, 1994; Dehnen, 2000) with

$$\Phi_{1,\mathrm{b}}(R,z,\varphi,t) = \mathrm{Re}\left\{\Phi_{\mathrm{a,b}}(R,z)\mathrm{e}^{\mathrm{i}m(\varphi-\varphi_{\mathrm{b}}-\Omega_{\mathrm{b}}t)}\right\}, \tag{5.1}$$

where $m = 2$, Ω_{b} is the pattern speed of the bar, and the azimuth is defined with respect to a line corresponding to the Galactic centre-Sun direction in the Milky Way, φ_{b} thus being the angle between the Sun and the long axis of the bar. We also choose

$$\Phi_{\mathrm{a,b}}(R,z) = -\alpha_{\mathrm{b}}\frac{v_0^2}{3}\left(\frac{R_0}{R_{\mathrm{b}}}\right)^3\left(\frac{R}{r}\right)^2\begin{cases}\left(\dfrac{r}{R_{\mathrm{b}}}\right)^{-3} & R \geq R_{\mathrm{b}},\\ 2-\left(\dfrac{r}{R_{\mathrm{b}}}\right)^3 & R < R_{\mathrm{b}},\end{cases} \tag{5.2}$$

where $r^2 = R^2 + z^2$ is the spherical radius, R_{b} is the length of the bar, and α_{b} represents the maximum ratio between the bar and axisymmetric background radial

forces at the Sun's galactocentric radius $R = R_0$. We use hereafter, as a representative example, $R_b = 0.625\,R_0$, $\varphi_b = 25^o$, and $\alpha_b = 0.01$.

We rewrite the perturbing potential as a Fourier series in terms of actions and angles

$$\Phi_1(J_R, J_\varphi, \theta_R, \theta_\varphi) = \mathrm{Re}\left\{\sum_j c_{jm} e^{i(j\theta_R + m(\theta_\varphi - \Omega_b t}\right\}. \tag{5.3}$$

In the epicyclic case as is presented in Monari et al., 2017b, the Fourier coefficients are restricted to $j = -1, 0, 1$ by construction. In contrast, in this thesis, the coefficients are numerically evaluated using AGAMA. This procedure is described in detail in section 2.2 . A new set of coordinates dubbed "slow" and "fast" are introduced via the equations

$$\theta_s = l\theta_R + m(\theta_\phi - \Omega_b t),\ J_\phi = mJ_s \tag{5.4}$$

$$\theta_f = \theta_R,\ J_R = lJ_s + J_f \tag{5.5}$$

where l denotes the resonance, $l = 0$ for the corotation resonance, $l = -1$ for the inner Lindblad resonance and $l = 1$ for the outer Lindblad resonance. By taking the time derivative of θ_s, we can see that this angle evolves slowly near a resonance since at a resonance

$$l\Omega_R + m(\Omega_\phi - \Omega_b) = 0 \tag{5.6}$$

In the new coordinate system, the motion is described by the Hamiltonian

$$H = H_0 + \mathrm{Re}\left\{\sum_j c_{jm} e^{i[(j-l)\theta_f + \theta_s]}\right\} - m\Omega_b J_s \tag{5.7}$$

where H_0 is the Hamiltonian of the unperturbed axisymmetric potential and the c_{jm} are the Fourier coefficients from Eq. 5.3. We then average H along θ_f to obtain

$$\bar{H} = H_0(J_f, J_s) - m\Omega_b J_s + \mathrm{Re}\{\sum_j c_{lm} e^{i\theta_s}\} \tag{5.8}$$

In this formalism, J_f is an integral of motion. For each value of J_f, we define $J_{s,res}$ as the value of J_s where

$$\Omega_s(J_f, J_{s,res}) = 0 \tag{5.9}$$

We can then obtain the approximate Hamiltonian near the resonances

$$\hat{H} = \frac{1}{2}G(J_s - J_{s,res})^2 - Fcos(\theta_s + g) \tag{5.10}$$

where

$$F = -|c_{lm}(J_f, J_{s,res})|,\ G = \frac{\partial \Omega_s}{\partial J_s}(J_f, J_{s,res}) \tag{5.11}$$

and $g = arg(c_{lm}(J_f, J_{s,res}))$. The Hamiltonian in Eq. 5.10 is the Hamiltonian of a pendulum. The corresponding equations of motion are

$$\dot{\theta}_s = G(J_s - J_{s,res}) \tag{5.12}$$

$$\dot{J}_s = -Fsin(\theta_s + g) \tag{5.13}$$

We then obtain

$$\ddot{\theta}_s = -\omega_0^2 cos(\theta_s + g) \tag{5.14}$$

where $\omega_0^2 = FG$. The energy of the pendulum is

$$E_p = \frac{\dot{\theta}_s^2}{2} + V_p(\theta_s) \tag{5.15}$$

where

$$V_p(\theta_s) = -\omega_0^2 cos(\theta_s + g) \tag{5.16}$$

We can then define the quantity

$$k = \sqrt{\frac{1}{2}(1 + \frac{E_p}{\omega_0^2})} \tag{5.17}$$

When $k < 1$, the orbit is trapped and librates around $\theta_s = -g$.

The action and the angle associated to the pendulum are

$$J_p = \frac{4}{pi}\frac{J_a}{k}[E(k^2) - (1-k^2)K(k^2)] \tag{5.18}$$

$$\theta_p = \frac{pi}{2K(k^2)} cn^{-1}(\frac{J_s - J_{s,res}}{J_a}, k^2) \tag{5.19}$$

where $J_a = 2\sqrt{F/G}k$, the elliptic functions E and K are defined as

$$E(m) = \int_0^{\pi/2} d\theta \sqrt{1 - msin^2\theta} \tag{5.20}$$

$$K(m) = \int_0^{\pi/2} \frac{d\theta}{\sqrt{1 - msin^2\theta}} \tag{5.21}$$

and $cn(u,m) = cos(\phi)$ where

$$u = \int_0^{\phi} \frac{d\theta}{\sqrt{1 - msin^2\theta}} \tag{5.22}$$

Finally, we get the perturbed distribution function in the trapping region with the equation

$$f_{tr}(J_f, J_s, \theta_s) = \frac{1}{2\pi}\int_0^{2\pi} f_0(J_f, J_{s,res} + \Delta J_s(\theta_p))d\theta_p \tag{5.23}$$

where

$$\Delta J_s = J_a cn(\frac{2}{\pi}K(k^2)\theta_p, k^2) \tag{5.24}$$

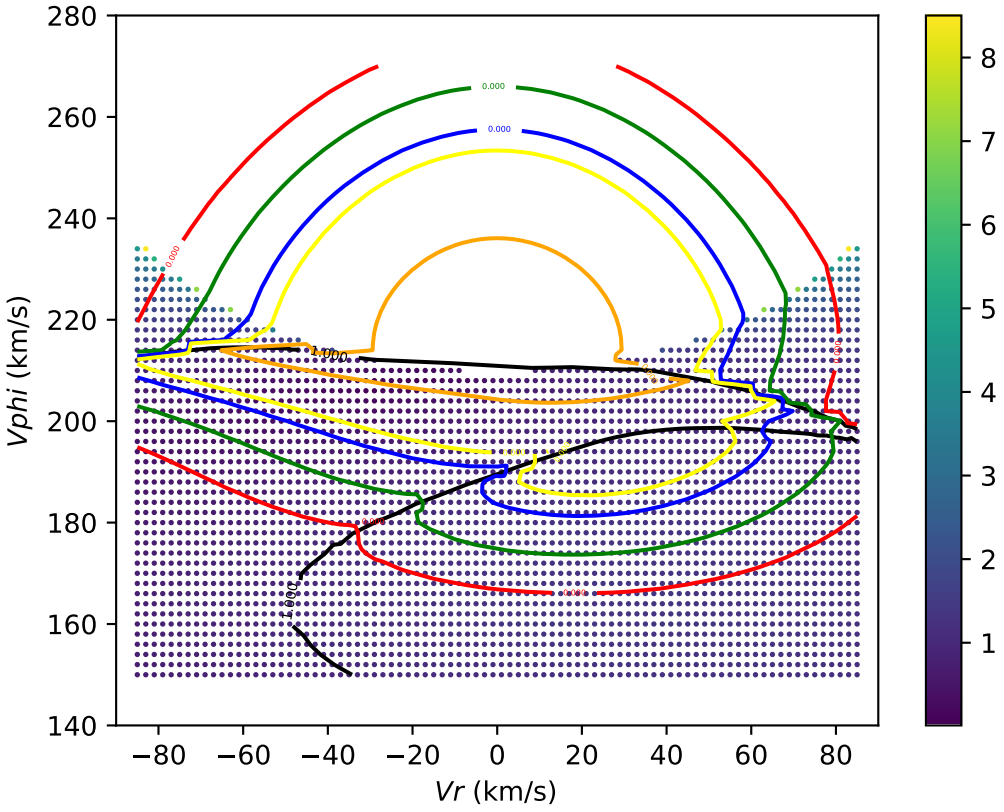

FIGURE 5.1: Constant distribution function contours at $R = 8\ kpc$ and at $\phi = 30°$ for the Outer Lindblad resonance (l = 1) in the epicyclic approximation.

and f_0 is the unperturbed distribution function. The perturbed function in the trapping region can be computed numerically using the equation

$$f_{tr}(J_f, J_s, \theta_s) = \frac{1}{N} \sum_i f_0(J_f, J_{s,res} + \Delta J_s(\theta_p^i)) \tag{5.25}$$

where θ_p^i sample the orbit between 0 and 2π and N is the number of sampling points.

In the zone of circulation (k > 1), the distribution function takes the form

$$f_{circ}(J_f, J_s, \theta_s) = f_0(J_f, \bar{J}_s) \tag{5.26}$$

where

$$\bar{J}_s = J_{s,res} + \frac{\pi}{2} \frac{J_a}{K(1/k^2)} \tag{5.27}$$

Using the same background distribution function introduced in Sect. 3.1, we can then compute the perturbed distribution function in both the epicyclic and AGAMA cases.

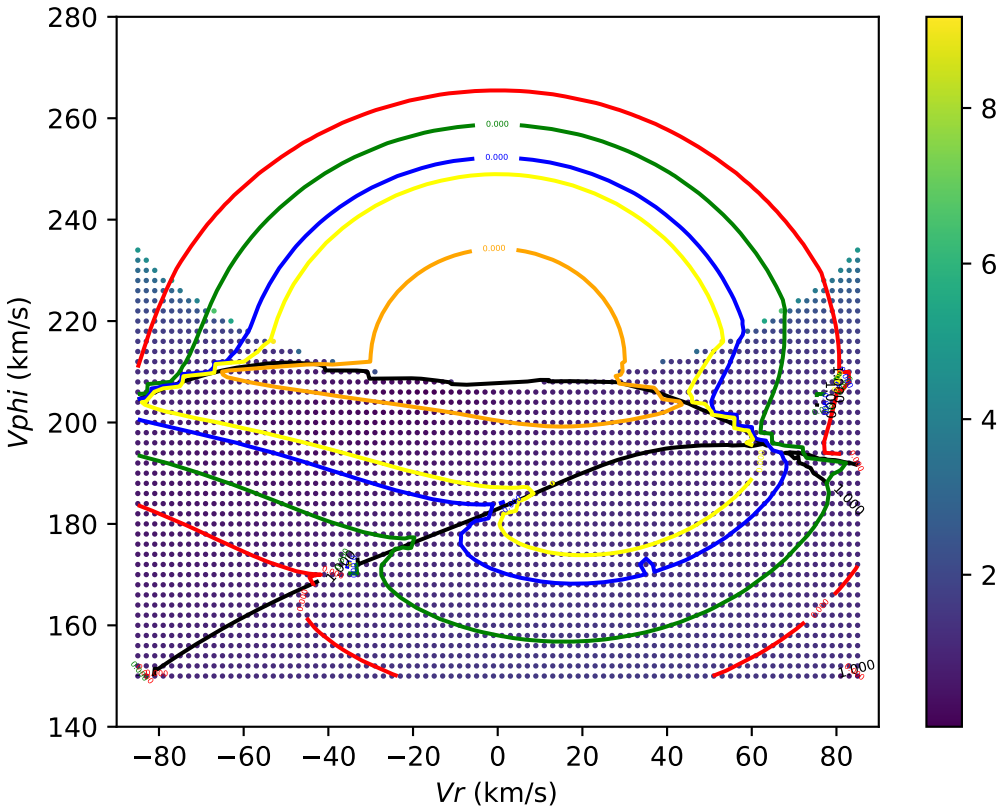

FIGURE 5.2: The same as above in the AGAMA case.

Chapter 6

A first application: locating moving groups with Gaia EDR3

This Chapter is based on the paper led by Marcel Bernet "From ridges to manifolds: 3D characterization of the moving groups in the Milky Way disc", to which I contributed as a co-author.

Moving groups, which are overdensities in the stellar velocity distribution, are a very important tool to understand the structure of the Milky Way. They can be connected to the orbital resonances of the bar and the spiral arms (Dehnen, 2000; Monari et al., 2019b) or to phase mixing related to external perturbations (Minchev et al., 2009). These moving groups have been more precisely delineated with the latest releases of the Gaia mission. Dehnen, 2000 showed that the velocity distribution in the solar neighborhood can be attributed to the effect of the Outer Lindblad resonance in the case of a short/fast bar. Conversely, Monari et al., 2019b and D'Onghia and Aguerri, 2020 showed that the same features can be attributed to the effect of the co-rotation resonance in the case of a long/slow bar.

Ramos, Antoja, and Figueras, 2018 used the wavelet transform to study the kinematics of the moving groups. They claimed that some features may be connected to phase mixing while others to resonance effects. In particular, they claimed that the observed traits related to the Hercules moving group can be produced by the Outer Lindblad resonance of a short/fast bar. On the other hand, Monari et al., 2019b found that the changes in angular momentum with respect to azimuth for the Hercules group are consistent with what is predicted for the co-rotation resonance of a long/slow bar.

In Ramos, Antoja, and Figueras, 2018, the analysis was restricted to three variables, the radial and azimuthal velocities and one variable in space. Meanwhile, in the work to which this thesis contributed, the position of the moving groups is sampled in 3D position space coupled to the radial and azimuthal velocities. They are detected by using the wavelet transform in small independent volumes and an algorithm based on the Breadth-first search algorithm from Graph Theory. The test particle simulations are done with a fast $(\Omega_b = 50 kms^{(}-1) kpc^{(}-1))$ and a slow $(\Omega_b = 30 kms^{(}-1) kpc^{(}-1))$ bar and then compared to the data.

The manifolds tracing the main moving groups in the solar neighbourhood along the $(R, \phi, Z, V_R, V_\phi)$ space, are sampled in an automatic way with Gaia EDR3 6D data. The skeleton of the velocity distribution is revealed in a multidimensional space that we can then be explored along the radial direction, and characterized in the azimuth and vertical submanifolds. This methodology has been successfully tested with two simulations of the effects of a (dynamically young) bar. It was possible to

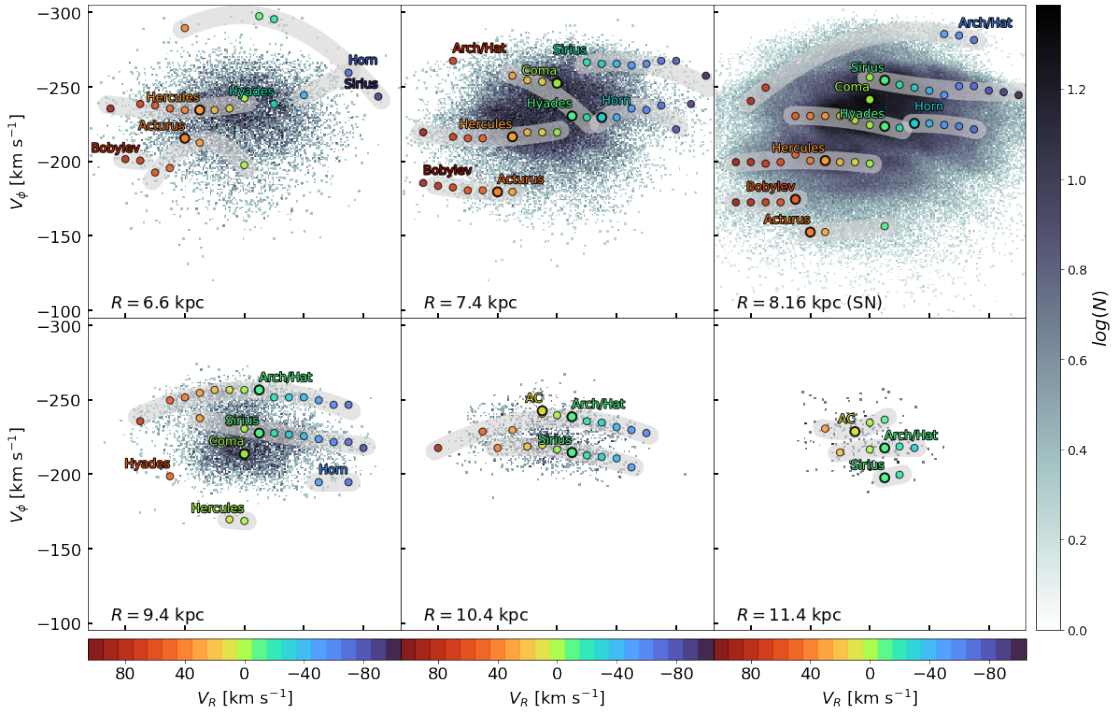

FIGURE 6.1: Moving group detection in different neighbourhoods along the radial direction. For each moving group, we include a parabolic fitting of the substructures associated with each group in a thick grey line. Each moving group contains several structures, corresponding to different V_R bins. The largest structure in each group is used as its representative (dots with larger black contours and the moving group name on top).

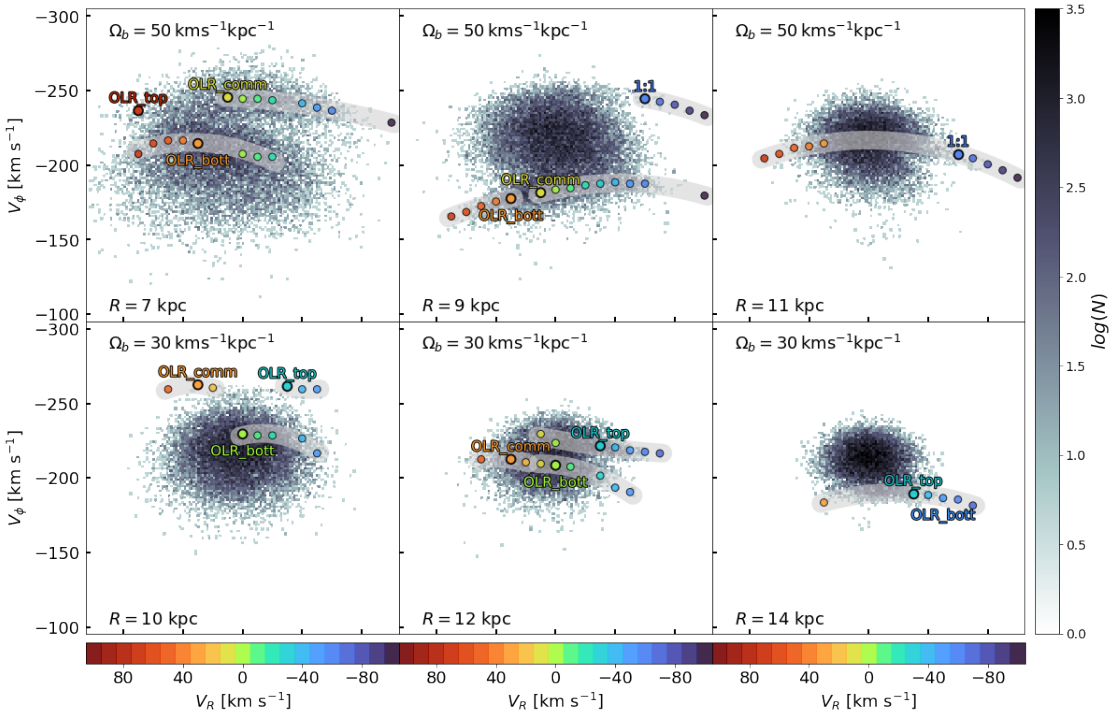

FIGURE 6.2: Moving group detection in different neighbourhoods along the radial direction in the simulations, analog to Fig. 6.1. Top row: fast bar model. Bottom row: slow bar model.

observe and quantify the spatial evolution of the observed moving groups in a large range of about 3 kpc around the sun. The main results and conclusions are:

- The azimuthal velocity of the moving groups in the radial direction does not follow lines of constant angular momentum, deviating from the naive first order prediction for resonances. In the simulations, resonant structures also deviate from this simple prediction, demanding more complex analytic predictions.

- The spatial evolution of the moving groups is complex. The moving groups configuration observed in the SN is not maintained throughout the disc. The relative position between the arches and their curvature changes across space, and the different moving groups split and merge several times. This is expected in a context of bifurcating orbital families, for example in the case of resonances.

- In our slow bar simulation, we observe a bi-modality created by the OLR in the outer parts of the disc. This bi-modality is also observed in the *Arch/Hat* moving group in the data. This intriguing agreement could favour the slow bar scenario, and opens the possibility of a test with future data.

- The *Acturus*, *Bobylev*, and *Hercules* moving groups present a positive slope of their V_ϕ location with the azimuth. We measure this slope to be -0.50 at $R = 8$ kpc for *Hercules*.

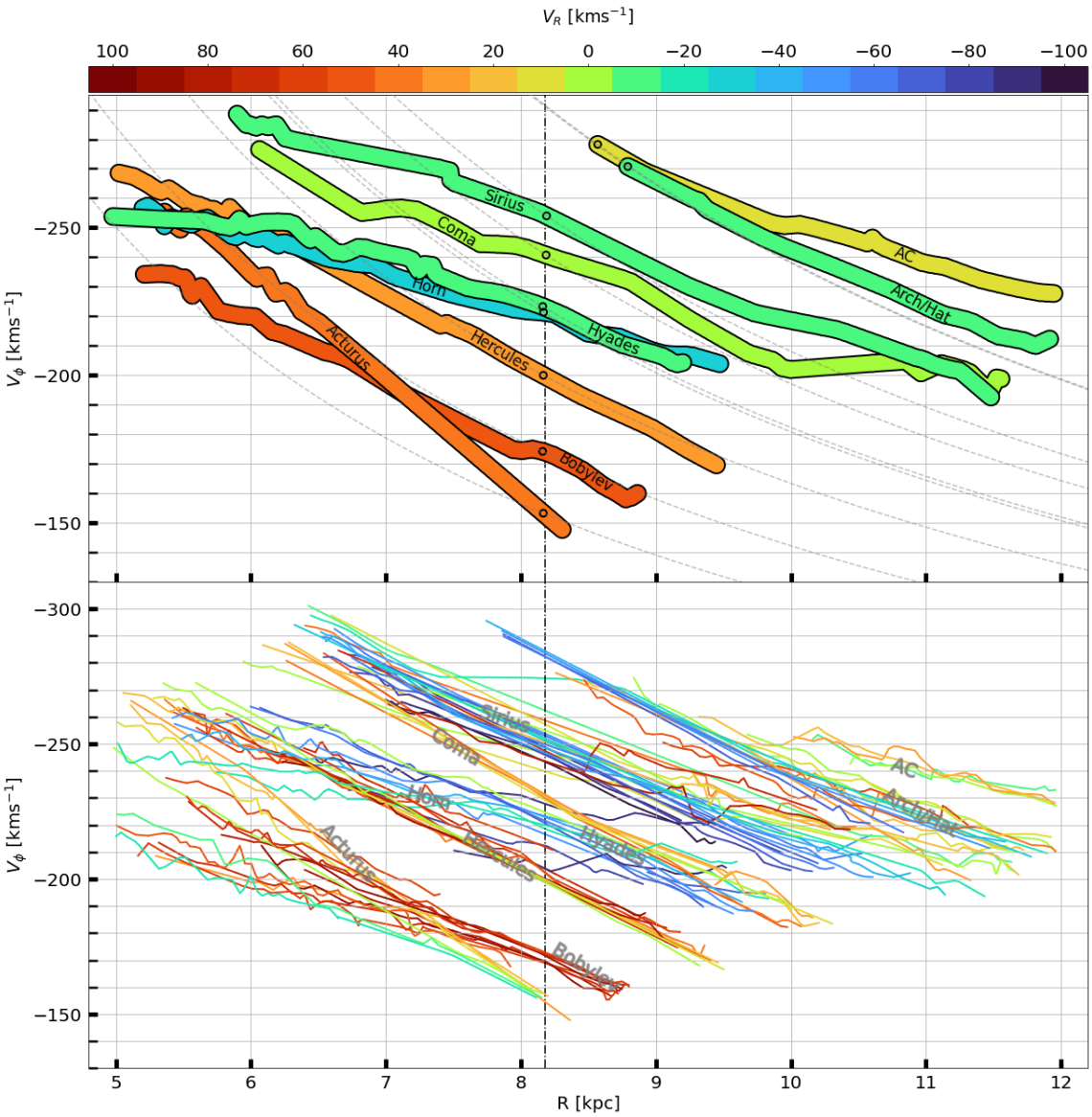

FIGURE 6.3: Azimuthal velocity of the kinematic substructures in the radial direction, $\phi = 0, Z = 0\ kpc$, as a function of the radius, and coloured by their radial velocity. The dashed grey lines correspond to constant angular momentum lines, crossing the moving groups at solar radius. Top: Structures corresponding to the main peak of a moving group, tagged with the name in literature. Bottom: Secondary peaks of the moving groups. The usual way to observe this projection is using the number of stars or the mean V_R in each bin. Using our methodology we can observe the skeleton of the distribution and its complexity. For instance, the slope of the moving groups at different V_R can be very different and the groups cross each other or share close regions in the diagram. In addition, the extension of the range of exploration shows that the moving group deviate from the constant vertical angular momentum predicted for small epicyclic amplitudes.

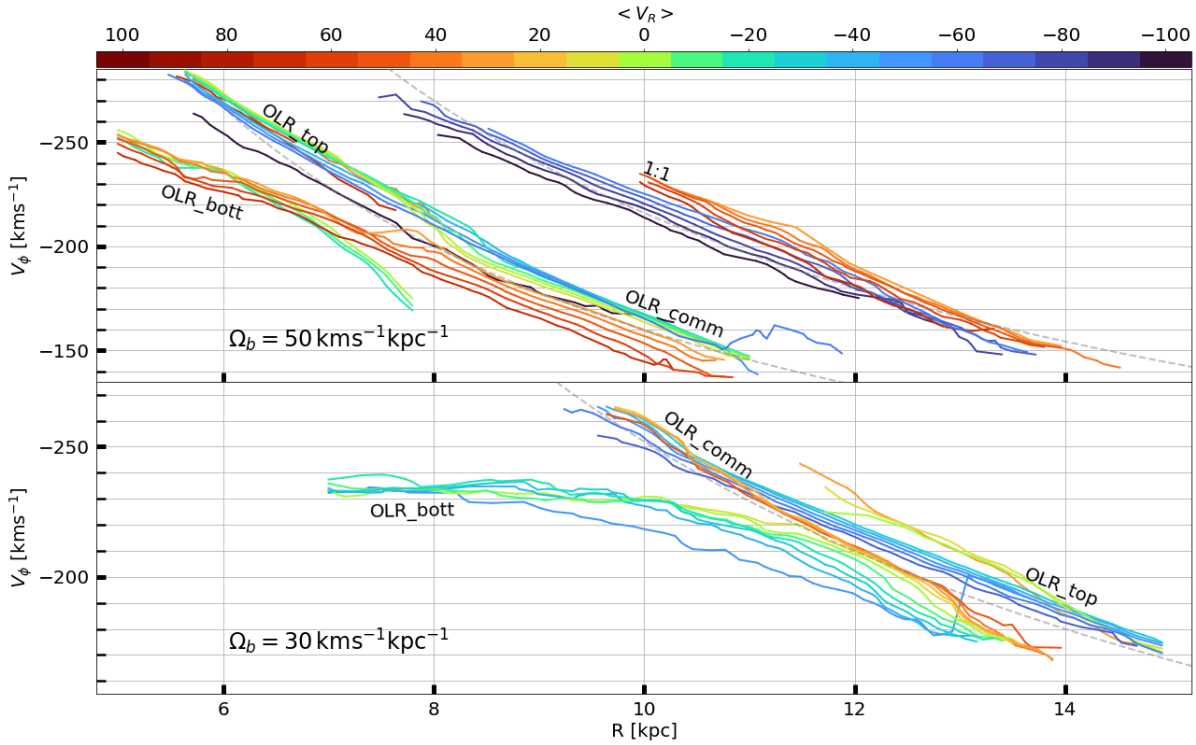

FIGURE 6.4: Azimuthal velocity of the kinematic substructures in the radial direction $(\phi = 0, Z = 0\ kpc)$ for the test particle simulations, as a function of the radius, and coloured by their radial velocity. We include dashed grey lines corresponding to constant angular momentum lines as a guide. Top: Structures for the fast bar model. Bottom: Structures for the slow bar model. In the fast bar model, we are able to detect substructures related to the OLR and the $1:1$ resonance, in the slow bar we only detect structures related with the OLR. With our methodology, we are able to show the complex morphology of the arches in a single image.

- The azimuthal velocity of the *Horn*, *Sirius* and *Arch/Hat* moving groups presents an axisymmetrical behaviour. In both our simulations, we observed a small azimuthal gradient in V_ϕ in the Arch/Hat-like structures, although it approches 0 as R increases. This could be related to the young bar model we are using.

- The vertical curvature of the moving groups is similar at the same R. These curvatures are dominated by the gravitational potential to first order, independently of the observed resonance. However, we notice that the *Coma Berenices* group deviates from this behaviour, which points to a different dynamical origin that deserves further investigation.

- In the fast bar simulation, a correlation between $\partial V_\phi / \partial \phi$ and V_R is observed for the OLR trapping region. The region where this correlation is observed in the simulation ($R > 9\,\mathrm{kpc}$, $V_\phi < -170$) is poorly sampled in Gaia EDR3, but this could potentially be used to give information on the pattern speed of the bar with better data.

Spiral arms, resonances with the bar, accretion events, and possibly other effects can contribute to the present phase space distribution from which we obtain our observables. Disentangling all the contributions of these dynamical processes is hard to address. We have shown the complexity of the phase-space structure that even a single mechanism (namely the bar) can produce. Our methodology allows to extract a quantitative and robust measurement of the observed phase space substructure that can be then compared and/or fit to different models. A similar methodology has been developed in parallel by Lucchini et al., 2022.

Chapter 7

Bar-disc perturbations in backward integration simulation for comparisons with Gaia DR3

As the axisymmetric potential of the Galaxy is perturbed by both a bar and a spiral and the method already described previously is not suitable for dealing with areas where the resonances overlap, the method of backward orbit integrations is used. First, a more appropriate background potential is chosen to describe the Milky Way. The potential used is that obtained by a fitting process applied to the circular velocity curve to match the potential used by Portail et al., 2016.

The basic idea of backwards orbit integrations is to make use of the collisionless Boltzmann equation to calculate the value of the distribution function along an orbit. As such, one can integrate backwards along an orbit to a time where there is no perturbation. Then, one can find the value of the perturbed distribution function at the present time for a certain point to simply equal the value of the unperturbed distribution function for the point reached after performing the integration. One can then directly calculate mean or median velocity maps which are compared to the ones obtained by the Gaia mission.

The bar which is the same one used by Portail et al., 2016 is taken in our case as the perturber and the variables are the amplitudes of the different modes of the bar as well as the pattern speed of the bar.

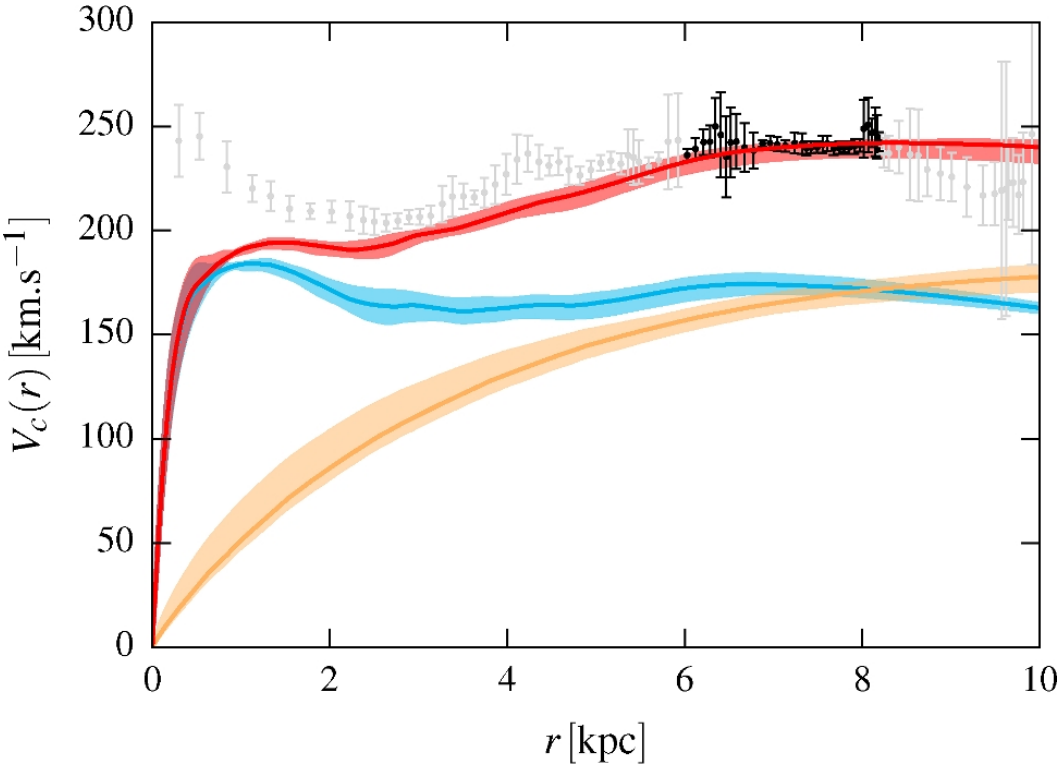

FIGURE 7.1: Rotation curve of the best model and range of model variations for evaluation of systematics on top of the composite rotation curve measurements from Sofue, Honma, and Omodaka, 2009. Blue, yellow and red curves represent respectively the baryonic, dark matter and total rotation curve, assuming that the totality of the additional central mass is baryonic.

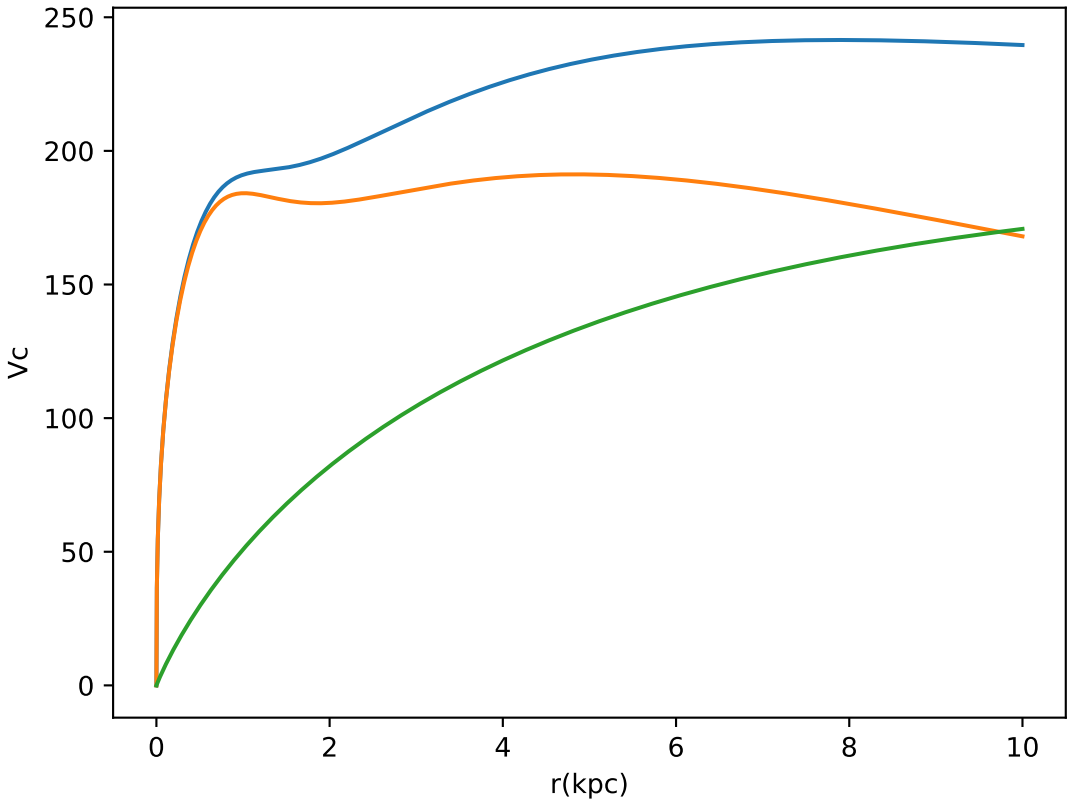

FIGURE 7.2: Rotation curve of our fitted model. Yellow, green and blue curves represent respectively the baryonic, dark matter and total rotation curve.

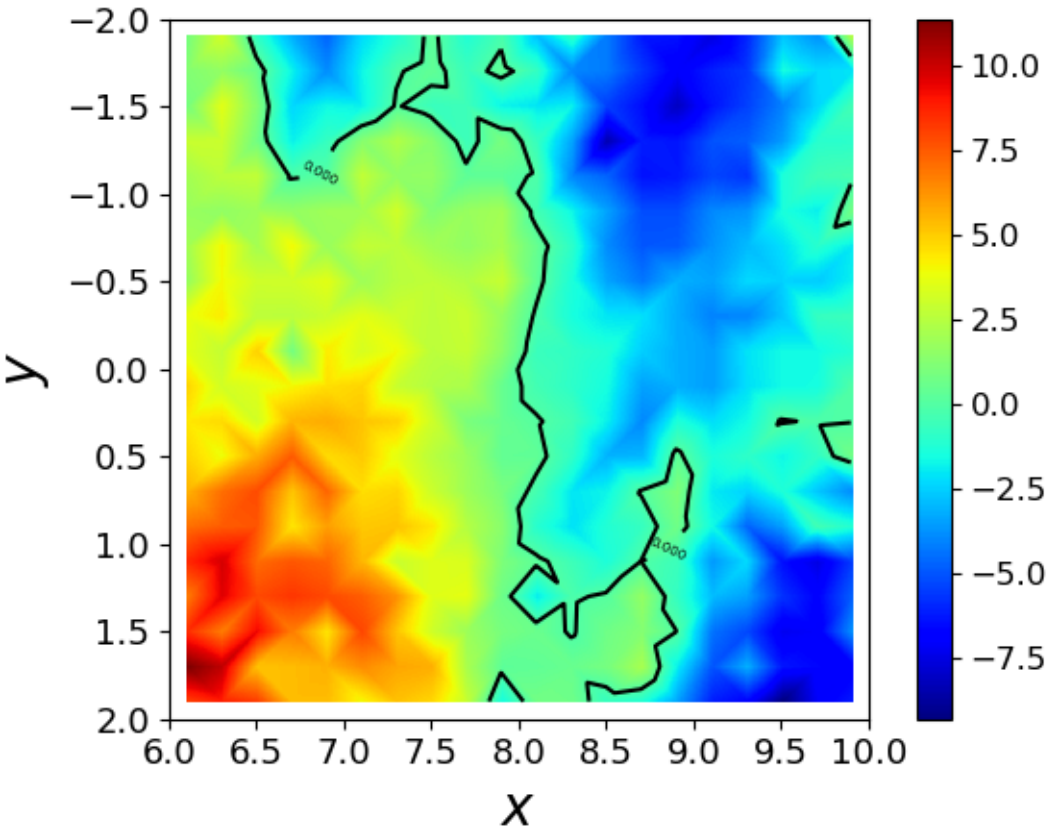

FIGURE 7.3: Median radial velocity map generated from the Gaia data. The iso-velocity contours $V_R = 0\, kms^{-1}$ are pointed out as black lines.

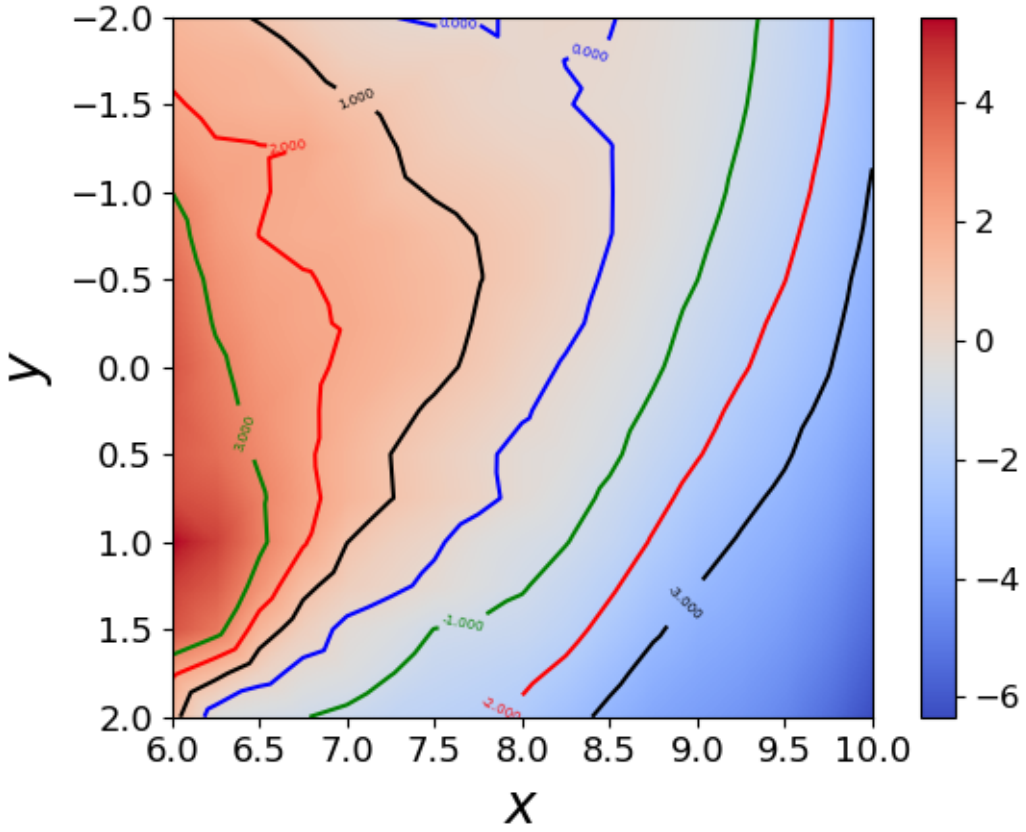

FIGURE 7.4: Median radial velocity map generated from our simulation with contours of constant radial velocity.

Chapter 8

Published articles

Astronomy & Astrophysics manuscript no. output
July 20, 2022

Perturbed distribution functions with accurate action estimates for the Galactic disc

H. Al Kazwini[1], Q. Agobert[1], A. Siebert[1], B. Famaey[1], G. Monari[1], S. Rozier[1], P. Ramos[1], R. Ibata[1], S. Gausland[2], C. Rivière[2], and D. Spolyar[3]

[1] Université de Strasbourg, CNRS UMR 7550, Observatoire astronomique de Strasbourg, 11 rue de l'Université, 67000 Strasbourg, France
[2] Université de Strasbourg, UFR de Mathématique et d'Informatique, 7 rue René Descartes, 67084 Strasbourg, France
[3] The Oskar Klein Centre for Cosmoparticle Physics, Department of Physics, Stockholm University, AlbaNova, 10691 Stockholm, Sweden

Received; accepted

ABSTRACT

In the Gaia era, understanding the effects of the perturbations of the Galactic disc is of major importance in the context of dynamical modelling. In this theoretical paper we extend previous work in which, making use of the epicyclic approximation, the linearized Boltzmann equation had been used to explicitly compute, away from resonances, the perturbed distribution function of a Galactic thin-disc population in the presence of a non-axisymmetric perturbation of constant amplitude. Here we improve this theoretical framework in two distinct ways in the new code that we present. First, we use better estimates for the action-angle variables away from quasi-circular orbits, computed from the `AGAMA` software, and we present an efficient routine to numerically re-express any perturbing potential in these coordinates with a typical accuracy at the per cent level. The use of more accurate action estimates allows us to identify resonances such as the outer 1:1 bar resonance at higher azimuthal velocities than the outer Lindblad resonance (OLR), and to extend our previous theoretical results well above the Galactic plane, where we explicitly show how they differ from the epicyclic approximation. In particular, the displacement of resonances in velocity space as a function of height can in principle constrain the 3D structure of the Galactic potential. Second, we allow the perturbation to be time dependent, thereby allowing us to model the effect of transient spiral arms or a growing bar. The theoretical framework and tools presented here will be useful for a thorough analytical dynamical modelling of the complex velocity distribution of disc stars as measured by past and upcoming Gaia data releases.

Key words. Galaxy: kinematics and dynamics – Galaxy: disc – Galaxy: solar neighborhood – Galaxy: structure – Galaxy: evolution – galaxies: spiral

1. Introduction

The natural canonical coordinate system of phase-space for Galactic dynamics and perturbation theory is the system of action-angle variables (Binney & Tremaine 2008). In an axisymmetric system in equilibrium, the Jeans theorem implies that the phase-space distribution function (DF) of any stellar (or dark matter) component can be expressed solely as a function of the actions that are labelling the actual orbits (e.g. Binney & Piffl 2015; Cole & Binney 2017). However, the effect of various perturbers of the potential (e.g. the Galactic bar and spiral arms) must be included in this process, together with the response of the distribution function. Within the resonant regions, to fully capture the behaviour of the DF, one needs to construct for each perturber new orbital tori, complete with a new system of action-angle variables (e.g. Monari et al. 2017a; Binney 2020a,b). Away from resonances, however, one can simply use the linearized Boltzmann equation. This also allows us to accurately identify the location of resonances.

This is particularly important in the context of the interpretation of recent data from the Gaia mission (Gaia Collaboration et al. 2018a, 2021), which revealed in exquisite detail the fine structure of stellar action space (e.g. Trick et al. 2019; Monari et al. 2019b,a). While the existence of moving groups of dynamical origin had been known for a long time in local velocity space around the Sun (e.g. Dehnen 1998; Famaey et al. 2005), Gaia revealed their structure in exquisite detail (Ramos et al. 2018) and also provided an estimate of their age distribution (Laporte et al. 2020), together with the shape of the global velocity field away from the Sun within the Galactic disc (Gaia Collaboration et al. 2018b). One additional major finding of Gaia is the existence of a local phase-spiral in vertical height versus vertical velocity in the solar neighbourhood (Antoja et al. 2018), which might be related to a vertical perturbation of the disc, for example by the Sagittarius dwarf galaxy (e.g. Laporte et al. 2019; Binney & Schönrich 2018; Bland-Hawthorn & Tepper-García 2021).

In previous theoretical work, Monari et al. (2016) (hereafter M16) explicitly computed the response of an axisymmetric DF in action space, representing a Milky Way thin-disc stellar population, to a quasi-stationary three-dimensional spiral potential, using the epicyclic approximation to model the actions, which is only a valid approximation for quasi-circular orbits in the thin disc. It was notably shown that the first-order moments of the perturbed DF then give rise to non-zero radial and vertical bulk flows (breathing modes). However, to treat perturbations away from the mid-plane, which is particularly important in the Gaia

context, one cannot make use of the epicyclic approximation to compute action-angle variables. Moreover, it is well known that spiral modes in simulations can be transient, remaining stationary for only a few rotations (Sellwood & Carlberg 2014), and the response of the disc should be different during the period of rising or declining amplitude. The same can be true for the bar, whose amplitude and pattern speed can also grow or vary with time (e.g. Chiba et al. 2021; Hilmi et al. 2020).

Here we improve on this previous modelling of M16 in two ways. First, we use a better estimate than the epicyclic approximation for the action-angle variables, relying on the torus mapping method of McGill & Binney (1990) to convert from actions and angles to positions and velocities, and on the Stäckel fudge (Binney 2012; Sanders & Binney 2016) for the reverse transformation. This will allow us to extend previous results to eccentric orbits and orbits wandering well above the Galactic plane. The routines developed and presented in this paper will also be of fundamental importance to study the vertical perturbations of the Galactic disc in further works. Second, we let the perturbation evolve with time, thereby allowing us to model the effect of a growing bar.

The paper is organized as follows. In Sect. 2, after a short reminder of the theoretical framework of perturbed DF, already given in detail in M16, we present the method used to expand in Fourier series the perturbing potential within the new action-angle coordinate system. Then a comparison with the results in the epicyclic case is made in Sect. 3. In Sect. 4 we explore the temporal treatment of the DF for an analytic growth of the amplitude of the perturber. Finally, we conclude and discuss the possible future applications of these theoretical tools in Sect. 5. The Appendix is dedicated to the presentation of the code.

2. Perturbing potential and perturbed DF

2.1. Action-angle variables

The canonical phase-space action-angle variables ($\boldsymbol{J}$,$\boldsymbol{\theta}$) of an integrable system are obtained from a canonical transformation implicitly using Hamilton's characteristic function as a type 2 generating function. The actions $\boldsymbol{J}$ are defined as new generalized momenta corresponding to a closed path integral of the velocities along their corresponding canonically conjugate position variable, namely $J_i = \oint v_i \mathrm{d}x_i/(2\pi)$. Since this does not depend on time, these actions are integrals of motion, and the Hamiltonian can be expressed purely as a function of these actions.

It turns out that Galactic potentials are close enough to integrable systems that actions can be estimated for them. For quasi-circular orbits close to the Galactic plane, with separable motion in the vertical and horizontal directions, one can locally approximate the radial and vertical motions of an orbit with harmonic motions, which is known as the epicyclic approximation. The radial and vertical actions then simply correspond to the radial and vertical energies divided by their respective (radial and vertical) epicyclic frequency. However, the epicyclic approximation is no longer valid when considering orbits with higher eccentricity, or with a large vertical amplitude. More precise ways of determining the action and angle coordinates have been devised. They typically differ depending on whether one wishes to transform angles and actions to positions and velocities or instead to make the reverse transformation from positions and velocities to actions and angles. In the first case a very efficient method is the torus mapping method first introduced by McGill & Binney (1990) (see also Binney & McMillan 2016 for a recent overview), while in the second case a Stäckel fudge is generally used (Binney 2012; Sanders & Binney 2016).

The general idea of torus mapping is to first express the Hamiltonian in the action-angle coordinates ($\boldsymbol{J}_T, \boldsymbol{\theta}_T$) of a toy potential, for which the transformation to positions and velocities is fully known analytically. The algorithm then searches for a type 2 generating function $G(\boldsymbol{\theta}_T, \boldsymbol{J})$ expressed as a Fourier series expansion on the toy angles $\boldsymbol{\theta}_T$, for which the Fourier coefficients are such that the Hamiltonian remains constant at constant $\boldsymbol{J}$. This generating function fully defines the canonical transformation from actions and angles to positions and velocities. For the inverse transformation, an estimate based on separable potentials can be used. These potentials are known as Stäckel potentials (e.g. Famaey & Dejonghe 2003), for which each generalized momentum depends on its conjugated position through three isolating integrals of the motion. These potentials are expressed in spheroidal coordinates defined by a focal distance. For a Stäckel potential, this focal distance of the coordinate system is related to the first and second derivatives of the potential. One can thus use the true potential at any configuration space point to compute the equivalent focal distance as if the potential were of Stäckel form, and from there compute the corresponding isolating integrals of the motion and the actions. In the following we make use of both types of transformations, namely the torus mapping to express the potential in action-angle coordinates and the Stäckel fudge to represent distribution functions in velocity space at a given configuration space point.

We now let $H_0(\boldsymbol{J})$ be the Hamiltonian of the axisymmetric and time-independent zeroth order gravitational potential Φ_0 of the Galaxy. The equations of motion connecting actions $\boldsymbol{J}$ and the canonically conjugate angles $\boldsymbol{\theta}$ are then simply

$$\dot{\boldsymbol{\theta}} = \frac{\partial H_0}{\partial \boldsymbol{J}} = \boldsymbol{\omega}(\boldsymbol{J}), \quad \dot{\boldsymbol{J}} = -\frac{\partial H_0}{\partial \boldsymbol{\theta}} = 0, \tag{1}$$

with $\boldsymbol{\omega}$ being the fundamental orbital frequencies. Thus, for a given orbit, the actions $\boldsymbol{J}$ are constant in time, defining an orbital torus on which the angles $\boldsymbol{\theta}$ evolve linearly with time, according to $\boldsymbol{\theta}(t) = \boldsymbol{\theta}_0 + \boldsymbol{\omega} t$. The Jeans theorem then tells us that the phase-space distribution function (DF) of an axisymmetric potential $f = f_0(\boldsymbol{J})$ is in equilibrium. In other words, f_0 is a solution of the collisionless Boltzmann equation:

$$\frac{\mathrm{d}f}{\mathrm{d}t} = 0. \tag{2}$$

2.2. Perturbed distribution functions

We now let Φ_1 be the potential of a small perturbation to the axisymmetric background potential Φ_0 of the Galaxy, with an amplitude relative to this axisymmetric background $\epsilon \ll 1$. Then the total potential is $\Phi = \Phi_0 + \Phi_1$ and the DF becomes, to first order in ϵ, $f = f_0 + f_1$, which is still a solution of the collisionless Boltzmann equation. Inserting $f = f_0 + f_1$ in Eq. (2), and keeping only the terms of order ϵ, leads to the *linearized* collisionless Boltzmann equation

$$\frac{\mathrm{d}f_1}{\mathrm{d}t} + [f_0, \Phi_1] = 0, \tag{3}$$

where [,] is the Poisson bracket. Integrating Eq. (3) over time, from $-\infty$ to the time t, leads to

$$f_1(\boldsymbol{J}, \boldsymbol{\theta}, t) = \int_{-\infty}^{t} \mathrm{d}t' \frac{\partial f_0}{\partial \boldsymbol{J}'}(\boldsymbol{J}') \cdot \frac{\partial \Phi_1}{\partial \boldsymbol{\theta}'}(\boldsymbol{J}', \boldsymbol{\theta}', t'), \tag{4}$$

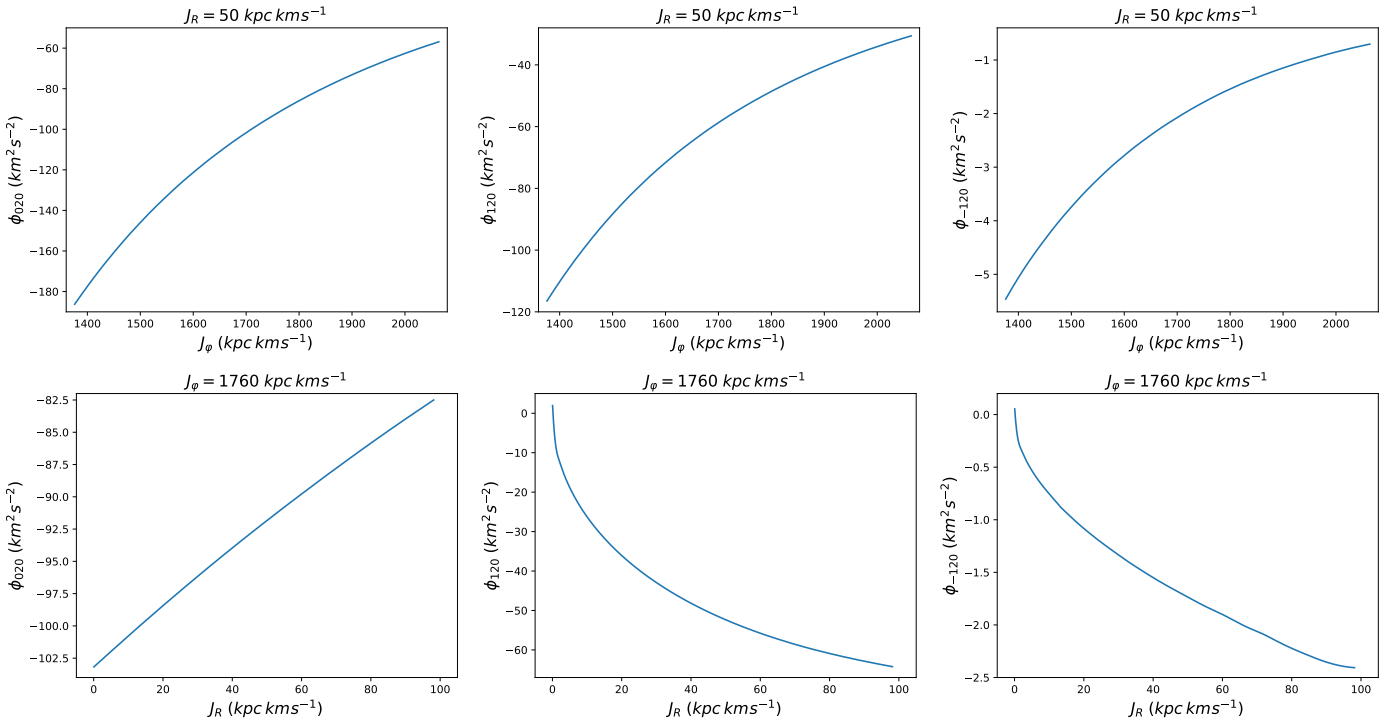

Fig. 1. Variations in a few Fourier coefficients $\phi_{jml}(\boldsymbol{J})$ of the bar potential from Sect. 2.4 as J_R or J_φ increase separately at $J_z = 0$. The actions on the abscissa axis are in kpc km s^{-1}. The curves are very smooth, which justifies our use of the cubic splines method to interpolate.

where $\boldsymbol{J}'$ and $\boldsymbol{\theta}'$ correspond to the actions and angles in the unperturbed case as a function of time (i.e. constant actions $\boldsymbol{J}'$ and angles evolving linearly). Since any function of the angles is 2π-periodic in the angles, the perturbing potential Φ_1 can be expanded in a Fourier series as

$$\Phi_1(\boldsymbol{J},\boldsymbol{\theta},t) = \mathrm{Re}\left\{\sum_{\boldsymbol{n}} \phi_{\boldsymbol{n}}(\boldsymbol{J},t)\,\mathrm{e}^{\mathrm{i}\boldsymbol{n}\cdot\boldsymbol{\theta}}\right\}. \tag{5}$$

Hereafter we consider in-plane perturbations such as spiral arms, meaning that we can write the time-varying Fourier coefficients in a non-rotating frame as $\phi_{\boldsymbol{n}}(\boldsymbol{J},t) = g(t)\,h(t)\,\phi_{\boldsymbol{n}}(\boldsymbol{J})$, where $g(t)$ controls the amplitude of the perturbation and $h(t)$ controls its pattern speed, with $h(t) = \mathrm{e}^{-\mathrm{i}m\Omega_\mathrm{p}t}$, where Ω_p is the pattern speed of the perturbation and m its azimuthal wave number (i.e. its multiplicity). Hereafter we mainly consider $m = 2$ perturbations. The vector index $\boldsymbol{n}$ is a triplet of scalar integer indices (j,k,l) running in principle from $-\infty$ to ∞, but in practice limited to a given range sufficient to approximate the perturbing potential. In the case of an m-fold in-plane perturbation, it is sufficient to take $k = m$. The main goal of this section is to express typical non-axisymmetric perturbing potentials originally expressed in configuration space as such a Fourier series in action-angle space. The algorithm that we present in Sect. 2.3 can be applied to any perturbing potential, however, including non-plane symmetric vertical perturbations. Once the potential is expressed as a function of angles and actions as in Eq. (5), then Eq. (4) becomes

$$f_1(\boldsymbol{J},\boldsymbol{\theta},t) = \mathrm{Re}\left\{\mathrm{i}\frac{\partial f_0}{\partial \boldsymbol{J}}(\boldsymbol{J})\cdot\sum_{\boldsymbol{n}}\boldsymbol{n}\int_{-\infty}^{t}\mathrm{d}t'\phi_{\boldsymbol{n}}(\boldsymbol{J}',t')\,\mathrm{e}^{\mathrm{i}\boldsymbol{n}\cdot\boldsymbol{\theta}'(t')}\right\}. \tag{6}$$

In M16, assuming $\phi_{\boldsymbol{n}}(\boldsymbol{J}',t') = g(t')\,h(t')\,\phi_{\boldsymbol{n}}(\boldsymbol{J})$, with $h(t') = \mathrm{e}^{-\mathrm{i}m\Omega_\mathrm{p}t'}$, and the amplitude of the perturbing potential constant in time at present time ($g(t) = 1$), and zero and constant in time at $-\infty$, led to the following explicit solution for $f_1(\boldsymbol{J},\boldsymbol{\theta},t)$,

$$f_1(\boldsymbol{J},\boldsymbol{\theta},t) = \mathrm{Re}\left\{\frac{\partial f_0}{\partial \boldsymbol{J}}(\boldsymbol{J})\cdot\sum_{\boldsymbol{n}}\boldsymbol{n}\phi_{\boldsymbol{n}}(\boldsymbol{J})\frac{\mathrm{e}^{\mathrm{i}\theta_{\mathrm{s},\boldsymbol{n}}}}{\omega_{\mathrm{s},\boldsymbol{n}}}\right\}, \tag{7}$$

where we defined

$$\theta_{\mathrm{s},\boldsymbol{n}} = \boldsymbol{n}\cdot\boldsymbol{\theta} - m\Omega_\mathrm{p}t, \tag{8}$$

$$\omega_{\mathrm{s},\boldsymbol{n}} = \boldsymbol{n}\cdot\boldsymbol{\omega} - m\Omega_\mathrm{p}. \tag{9}$$

The subscript 's' stands for slow, because in the proximity of a resonance of the type $\omega_{\mathrm{s},\boldsymbol{n}} = 0$, the angle $\theta_{\mathrm{s},\boldsymbol{n}}$ evolves very slowly. One can also immediately see that the linearized solution above is valid only away from such resonances since it diverges for these orbits. Orbits near these resonances are actually trapped, and for them the determination of the linearly perturbed DF becomes inappropriate. Specific treatment for these resonant regions is required, which was addressed in Monari et al. (2017a) within the epicyclic approximation, and by Binney (2020a) in a more general context.

Using the epicyclic approximation the Fourier coefficients of a spiral potential have been computed analytically in M16 with indices $\boldsymbol{n} = (j,k,l)$ running over the values $j = \{-1,0,1\}$, $k = m = 2$, and $l = \{-2,0,2\}$, and the perturbed distribution function away from resonances was then computed. In the following we extend the results of M16 to a more general estimate of the action-angle variables through the torus mapping method. The resulting DF is plotted in velocity space by making use of the Stäckel fudge. For both transformations we use the Action-based Galaxy Modelling Architecture (`AGAMA`; Vasiliev 2019, 2018).

2.3. Perturbing potential in actions and angles

In previous work, M16 worked in the epicyclic approximation as it provides an analytical expression for evaluating actions and

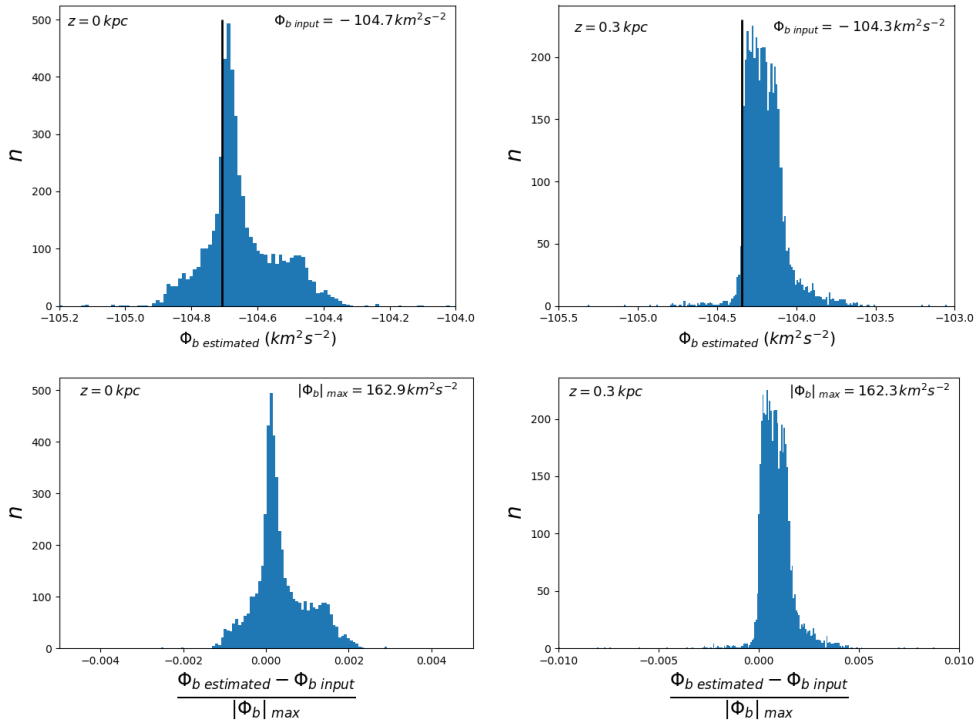

Fig. 2. Accuracy of the reconstruction of the bar potential . Left panel (top): Estimate of the bar potential from Sect. 2.4 at the Sun's position in the plane with 41 complex Fourier coefficients in Eq. 10 and the reconstruction using cubic splines. The vertical line denotes the true value. The value in the top right inset denotes the true value in physical units. The potential is always estimated at the same configuration space location (within the plane, at the Sun's position) but for different velocities. Left panel (bottom): Relative accuracy compared to the maximum value of the bar potential at the Sun's radius denoted in the top right inset. Right panel: Same, but at $z = 0.3$ kpc with 231 complex Fourier coefficients. The typical accuracy is well below the per cent level, although with a slight bias towards lower amplitudes (i.e. $|\Phi_{\mathrm{b\,estimated}}| < |\Phi_{\mathrm{b\,input}}|$) above the plane.

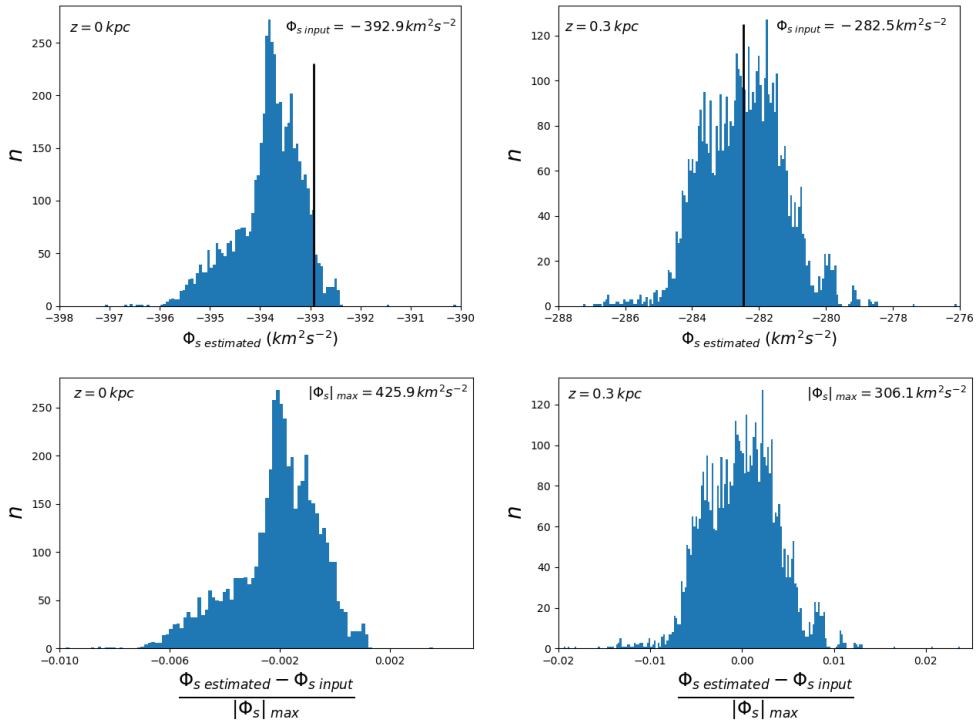

Fig. 3. Accuracy of the reconstruction of the spiral arms potential. Left panel (top): Estimate of the spiral arms potential from Sect. 2.5 at the Sun's position in the plane with 41 complex Fourier coefficients in Eq. 10 and the reconstruction using cubic splines. The vertical line denotes the true value. The value in the top right inset denotes the true value in physical units. The potential is always estimated at the same configuration space location (within the plane, at the Sun's position) but for different velocities. Left panel (bottom): Relative accuracy compared to the maximum value of the spiral arms potential at the Sun's radius denoted in the top right inset. Right panel: Same, but at $z = 0.3$ kpc with 231 complex Fourier coefficients. The typical accuracy is again well below the per cent level in the plane, while it is around the per cent level above the plane.

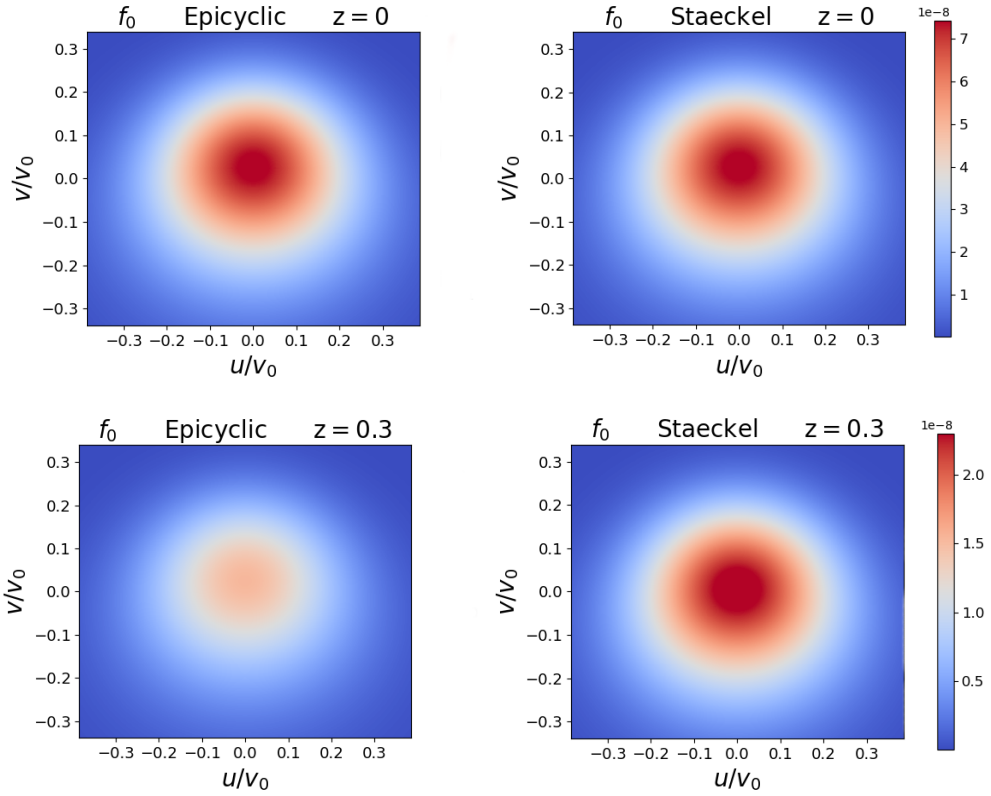

Fig. 4. Local uv-plane stellar velocity distribution at axisymmetric equilibrium and for $w = 0$, from Eq. 16 at $(R, z, \varphi) = (R_0, 0, 0)$. Left panel: Epicyclic approximation in the plane (top) and at $z = 0.3$ kpc (bottom). Right panel: Stäckel fudge with `AGAMA` in the plane (top) and at $z = 0.3$ kpc (bottom).

angles from cylindrical coordinates. The Fourier coefficients of the Fourier series expansion of the perturbing potentials were then also determined analytically within this approximation. Approximating the vertical component of the perturbing potential by a harmonic oscillator, the nine Fourier coefficients ϕ_{jml} were then limited to the range $j = \{-1, 0, 1\}$, corresponding to the θ_R oscillations of the potential, and $l = \{-2, 0, 2\}$, corresponding to the θ_z oscillations of the potential close to the Galactic plane.

However, the epicyclic approximation is only valid for nearly circular orbits, but not when considering eccentric orbits. Hereafter the transformations from angles and actions to positions and velocities (and reciprocally) are instead evaluated numerically with `AGAMA` (Vasiliev 2018). The code makes use of torus mapping to go from action-angle to position-velocity, and uses the Stäckel fudge for the inverse transformation. Our goal now is to obtain the Fourier coefficients of a known perturbing potential using these numerically computed actions (instead of epicyclic).

We proceed in the following way to evaluate Fourier coefficients of the perturbing potential in Eq. (5). The first step is to choose a set of actions within a range representing all the orbits of interest in the axisymmetric background configuration, each triplet of actions representing one of the orbits. For instance, in the solar neighbourhood we consider radial actions ranging from 0 to 220 kpc km s^{-1}, azimuthal actions ranging from 1200 to 2160 kpc km s^{-1}, and vertical actions ranging from 0 to 26 kpc km s^{-1} depending on the height above the Galactic plane. For each orbit, we then define an array of angles $(\theta_R, \theta_\varphi, \theta_z)$. These actions and angles can then all be converted to positions thanks to the torus machinery in `AGAMA`. For each triplet of actions, a range of positions (R, φ, z) is covered by the angles, and we look for the best-fitting coefficients $\phi_{jml}(J_R, J_z, J_\varphi)$, satisfying the following equation (setting $t = 0$ for the time being):

$$\Phi_1(R, \varphi, z) = \mathrm{Re}\left\{\sum_{j,l} \phi_{jml}(J_R, J_z, J_\varphi) \mathrm{e}^{\mathrm{i}(j\theta_R + m\theta_\varphi + l\theta_z)}\right\}. \quad (10)$$

This is performed with the method of linear least squares using singular value decomposition, as proposed in chapter 15.4 of Press et al. (1992). We then interpolate the value of the coefficient ϕ_{jml} with cubic splines, also proposed in Press et al. (1992), chapter 3.3. The number of Fourier coefficients is chosen to be high enough to ensure that all orbits passing through a given configuration space point yield the same value of the potential at this point within a relative accuracy of less than 1%.

Concretely, we apply this hereafter to the potential of a central bar and of a two-armed spiral pattern. The background axisymmetric potential is chosen to be Model I from Binney & Tremaine (2008). This potential has a bulge described by a truncated oblate spheroidal power law; a gaseous disc with a hole at the centre; a stellar thin disc and a stellar thick disc, both with a scale-length of 2 kpc; and a dark halo with an oblate two-power-law profile. The galactocentric radius of the Sun is set at $R_0 = 8$ kpc, and the local circular velocity is $v_0 = 220$ km s^{-1}.

2.4. Bar potential

The potential we choose for the bar is a simple quadrupole potential (Weinberg 1994; Dehnen 2000) with

$$\Phi_{1,\mathrm{b}}(R, z, \varphi, t) = \mathrm{Re}\left\{\Phi_{\mathrm{a,b}}(R, z)\mathrm{e}^{\mathrm{i}m(\varphi - \varphi_\mathrm{b} - \Omega_\mathrm{b} t)}\right\}, \quad (11)$$

where $m = 2$, Ω_b is the pattern speed of the bar (expressed hereafter in multiples of the angular frequency at the Sun $\Omega_0 =$

v_0/R_0, where v_0 is the local circular velocity at the galactocentric radius of the Sun R_0), and the azimuth is defined with respect to a line corresponding to the Galactic centre-Sun direction in the Milky Way, φ_b thus being the angle between the Sun and the long axis of the bar. We also choose

$$\Phi_{a,b}(R,z) = -\alpha_b \frac{v_0^2}{3}\left(\frac{R_0}{R_b}\right)^3\left(\frac{R}{r}\right)^2 \begin{cases} \left(\frac{r}{R_b}\right)^{-3} & R \geq R_b, \\ 2-\left(\frac{r}{R_b}\right)^3 & R < R_b, \end{cases} \quad (12)$$

where $r^2 = R^2 + z^2$ is the spherical radius, R_b is the length of the bar, and α_b represents the maximum ratio between the bar and axisymmetric background radial forces at the Sun's galactocentric radius $R = R_0$. We use hereafter, as a representative example, $R_b = 0.625\,R_0$, $\varphi_b = 25^o$, and $\alpha_b = 0.01$. We also consider two typical pattern speeds: $\Omega_b = 1.89\,\Omega_0$ and $\Omega_b = 1.16\,\Omega_0$.

The bar potential is quite easy to reproduce using Fourier coefficients since it varies smoothly on orbits. Thus, for a study in the Galactic plane, 41 complex Fourier coefficients for each triplet of actions are sufficient to approximate the value of the potential with an accuracy much better than 1%. Here it should be noted that the potential of the bar oscillates along the azimuth at a given radius and that the relative accuracy can be ill-defined when the potential passes through zero. Therefore, we define here the relative accuracy with respect to the amplitude (i.e. the maximum value) of the bar potential at a given radius. The Fourier coefficients themselves vary smoothly, as illustrated in Fig. 1, which shows the variations of a few Fourier coefficients as J_R and J_φ increase separately, justifying the use of cubic-spline interpolation to get the value of the potential at a specific position. Figure 2 demonstrates the accuracy of our method in reproducing the bar potential in the solar neighbourhood for different values of the local velocities. The potential is estimated at the same configuration space location for the whole range of relevant velocities, with a typical accuracy at the per cent level both in the plane and at $z = 0.3$ kpc. The accuracy remains very good above the plane, although with a slight bias towards lower amplitudes than the true value. More complex Fourier coefficients are needed outside of the plane. This tool is of course not limited to any specific form of the perturbing potential, the only adjustable parameter being the number of Fourier coefficients necessary to recover a given perturbing potential with a per cent-level accuracy.

2.5. Spiral potential

The potential we use for the spiral arms is the following (Cox & Gómez 2002; Monari et al. 2016)

$$\Phi_{1,sp}(R,z,\varphi,t) = \mathrm{Re}\left\{\Phi_{a,sp}(R,z)\,\mathrm{e}^{\mathrm{i}m(\varphi-\varphi_{sp}-\Omega_{sp}t)}\right\}, \quad (13)$$

where $m = 2$, Ω_{sp} is the pattern speed of the spiral arms, and

$$\Phi_{a,sp}(R,z) = -\frac{A}{R_{sp}KD}\mathrm{e}^{\mathrm{i}m\frac{\ln(R/R_{sp})}{\tan(p)}}\left[\mathrm{sech}\left(\frac{Kz}{\beta}\right)\right]^\beta, \quad (14)$$

where

$$K(R) = \frac{2}{R\sin(p)}, \quad \beta(R) = K(R)h_{sp}[1+0.4K(R)h_{sp}],$$
$$D(R) = \frac{1+K(R)h_{sp}+0.3[K(R)h_{sp}]^2}{1+0.3K(R)h_{sp}}. \quad (15)$$

Here $R_{sp} = 1$ kpc is the length parameter of the logarithmic spiral potential, $h_{sp} = 0.1$ kpc the height parameter, $p = -9.9^o$ the pitch angle, $\varphi_{sp} = -26^o$ the phase, and $A = 683.4\,\mathrm{km^2\,s^{-2}}$ the amplitude. Hereafter, we adopt a pattern speed $\Omega_{sp} = 0.84\,\Omega_0$, placing the main resonances away from (or at high azimuthal velocities in) the solar neighbourhood.

Within the Galactic plane, the top panel of Fig. 3 shows our reconstruction of the spiral potential at the Sun's position, again with 41 complex Fourier coefficients. The accuracy is again below the per cent level as in the bar case, although in the spiral case there is a slight bias towards higher amplitudes with respect to the input spiral potential. This bias is very small, however, and does not affect our results. At $z = 0.3$ kpc, more complex Fourier coefficients are again needed (Fig. 3, bottom panel), and the accuracy reaches the per cent level, this time without bias.

3. Results and comparison with the epicyclic approximation

3.1. Background equilibrium

From here on we work with a background axisymmetric DF f_0 as a sum of two quasi-isothermal DFs (Binney & McMillan 2011) for the thin and thick disc:

$$f_0(J_R,J_z,J_\varphi) = f_{thin} + 0.075 f_{thick}. \quad (16)$$

The form of each DF is

$$f(J_R,J_z,J_\varphi) = \frac{\Omega\exp(-R_g/h_R)}{2\,(2\pi)^{3/2}\,\kappa\,\tilde\sigma_R^2\,\tilde\sigma_z\,z_0}\exp\left(-\frac{J_R\kappa}{\tilde\sigma_R^2}-\frac{J_z\nu}{\tilde\sigma_z^2}\right), \quad (17)$$

where R_g, Ω, κ, and ν are all functions of J_φ, and

$$\tilde\sigma_R(R_g) = \tilde\sigma_R(R_0)\exp\left(-\frac{R_g-R_0}{h_{\sigma_R}}\right),$$
$$\tilde\sigma_z(R_g) = \tilde\sigma_z(R_0)\exp\left(-\frac{R_g-R_0}{h_{\sigma_z}}\right). \quad (18)$$

For the thin disc DF f_{thin}, we choose $h_R = 2$ kpc, $z_0 = 0.3$ kpc, $h_{\sigma_R} = h_{\sigma_z} = 10$ kpc, $\tilde\sigma_R(R_0) = 35$ km s^{-1}, and $\tilde\sigma_z(R_0) = 15$ km s^{-1}. For the thick disc DF f_{thick}, we choose $h_R = 2$ kpc, $z_0 = 1$ kpc, $h_{\sigma_R} = 10$ kpc, $h_{\sigma_z} = 5$ kpc, $\tilde\sigma_R(R_0) = 50$ km s^{-1}, and $\tilde\sigma_z(R_0) = 50$ km s^{-1}. Since we normalize the central surface densities of the thin and thick disc to 1, our densities can be multiplied by the appropriate surface density of the relevant stellar population to obtain physical units. The background axisymmetric potential is chosen to be Model I from Binney & Tremaine (2008), in which the above equilibrium DF f_0 is a good representation of the thin and thick disc components. In this model one has $R_0 = 8$ kpc and $v_0 = 220$ km s^{-1}.

The top panels of Fig. 4 display the (u,v)-plane in the solar neighbourhood within the $z = 0$ plane (and for $w = -v_z = 0$) for this f_0 axisymmetric background, where $u = -v_R$ and $v = v_\varphi - v_0$, obtained by converting velocity-space into action-space through the epicyclic approximation and the Stäckel fudge from `AGAMA`. The velocity distributions are quite similar. However, as can be seen in the bottom panels of Fig. 4, the epicyclic approximation quickly becomes imprecise outside of the plane as it implies a sharper falloff of the density compared to the better Stäckel action estimates.

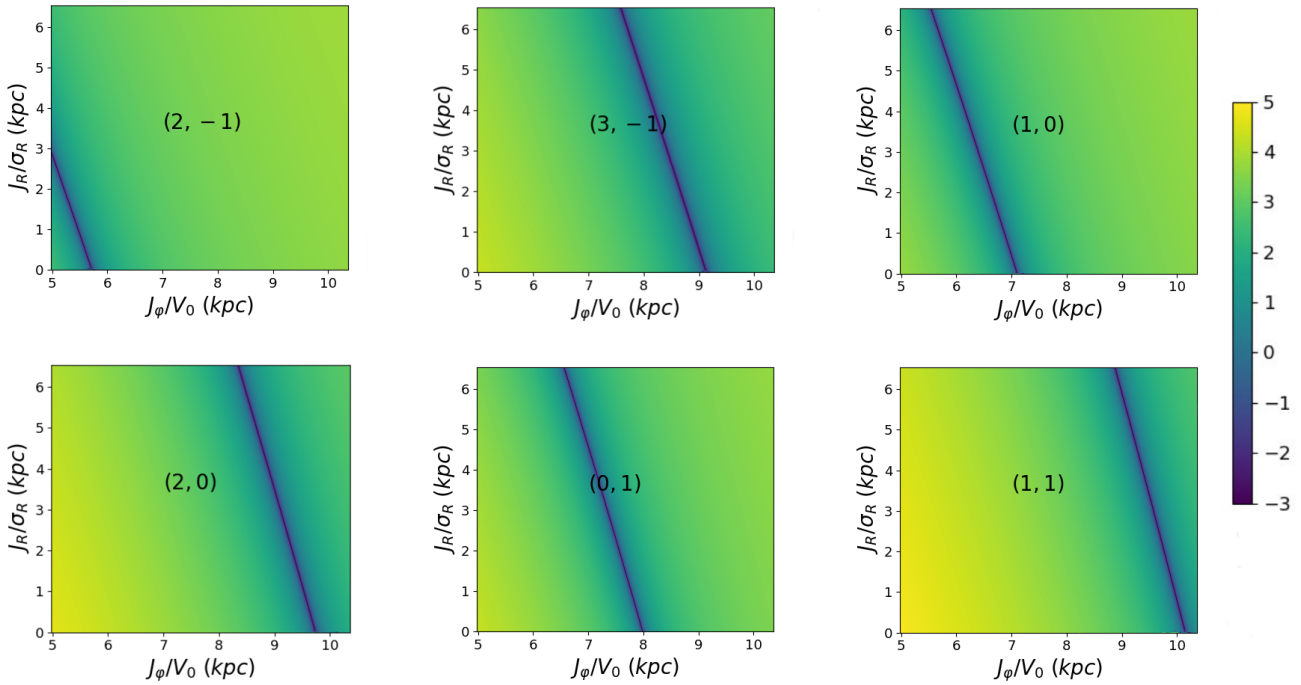

Fig. 5. Values of $\log(\omega_{s,jml})$ in the (J_R, J_φ) plane with fixed $J_z = 10$ kpc km s^{-1}, for a few combinations of (j, l) indices giving rise to resonant zones in action space (recalling that $m = 2$). The pattern speed Ω_p here is $1.89\,\Omega_0$. The two actions are renormalized by the radial velocity dispersion of the thin disc and the circular velocity at the Sun, respectively. The deep blue lines correspond to resonant zones. For instance, the $(1, 0)$ case corresponds to the traditional OLR (for a non-zero J_z). Most other low-order combinations of indices did not give rise to any relevant resonant zone in the region of interest.

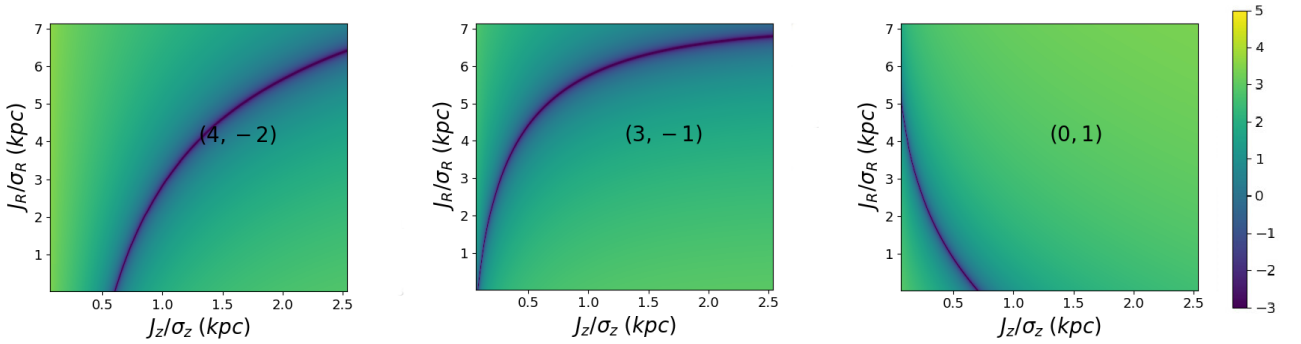

Fig. 6. Values of $\log(\omega_{s,jml})$ in the (J_R, J_z) plane with fixed $J_\varphi = 1759$ kpc km s^{-1} for different (j, l) resonances. The pattern speed Ω_p is that of our fiducial central bar fixed at $1.89\,\Omega_0$. The two actions are renormalized by the radial velocity dispersion and the vertical velocity dispersion of the thin disc at the Sun, respectively. The deep blue lines correspond to resonance zones. Most combinations of indices explored did not give rise to any relevant resonant zone in the region of interest.

3.2. Resonant zones

In the case of a perturbation with quasi-static amplitude that has reached its plateau, once the Fourier coefficients representing the perturbing potential have been computed (from the epicyclic approximation or from Eq. 10) the expression for the perturbed DF can be simply expressed away from resonances with Eq. 7 as

$$f_1(\boldsymbol{J}, \boldsymbol{\theta}, t) = \mathrm{Re}\left\{ \sum_{j,l=-n}^{n} f_{jml}\, \mathrm{e}^{\mathrm{i}[j\theta_R + m(\theta_\varphi - \Omega_p t) + l\theta_z]} \right\}, \tag{19}$$

with n the order of the Fourier series (in this paper, $m = 2$ in both the bar and spiral cases), and

$$f_{jml} = \phi_{jml} \times \frac{j\frac{\partial f_0}{\partial J_R} + m\frac{\partial f_0}{\partial J_\varphi} + l\frac{\partial f_0}{\partial J_z}}{j\omega_R + m(\omega_\varphi - \Omega_p) + l\omega_z}, \tag{20}$$

where ω_R, ω_φ, and ω_z can be approximated as epicyclic frequencies in the epicyclic case or can be determined with `AGAMA`. The denominator of f_{jml} may lead to a divergence in the DF when it approaches zero. Following our notation in Eq. 9, it can be expressed as

$$\omega_{s,jml}(J_R, J_\varphi, J_z) = j\omega_R + m(\omega_\varphi - \Omega_p) + l\omega_z. \tag{21}$$

The amount of the resonances is limited in the epicyclic case because, by construction, indices run only over the values $j = \{-1, 0, 1\}$ and $l = \{-2, 0, 2\}$, but they can be much more numerous in the more accurate `AGAMA` case. For the bar potential of Eq. 11 and Eq. 12, and choosing a pattern speed $\Omega_p = 1.89\Omega_0$ as for our fiducial bar model, we explore in Fig. 5 and Fig. 6, the values of $\omega_{s,jml}(J_R, J_\varphi, J_z)$ in action space when varying the pair of integer indices (j, l). The actions are renormalized by

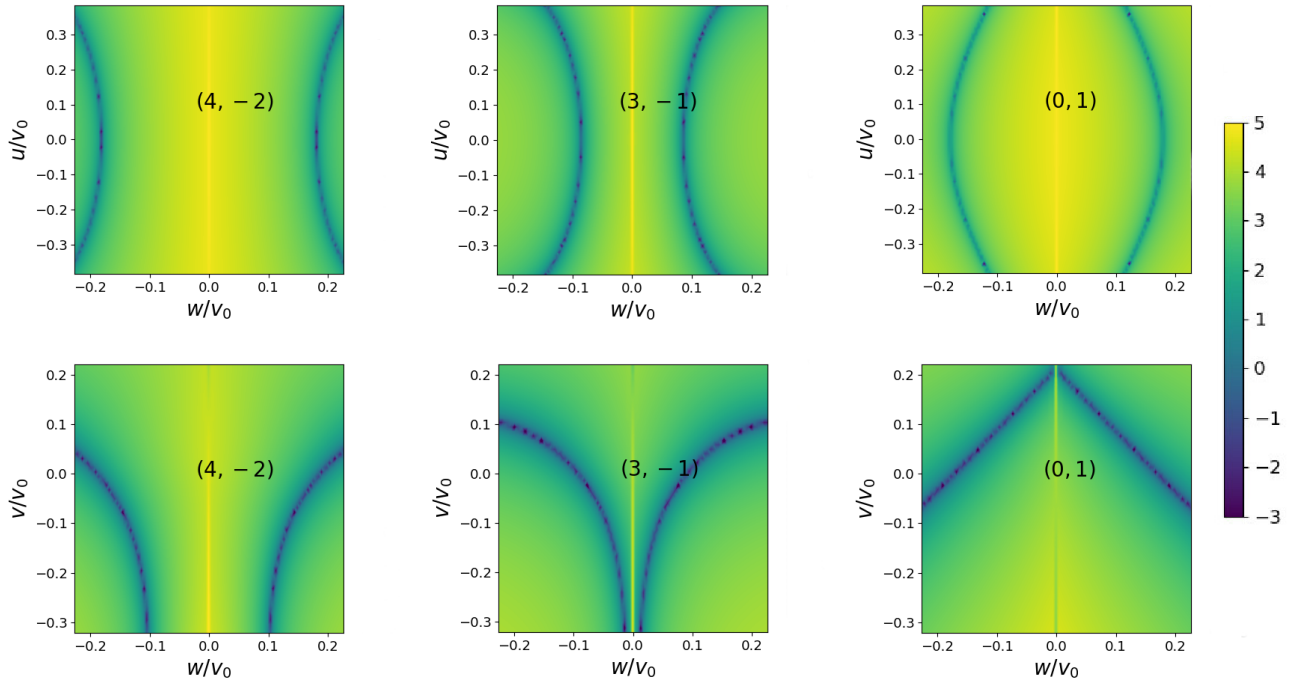

Fig. 7. Values of $log(\omega_{s,jml})$ in the uw-plane and vw-plane. Top row: Values of $log(\omega_{s,jml})$ at $z = 0$ in the uw-plane with fixed $J_\varphi = 1759$ kpc km s^{-1}, for the various vertical resonances relevant in the solar neighbourhood (the $l = 0$ resonances are treated in detail in Sect. 3.3). They all appear at relatively large values of w and are very concentrated in w, varying very quickly in u as a function of w. Bottom row: Values of $log(\omega_{s,jml})$ in the vw-plane with fixed $u = 0$ km s^{-1}. The pattern speed Ω_p is that of our fiducial central bar fixed at 1.89 Ω_0.

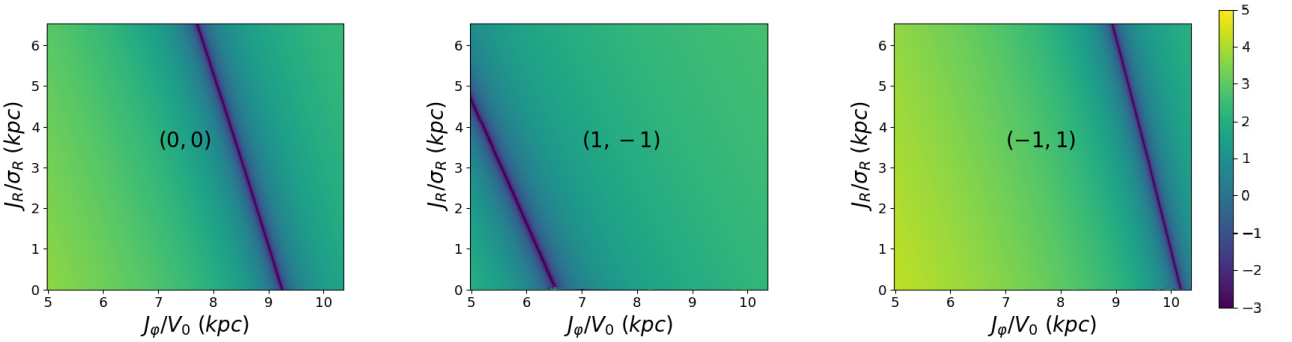

Fig. 8. Same as Fig. 5, but with some combinations of indices giving rise to resonant zones for $\Omega_p = 0.84\,\Omega_0$.

the radial velocity dispersion of the thin disc, circular velocity, and vertical velocity dispersion of the thin disc at the Sun, respectively, to only display a relevant range of actions. Exploring indices in the range $[-4, +4]$, it is clear that most combinations do not induce a resonance that is relevant to the dynamics of the solar neighbourhood. We only display in Fig. 5 and Fig. 6 the combination of indices (in addition to the corotation) for which a resonant zone appears in the plotted region of action space. It is clear that very few low-order resonances are indeed present in the range of actions that are truly relevant for the solar neighbourhood.

To date our method has not been adapted to the projection of the DF on a plane in action space or local velocity space, and therefore works best in 3D. Therefore, we show in Fig. 7 some slices in velocity space at $z = 0$, denoting the location of the vertical resonances (i.e. resonances involving a non-zero l, hence involving the vertical frequency) either for a fixed value of the azimuthal velocity (and action) or for a fixed value of the radial velocity. Identifying such resonances in the vw-plane and uw-plane should allow new types of constraints to be put on the pattern speed of internal perturbers and the vertical shape of the potential of the Galaxy.

Interestingly, most of these resonances are very concentrated in w and vary quickly both in u and v as a function of w, making them elusive to find when stacking tracer stars in any 2D plane of velocity space, but in principle they stand out in thin slices of velocity space. Concretely, when considering a change of 10 km s^{-1} in vertical velocity from 5 to 15 km s^{-1}, the corresponding change in the location of the vertical resonance in v within the uv-plane is always larger than 10 km s^{-1} and typically larger (sometimes much larger) than 30 km s^{-1}.

Moreover, the signature of these vertical resonances in the uv-plane is rather thin, typically of the order of the km s^{-1}, hence much thinner than the displacement of the resonance with w. This means that, when investigating the uv-plane, vertical resonances should mostly be washed out as soon as the investigated

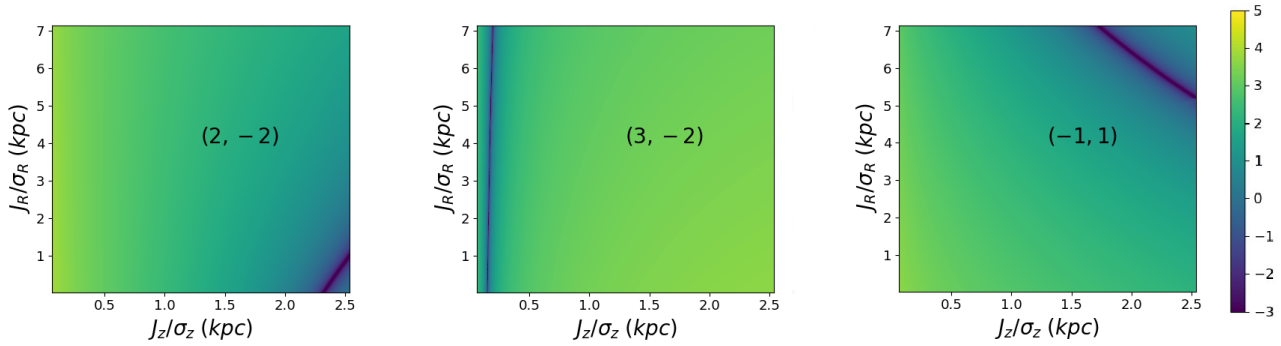

Fig. 9. Same as Fig. 6, but with some combinations of indices giving rise to resonant zones for $\Omega_p = 0.84\,\Omega_0$.

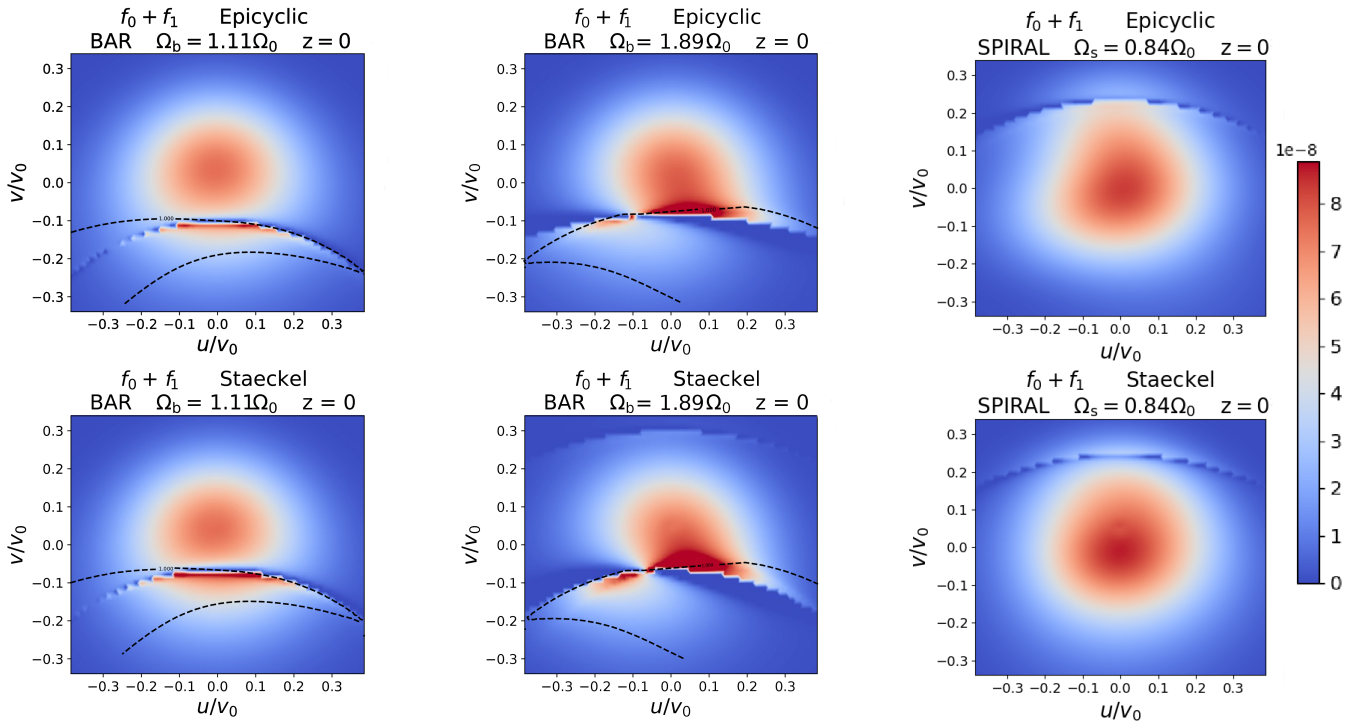

Fig. 10. Distribution function from Fig. 4 in velocity space at the solar position within the Galactic plane, now perturbed to linear order by a bar (perturbing potential from Sect. 2.4) with pattern speeds $\Omega_b = 1.16\,\Omega_0$ (left) and $\Omega_b = 1.89\Omega_0$ (middle), or by a spiral pattern (perturbing potential from Sect. 2.5) with pattern speed $\Omega_{sp} = 0.84\,\Omega_0$ (right). The black dashed contours represent the zones where k is equal to or less than 1, k being a quantity computed in Monari et al. (2017a) that designates the region where the orbits are trapped at the main resonance (the computation used here in the Stäckel case will be presented in detail in Al Kazwini et al., in preparation). Top row: Epicyclic approximation. Bottom row: Stäckel fudge.

slice is thick enough. Therefore, when investigating the DF in the uv-plane in the next subsection, we limit ourselves to the effect of $l = 0$ resonances.

As displayed in Fig. 8 and Fig. 9, for a lower pattern speed $\Omega_p = 0.84\,\Omega_0$, corresponding to the pattern speed of our fiducial spiral potential, a smaller number of vertical resonances are prominent in the solar neighbourhood.

While a specific treatment is needed in these resonant zones (e.g. Monari et al. 2017a), the signature of the resonances (and thus their location in velocity space) can clearly be identified with our linear perturbation method, and the linear perturbation treatment hereafter should accurately describe the deformations of velocity space outside of these resonant zones.

3.3. Comparing the perturbed DF for different action estimates

We are now in a position to compare the linear deformation of local velocity space for different action estimates, namely the epicyclic case used in previous works and the more accurate `AGAMA` action estimates. Since our method works best for now in 3D velocity space, we limit ourselves to slices of zero vertical velocity at different heights and to $l = 0$ resonances.

Figure 10 displays the $f_0 + f_1$ linearly perturbed distribution function at the position of the Sun in the Galactic plane for the bar potential of Sect. 2.4 and two different pattern speeds, and for the spiral potential of Sect. 2.5. As in Monari et al. (2017b), whenever $f_1 > f_0$, we cap f_1 at the value of f_0 to roughly represent the resonant zone. The more rigorous approach, which we leave to further work in the context of `AGAMA` actions (Al Kazwini et al., in prep.), is to treat the DF with the method of

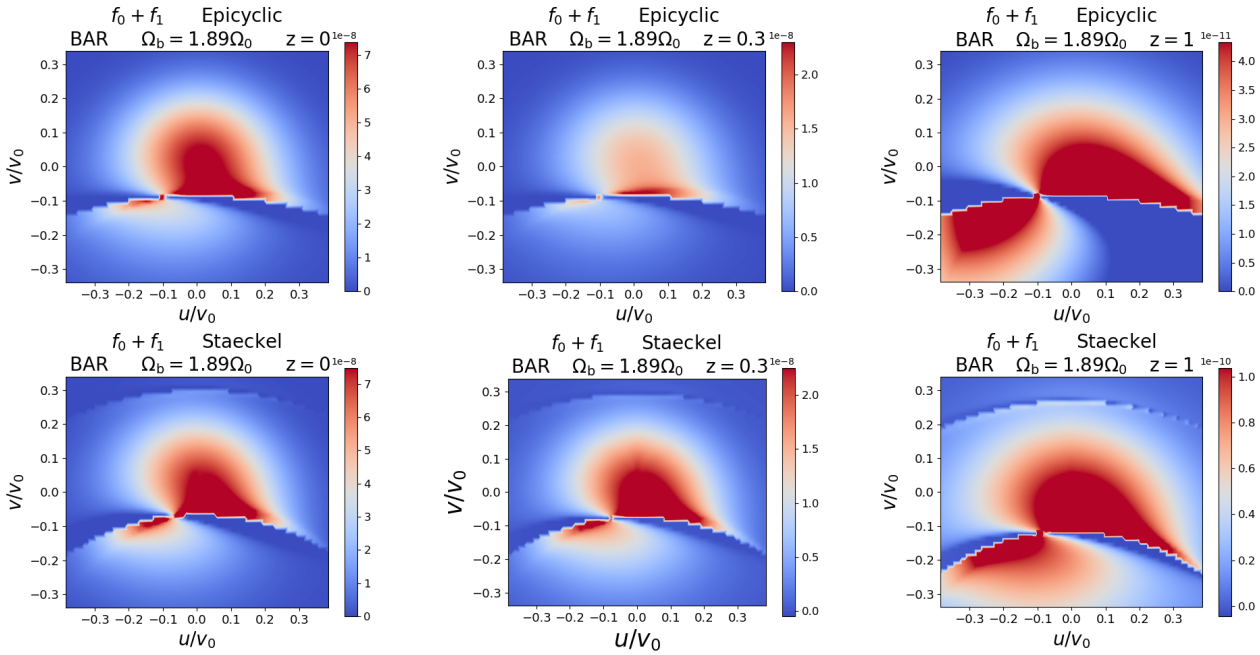

Fig. 11. Local stellar velocity distribution perturbed to linear order at the solar galactocentric radius and azimuth at three different heights (left: $z = 0$ kpc, middle: $z = 0.3$ kpc, right: $z = 1$ kpc), when perturbed by a bar (perturbing potential of Sect. 2.4) with pattern speed $\Omega_b = 1.89\Omega_0$. Top row: Epicyclic approximation. Bottom row: Stäckel fudge. The scale of the colour bar is different in the upper and lower panels for $z = 1$ kpc.

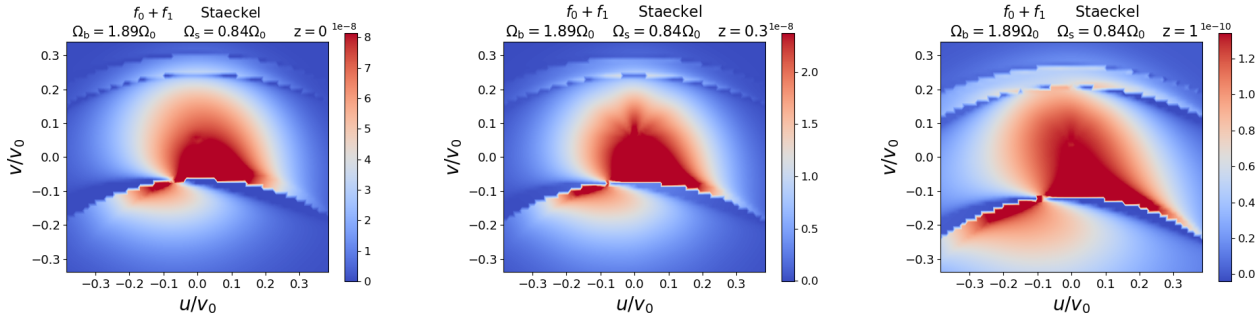

Fig. 12. Same as Fig. 11, in the Stäckel fudge case, but now for joint perturbation by a bar (perturbing potential of Sect. 2.4) with pattern speed $\Omega_b = 1.89\Omega_0$ and a spiral pattern (perturbing potential of Sect. 2.5) with pattern speed $\Omega_{sp} = 0.84\,\Omega_0$.

Monari et al. (2017a) in these regions. However, while the DF within the resonant zone is not well modelled by the present method, the *location* and global shape of resonances should be well reproduced. We indeed highlight in Fig. 10 the zone occupied by trapped orbits at the corotation ($\Omega_b = 1.16\,\Omega_0$) and OLR ($\Omega_b = 1.89\Omega_0$) of the bar, as determined with the method of Monari et al. (2017a) both in the epicyclic and `AGAMA` cases (Al Kazwini et al. in prep.). While the *quantitative* enhancement of the DF will be slightly different from our linear treatment in these trapping zones, it is clear that the location of the resonant deformation is well captured by the method, as expected. The linear deformation outside of the resonant zones should be well described by our method as well. Interestingly enough, the linear deformation due to the bar is generally stronger in the `AGAMA` case, and that due to the spiral is weaker in the `AGAMA` case. This means that reproducing the effect of spiral arms on the local velocity distribution might require a higher amplitude when considering an accurate estimate of the action-angle variables rather than the epicyclic approximation. We speculate that this is related to the inaccuracy of the reconstruction of the potential in the epicyclic case, which causes different biases in the spiral and bar cases.

The case of the pattern speed of the bar being $1.89\,\Omega_0$ would correspond to a configuration where the Hercules stream at negative u and negative v corresponds to the $2:1$ outer Lindblad resonance of the bar (e.g. Dehnen 2000; Minchev et al. 2007; Monari et al. 2017b; Fragkoudi et al. 2019). Although this happens in the resonant zone, it is interesting to note that this feature is less squashed in the more realistic `AGAMA` case. Moreover, a resonance unnoticed within the epicyclic approximation appears at high azimuthal velocities: we can identify this resonance as the outer $1:1$ resonance of the bar (Dehnen 2000). In the spiral case, the resonant ridge at large azimuthal velocities can be identified as the corotation of the spiral pattern.

Figure 11 displays the linear deformation due to the bar, for the case of pattern speed of $1.89\,\Omega_0$, at different heights above the Galactic plane, both in the epicyclic and `AGAMA` cases. We again restrict ourselves to a zero vertical velocity slice and $l = 0$ resonances. As can be seen in this figure, the epicyclic approximation quickly becomes imprecise at large heights because it implies a stronger falloff of the density with height (as already noted in Fig. 4) while not changing the azimuthal velocity distribution (and the location of resonances in v) due to the hypothesis of complete decoupling of vertical motions.

In the AGAMA case the azimuthal velocity distribution is affected by a larger asymmetric drift at large heights, and the location of the outer Lindblad resonance of the bar in the uv-plane is also displaced to lower azimuthal v at larger heights. This occurs because at fixed J_φ the azimuthal and radial frequencies computed with AGAMA are lower at higher z, meaning that one needs to reach lower J_φ (corresponding to orbits whose guiding radii are in the inner Galaxy) to reach the resonance.

This trend is most clearly visible at $z = 1$ kpc, where the epicyclic approximation does not accurately represent the location of the Hercules feature compared to the AGAMA case. Interestingly, comparing the displacement with height of the OLR in the case of a bar with pattern speed $1.89\,\Omega_0$ with that of the corotation in the case of a $1.16\,\Omega_0$ pattern speed, we noted that the corotation location in the uv-plane is more displaced than the OLR. This is because the corotation only depends on the azimuthal frequency, while the OLR depends on a combination of the azimuthal and radial frequencies. On the other hand, with the presently assumed background potential, we found that the displacement with height was rather independent of the pattern speed and therefore of the location of the resonance in local velocity space. We found a gradient in v of 8 $\mathrm{kms^{-1}kpc^{-1}}$ for the corotation, 6 $\mathrm{kms^{-1}kpc^{-1}}$ for the OLR, and 4 $\mathrm{kms^{-1}kpc^{-1}}$ for the $1:1$ resonance. This different displacement can also be seen when linearly adding the effect of the bar and spiral in Fig. 12, where the spacing between the $1:1$ resonance of the bar and that of the corotation of the spiral increases with height.

Quantitatively, these displacements depend strongly on the background Galactic potential. This means that once the resonances potentially responsible for moving groups in the solar neighbourhood have been identified, studying their position in the uv-plane as a function of z can in principle be a powerful new way to constrain the 3D structure of the Galactic potential. This cannot be done within the epicyclic approximation. We note that marginalizing over vertical velocities instead of taking a zero-velocity slice would not compensate for these variations of the location of resonances with height but would only enhance the effect. In practice, we investigated the displacement of the location of the in-plane OLR with vertical velocities. For $w = 50$ km s^{-1} the displacement compared to $w = 0$ km s^{-1} in terms of the v-location of the resonance at $z = 1$ kpc is 8 km s^{-1}, always towards lower azimuthal velocities; however, the signal will always be dominated by the lowest w values due to the vertical orbital structure of the disc.

4. Adding the temporal evolution

In the previous sections we always consider a constant amplitude for the perturbing potential in order to determine an analytical expression for the perturbed DF. In this section we investigate the time dependence of the DF by choosing a time-varying amplitude for the perturbing potential.

4.1. Time-varying amplitude function

The expression we use for the time-dependent function g controlling the amplitude of the perturbation during its growth is

$$g(t) = \frac{1 - \cos(\pi t/t_\mathrm{f})}{2}, \tag{22}$$

where t_f is the time at which the perturbation is completely formed, expressed in Gyr. We consider $t_\mathrm{f} = 0.5$ Gyr.

The motivation for this choice of growth function is its analytic simplicity, having a function starting from exactly zero at the origin, and smooth over the whole considered range. The first derivative, $[\pi/(2t_\mathrm{f})]\sin(\pi t/t_\mathrm{f})$, assures the continuity at 0 and t_f with both stages, fixed at 0 for $t \le 0$ and at 1 for $t \ge t_\mathrm{f}$ (the first derivative is thus equal to 0 at 0 and t_f).

4.2. Time-dependent perturbed distribution function

We now take the integral of Eq. (6), restricted to $[0, t]$ (because the g function is equal to 0 on $]-\infty, 0]$) and integrate by parts. We take $\phi_{\boldsymbol{n}}(\boldsymbol{J}', t') = g(t')\,h(t')\,\phi_{\boldsymbol{n}}(\boldsymbol{J})$, with $h(t') = \mathrm{e}^{-\mathrm{i}m\Omega_\mathrm{p}t'}$, and we define

$$\eta(t) \equiv \frac{\mathrm{e}^{\mathrm{i}\theta_{\mathrm{s},\boldsymbol{n}}(t)}}{\mathrm{i}\omega_{\mathrm{s},\boldsymbol{n}}} \rightarrow \mathrm{d}\eta = \mathrm{e}^{\mathrm{i}\theta_{\mathrm{s},\boldsymbol{n}}(t)}\mathrm{d}t, \tag{23}$$

allowing us to rewrite Eq. (6) as

$$f_1(\boldsymbol{J}, \boldsymbol{\theta}, t) = \mathrm{Re}\left\{\mathrm{i}\frac{\partial f_0}{\partial \boldsymbol{J}}(\boldsymbol{J}) \cdot \sum_{\boldsymbol{n}} \boldsymbol{n}\phi_{\boldsymbol{n}}(\boldsymbol{J}) \int_0^t g(t')\frac{\mathrm{d}\eta}{\mathrm{d}t'}(t')\,\mathrm{d}t'\right\}. \tag{24}$$

We can now integrate by parts

$$\int_0^t g(t')\frac{\mathrm{d}\eta}{\mathrm{d}t'}(t')\,\mathrm{d}t' = [g(t')\eta(t')]_0^t - \int_0^t \frac{\mathrm{d}g}{\mathrm{d}t'}(t')\,\eta(t')\,\mathrm{d}t', \tag{25}$$

and since $g(0) = 0$,

$$[g(t')\eta(t')]_0^t = g(t)\eta(t). \tag{26}$$

To calculate the second part of the integral, since $\mathrm{d}g(t)/\mathrm{d}t = \pi/(2t_\mathrm{f})\sin(\pi t/t_\mathrm{f})$, we write,

$$\int_0^t \frac{\mathrm{d}g}{\mathrm{d}t'}(t')\eta(t')\mathrm{d}t' = \frac{\pi}{2t_\mathrm{f}}\frac{1}{\mathrm{i}\omega_{\mathrm{s},\boldsymbol{n}}}\int_0^t \sin\left(\frac{\pi t'}{t_\mathrm{f}}\right)\mathrm{e}^{\mathrm{i}\theta_{\mathrm{s},\boldsymbol{n}}(t')}\mathrm{d}t'. \tag{27}$$

We look for a primitive G of $\sin(\pi t/t_\mathrm{f})\mathrm{e}^{\mathrm{i}\theta_{\mathrm{s},\boldsymbol{n}}(t)}$ of the form

$$G(t) = \left[A\cos\left(\frac{\pi t}{t_\mathrm{f}}\right) + B\sin\left(\frac{\pi t}{t_\mathrm{f}}\right)\right]\mathrm{e}^{\mathrm{i}\theta_{\mathrm{s},\boldsymbol{n}}(t)}. \tag{28}$$

Deriving $G(t)$ with respect to t, and equating it to the integrand in Eq. 27 we get

$$B\frac{\pi}{t_\mathrm{f}} + A\,\mathrm{i}\omega_{\mathrm{s},\boldsymbol{n}} = 0 \quad \text{and} \quad B\,\mathrm{i}\omega_{\mathrm{s},\boldsymbol{n}} - A\frac{\pi}{t_\mathrm{f}} = 1, \tag{29}$$

which leads to

$$A = \frac{\pi/t_\mathrm{f}}{\omega_{\mathrm{s},\boldsymbol{n}}^2 - (\pi/t_\mathrm{f})^2} \quad \text{and} \quad B = \frac{-\mathrm{i}\omega_{\mathrm{s},\boldsymbol{n}}}{\omega_{\mathrm{s},\boldsymbol{n}}^2 - (\pi/t_\mathrm{f})^2}. \tag{30}$$

Substituting the Eqs. (26) and (28) into Eq. (25) results in the following expression for the perturbed DF

$$\begin{aligned} f_1(\boldsymbol{J}, \boldsymbol{\theta}, t) = \mathrm{Re}\Bigg\{&\frac{\partial f_0}{\partial \boldsymbol{J}}(\boldsymbol{J}) \cdot \sum_{\boldsymbol{n}} \boldsymbol{n}\,\phi_{\boldsymbol{n}}(\boldsymbol{J}) \times \\ &\left[\frac{1}{2}\left(1 - \cos\left(\frac{\pi t}{t_\mathrm{f}}\right)\right)\frac{\mathrm{e}^{\mathrm{i}\theta_{\mathrm{s},\boldsymbol{n}}}}{\omega_{\mathrm{s},\boldsymbol{n}}} - \frac{\pi}{2t_\mathrm{f}}\frac{1}{\omega_{\mathrm{s},\boldsymbol{n}}}\frac{1}{\omega_{\mathrm{s},\boldsymbol{n}}^2 - (\pi/t_\mathrm{f})^2} \times \right. \\ &\left.\left(\left(\frac{\pi}{t_\mathrm{f}}\cos\left(\frac{\pi t}{t_\mathrm{f}}\right) - \mathrm{i}\omega_{\mathrm{s},\boldsymbol{n}}\sin\left(\frac{\pi t}{t_\mathrm{f}}\right)\right)\mathrm{e}^{\mathrm{i}\theta_{\mathrm{s},\boldsymbol{n}}} - \frac{\pi}{t_\mathrm{f}}\mathrm{e}^{\mathrm{i}(\theta_{\mathrm{s},\boldsymbol{n}} - \omega_{\mathrm{s},\boldsymbol{n}}t)}\right)\right]\Bigg\}. \end{aligned} \tag{31}$$

It should be noted that we do not exactly recover the static case at $t = t_f$ because not *all* derivatives of $g(t)$ are strictly zero at the initial and final time, as assumed in M16. If a true plateau is

reached after t_f in an analytic fashion, the function would nevertheless converge towards the static case. How quickly this would happen is not trivial to compute. We can however compute an upper limit based on the formalism of Monari et al. (2017a). Considering that the most trapped orbits have their slow variables following the behaviour of a harmonic oscillator, and taking 2π over the frequency of this harmonic oscillator as a characteristic time for phase-mixing, we obtain a characteristic time of the order of 2 Gyr.

Now we can study analytically how the linear response to a fiducial bar with $\Omega_b = 1.89\Omega_0$ evolves with time. As before the method is not strictly valid at resonances, where a treatment like that used in Monari et al. (2017a) must be applied (see also Binney 2020a,b). It is nevertheless interesting to see in Fig. 13 how the linear deformation of the velocity plane evolves with time near resonances (in a patch co-moving with the bar, hence at a constant azimuthal angle to the bar), while the amplitude of the perturbation grows. The effect of the OLR appears as soon as the perturbation starts to grow. As it progressively grows, the two linear modes in the DF separate and lead to a velocity plane already very much resembling the stationary form of the perturbed DF after 0.25 Gyr, that is when $g(t) = 0.5$ and the perturbation is half-formed. In the absence of a pattern speed variation, it is therefore not necessarily obvious to disentangle the effect of a bar whose amplitude is growing from that of a fully formed bar with larger and constant amplitude.

5. Conclusion

Starting from the formalism exposed in M16, we proposed a more accurate way to determine the DF of the Galactic disc perturbed to linear order by a non-axisymmetric perturbation, using a more accurate action-angle coordinate system. First, we used the torus mapping from `AGAMA` to numerically compute the perturbing potential in action-angle coordinates as a Fourier series expansion over the angles. We showed that we could estimate typical non-axisymmetric perturbing potentials with an accuracy at the per cent level. The algorithm can be applied to any perturbing potential, including non-plane symmetric vertical perturbations, which will be particularly important when studying the vertical perturbations of the disc with similar methods (Rozier et al., in prep.).

We then computed the DF perturbed to linear order by a typical bar or spiral potential (or a linear combination of both), and computed the local stellar velocity distribution by converting velocities to actions and angles through the Stäckel fudge implemented in `AGAMA`. The results were compared to those obtained by using the epicyclic approximation. The linear deformation due to the bar is generally stronger in the `AGAMA` case, and that due to the spiral is weaker in the `AGAMA` case. This means that reproducing the effect of spiral arms on the local velocity distribution might require a higher amplitude when considering an accurate estimate of the action-angle variables rather than the epicyclic approximation. Most importantly, the epicyclic approximation is inadequate at large heights and does not change the azimuthal velocity location of the resonances due to the hypothesis of complete decoupling of vertical motions. In the `AGAMA` case instead, the locations of resonances are displaced to lower azimuthal v at larger heights. With the background potential used in this paper, we found a displacement in v of 8 $\mathrm{kms^{-1}kpc^{-1}}$ for the corotation, 6 $\mathrm{kms^{-1}kpc^{-1}}$ for the OLR and 4 $\mathrm{kms^{-1}kpc^{-1}}$ for the $1:1$ resonance. Thus, the position of moving groups in the uv-plane as a function of z can be a powerful way to constrain the 3D structure of the Galactic potential. The key to exploring this will be the DR3 of Gaia (Brown 2019) with its $\sim$ 35 million radial velocities allowing us to better probe the z-axis above and below the Milky Way plane.

Finally, the temporal treatment is also an improvement over M16. We applied it to the case of a bar of growing amplitude, with an analytic evolution of the amplitude. As the bar progressively grows, the two linear modes in the DF separate, and lead to a velocity plane already very much resembling the stationary form of the perturbed DF once the perturbation is half-formed. In the absence of a pattern speed variation, it is therefore not necessarily obvious to disentangle the effect of a bar whose amplitude is growing from that of a fully formed bar with larger and constant amplitude. We explored here a peculiar form of the growth function motivated by its analytic simplicity. If the perturbation grows by linear instability, exponential growth will be more realistic. Numerical experiments are usually well fitted by a logistic function (exponential growth at the beginning and saturation to the plateau). One problem for our treatment is that the logistic function is never strictly equal to 0. In addition, there is hope that similar analytical simplifications such as those for the amplitude growth studied here can also be made with this function, which we will investigate in the future.

While the form of the DF is not well estimated in the resonant zones with the linear perturbations presented in this paper, the signature of the resonances (and thus their location in velocity space) can clearly be identified with this linear perturbation method. The more rigorous approach, which we leave to further works in the context of `AGAMA` actions (Al Kazwini et al., in prep.), is to treat the DF with a method like that of Monari et al. (2017a) in these regions, patching these results over the linear deformation computed here. Another caveat is that the torus mapping was used to express the perturbing potential in actions and angles, but for the estimate of the local stellar velocity field, we made use of the less precise Stäckel fudge method. Therefore, another promising way for improvement would be to use the new `ACTIONFINDER` deep-learning algorithm (Ibata et al. 2021) to make the reverse transformation. Finally, the results presented in this paper were obtained in 3D action and velocity spaces, and were mostly presented in 2D slices: it would therefore be particularly useful to improve our algorithm by including a marginalization over any axis, for instance marginalizing over vertical velocities. This is computationally more intensive but should not, a priori, pose any conceptual problem.

The tools presented in this paper will be useful for a thorough analytical dynamical modelling of the complex velocity distribution of Milky Way disc stars as measured by past and upcoming Gaia data releases. These tools will also be useful for fully self-consistent treatments of the response of the disc to external perturbations. The ultimate goal is to adjust models to the exquisite data from Gaia, which cannot be done properly with N-body simulations due to the vast parameter space to explore. The theoretical tools and the new code presented in this paper consequently represent a useful step in this direction.

Acknowledgements. We thank the referee, Dr Paul McMillan, for a thoughtful and constructive report which has helped improving the paper and correcting a small bug in the first version. AS, BF, GM, SR, PR and RI acknowledge funding from the Agence Nationale de la Recherche (ANR project ANR-18-CE31-0006 and ANR-19-CE31-0017) and from the European Research Council (ERC) under the European Union's Horizon 2020 research and innovation programme (grant agreement No. 834148).

References

Antoja, T., Helmi, A., Romero-Gómez, M., et al. 2018, Nature, 561, 360

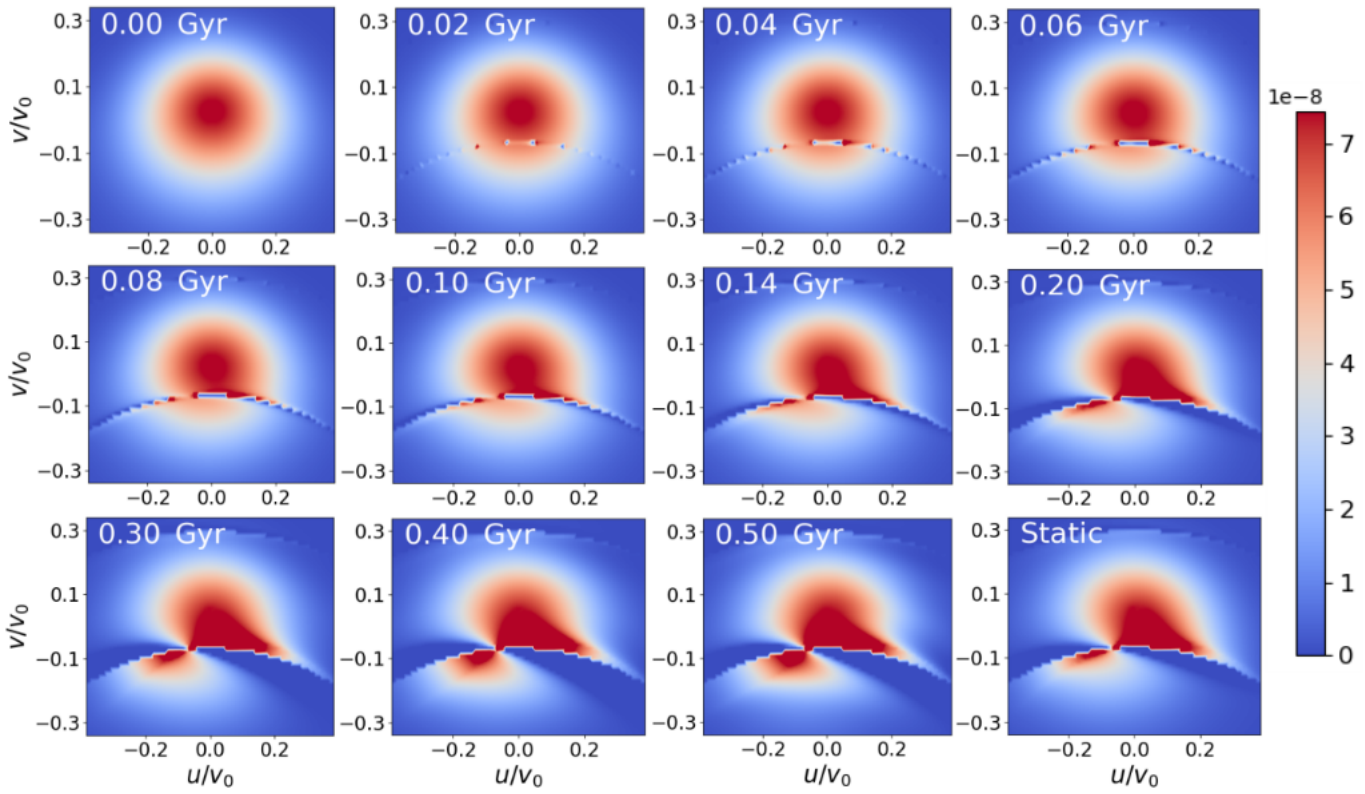

Fig. 13. Local stellar velocity distribution perturbed to linear order in the Galactic plane by the bar of Sect. 2.4 with $\Omega_b = 1.89\Omega_0$ with the Stäckel fudge, and an amplitude of the bar growing as described in Sect. 4.1. The first 11 panels display the temporal evolution of the perturbation. The last panel displays the stationary case. The amplitude of the bar goes from 0 at $t = 0$ to its plateau ($g(t) = 1$) at $t = 0.5$ Gyr.

Binney, J. 2012, MNRAS, 426, 1324
Binney, J. 2020a, MNRAS, 495, 886
Binney, J. 2020b, MNRAS, 495, 895
Binney, J. & McMillan, P. 2011, MNRAS, 413, 1889
Binney, J. & McMillan, P. J. 2016, MNRAS, 456, 1982
Binney, J. & Piffl, T. 2015, MNRAS, 454, 3653
Binney, J. & Schönrich, R. 2018, MNRAS, 481, 1501
Binney, J. & Tremaine, S. 2008, Galactic Dynamics: Second Edition (Princeton University Press)
Bland-Hawthorn, J. & Tepper-García, T. 2021, MNRAS, 504, 3168
Brown, A. G. A. 2019, in The Gaia Universe, 18
Chiba, R., Friske, J. K. S., & Schönrich, R. 2021, MNRAS, 500, 4710
Cole, D. R. & Binney, J. 2017, MNRAS, 465, 798
Cox, D. P. & Gómez, G. C. 2002, ApJS, 142, 261
Dehnen, W. 1998, AJ, 115, 2384
Dehnen, W. 2000, AJ, 119, 800
Famaey, B. & Dejonghe, H. 2003, MNRAS, 340, 752
Famaey, B., Jorissen, A., Luri, X., et al. 2005, A&A, 430, 165
Fragkoudi, F., Katz, D., Trick, W., et al. 2019, MNRAS, 488, 3324
Gaia Collaboration, Brown, A. G. A., Vallenari, A., et al. 2018a, A&A, 616, A1
Gaia Collaboration, Brown, A. G. A., Vallenari, A., et al. 2021, A&A, 649, A1
Gaia Collaboration, Katz, D., Antoja, T., et al. 2018b, A&A, 616, A11
Hilmi, T., Minchev, I., Buck, T., et al. 2020, MNRAS, 497, 933
Ibata, R., Diakogiannis, F. I., Famaey, B., & Monari, G. 2021, ApJ, 915, 5
Laporte, C. F. P., Famaey, B., Monari, G., et al. 2020, A&A, 643, L3
Laporte, C. F. P., Minchev, I., Johnston, K. V., & Gómez, F. A. 2019, MNRAS, 485, 3134
McGill, C. & Binney, J. 1990, MNRAS, 244, 634
Minchev, I., Nordhaus, J., & Quillen, A. C. 2007, ApJ, 664, L31
Monari, G., Famaey, B., Fouvry, J.-B., & Binney, J. 2017a, MNRAS, 471, 4314
Monari, G., Famaey, B., & Siebert, A. 2016, MNRAS, 457, 2569
Monari, G., Famaey, B., Siebert, A., et al. 2019a, A&A, 632, A107
Monari, G., Famaey, B., Siebert, A., et al. 2017b, MNRAS, 465, 1443
Monari, G., Famaey, B., Siebert, A., Wegg, C., & Gerhard, O. 2019b, A&A, 626, A41
Press, W. H., Teukolsky, S. A., Vetterling, W. T., & Flannery, B. P. 1992, Numerical Recipes in C: Second Edition (Cambridge University Press)
Ramos, P., Antoja, T., & Figueras, F. 2018, A&A, 619, A72
Sanders, J. L. & Binney, J. 2016, MNRAS, 457, 2107
Sellwood, J. A. & Carlberg, R. G. 2014, ApJ, 785, 137
Trick, W. H., Coronado, J., & Rix, H.-W. 2019, MNRAS, 484, 3291
Vasiliev, E. 2018, AGAMA: Action-based galaxy modeling framework, Astrophysics Source Code Library
Vasiliev, E. 2019, MNRAS, 482, 1525
Weinberg, M. D. 1994, ApJ, 420, 597

Appendix A: PERDIGAL code presentation

All the results shown in this article were obtained with a single code, written in C++ and Python, that calculates both the perturbing potential in action-angle coordinates and the perturbed DF. The code is named the PERturbed DIstribution functions for the GALactic disc (`PERDIGAL`) and will be made available on request, although it may eventually be embedded in a larger Galactic dynamics toolkit. Launching the code without argument gives the explanations shown in Fig. A.1.

The calculation of the perturbed DF consists of five steps: the creation of a file storing the positions of the DF (DFpos), the creation (via `AGAMA`) of several files containing positions from the many orbits (FCorb) required for the following step, the determination of Fourier coefficients for the perturbing potential to create the grid (FCgrid), the determination of the Fourier coefficients for each position which the DF will be calculated at (FCforDF), and finally the calculation of the perturbed DF (PertDF).The mode ALL processes the three steps (FCgrid, FCforDF, and PertDF) at one time, without saving Fourier coeffcients from FCgrid and FCforDF in files. However, ALL should not be used without certainty about the decomposition of the potential. This process strongly depends on the initial conditions fed to the code, and a check after each part of the calculation is recommended. Finally, PDFdisp displays the perturbed DF using Matplotlib.

All useful parameters are stored in two particular files and can be modified without compiling the code. They contain parameters for the calculation of Fourier coefficients, parameters for the perturbing potentials, and others depending on whether the DF is determined at first or second order, or with a time-dependent amplitude for the perturbing potential. Figure A.2 is a logigram recalling the procedure of the calculation of the perturbed DF.

```
---- ---- ---- ----
Use: ./PDF [-option MODE] POTENTIALS_LIST
 or: ./PDF FUNCTION
---- ---- ---- ----
[MODE] = FCgrid  (calculate the grid of Fourier coefficients and store it in a file)
         FCforDF (calculate the Fourier coefficients for each position of the Distribution Function and store it in a file)
         PertDF  (calculate the Perturbed Distribution Function and store it in a file)
         PDFdisp (display the Perturbed Distribution Function)
         ALL     (execute the three above modes)
         EPI     (calculate the Perturbed Distribution Function with the epicyclic approximation and store it in a file)
---- ---- ---- ----
FUNCTION = DFpos   (create a file with the positions of the Distribution Function)
           FCorb   (create files with positions on orbits used to create the Fourier coefficients grid)
           Freq    (create a grid of Staeckel frequencies and store it in a file)
           Moments (calculate the moments of the potential and store them in a file)
           Momdisp (display the moments)
---- ---- ---- ----
```

Fig. A.1. Guide for the use of the code. The first three modes deal with the determination of the Fourier coefficients when expanding in series the perturbing potential (FCgrid and FCforDF), and the calculation of the perturbed distribution function (PertDF). PDFdisp allows this function to be displayed as a distribution of velocities. ALL regroups these modes into one, but it is not recommended because of the need to check the Fourier decomposition. EPI directly calculates the perturbed distribution function under the epicyclic approximation, as explained in M16. The FUNCTIONs correspond to different operations required before using the MODEs. DFpos creates the file storing the positions at which the distribution function will be determined. FCorb creates several files containing positions from the many orbits needed to calculate the Fourier coefficients in the FCgrid step.

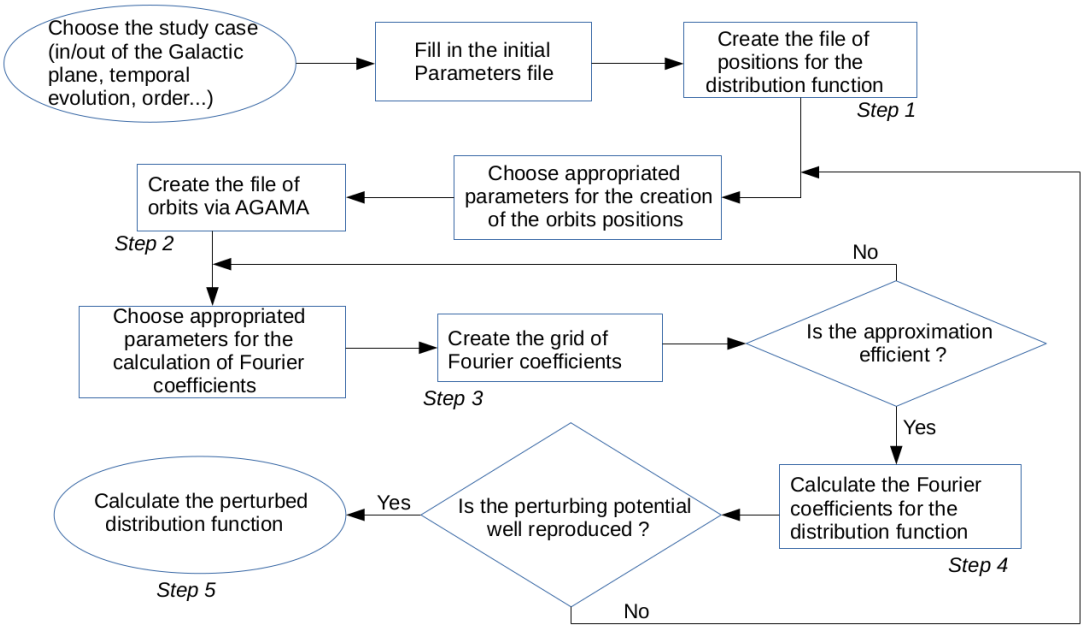

Fig. A.2. Logigram recalling the procedure of the calculation of the perturbed DF. The different steps 1-5 correspond respectively to the modes DFpos, FCorb, FCgrid, FCforDF, and PertDF. There are two cases where the result of the code needs to be verified: after the third step (to check that the decomposition is correct) and after the fourth step (to check that the perturbing potential is well reproduced).

Astronomy & Astrophysics manuscript no. output
May 31, 2022

From ridges to manifolds: 3D characterization of the moving groups in the Milky Way disc

M. Bernet[1,2,3], P. Ramos[1,2,3,4], T. Antoja[1,2,3], B. Famaey[4], G. Monari[4], H. Al Kazwini[4], and M. Romero-Gómez[1,2,3]

[1] Departament de Física Quàntica i Astrofísica (FQA), Universitat de Barcelona (UB), C Martí i Franquès, 1, 08028 Barcelona, Spain
e-mail: mbernet@fqa.ub.edu
[2] Institut de Ciències del Cosmos (ICCUB), Universitat de Barcelona (UB), C Martí i Franquès, 1, 08028 Barcelona, Spain
[3] Institut d'Estudis Espacials de Catalunya (IEEC), C Gran Capità, 2-4, 08034 Barcelona, Spain
[4] Université de Strasbourg, CNRS, Observatoire astronomique de Strasbourg, 11 rue de l'Université, 67000 Strasbourg, France

Received September 15, 1996; accepted March 16, 1997

ABSTRACT

Context. The details of the effect of the bar and spiral arms on the disc dynamics of the Milky Way are still unknown. The stellar velocity distribution in the Solar Neighbourhood displays kinematic substructures, which are possibly signatures of these processes and of previous accretion events. With the Gaia mission, more detail of these signatures, such as ridges in the V_ϕ-R plane and thin arches in the V_ϕ-V_R plane, has been revealed. The positions of these kinematic substructures –moving groups– can be thought of as continuous manifolds in the 6D phase space, and the ridges and arches as specific projections of these manifolds.
Aims. We aim to detect and characterize the moving groups along the Milky Way disc, obtaining a sampling of the velocities and positions of the manifolds in a 5D space (Galactocentric radial and azimuthal velocities and 3D configuration space).
Methods. We develop and apply a novel methodology to perform a blind search for substructure in the Gaia EDR3 6D data, which consists in the execution of the Wavelet Transform in independent small volumes of the Milky Way disc, and the grouping of these local solutions into global structures with a method based on the Breadth-first search algorithm from Graph Theory. We apply the same methodology to simulations of barred galaxies to validate the method and to compare with the data.
Results. We reveal the skeleton of the velocity distribution, uncovering projections that were not possible before. We sample nine main moving groups along a large region of the disc in configuration space, covering up to 6 kpc, 60 deg, and 2 kpc in the radial, azimuthal, and vertical directions respectively, extending significantly the range of previous analysis. In the radial direction, we find that the groups deviate from the lines of constant angular momentum that one would naively expect from an epicyclic approximation analysis of the first order effects of resonances. In fact, we reveal that the spatial evolution of the moving groups is complex and that the configuration of moving groups in the Solar Neighbourhood is not maintained along the disc. We also find that the azimuthal velocity of the moving groups that are mostly detected in the inner parts of the disc (*Acturus*, *Bobylev*, and *Hercules*) is non-axisymmetric. For *Hercules*, we measure an azimuthal gradient of $-0.50\,\mathrm{kms}^{-1}\mathrm{deg}^{-1}$ at $R = 8$ kpc. We detect a vertical asymmetry in the azimuthal velocity for the *Coma Berenices* moving group which is not expected for structures originating from a resonance of the bar, supporting the previous hypothesis of the incomplete vertical phase-mixing of the group. In our simulations, we extract substructures corresponding to the Outer Linbdlad Resonance and the 1:1 resonances and observe the same deviation from constant angular momentum lines and the non-axisymmetry of the azimuthal velocities of the moving groups in the inner part of the disc.
Conclusions. This data-driven characterization is a starting point for a holistic understanding of the moving groups. It also allows for a quantitative comparison with models, providing a key tool to comprehend the dynamics of the Milky Way.

Key words. Galaxy: disc – Galaxy: kinematics and dynamics – Galaxy: structure – Galaxy: evolution – Methods: data analysis

1. Introduction

The stellar velocity distribution in the solar neighbourhood (SN) has been for a long time a key element in our understanding of the structure of the Milky Way (MW) (Dehnen & Binney 1998; Skuljan et al. 1999; Famaey et al. 2005; Antoja et al. 2008). Historically, several overdensities in this velocity distribution have been identified and discussed (Pleiades, Hyades, Sirius). These moving groups, as they are usually referred to, can be related to the orbital resonances of the bar and spiral arms of the Galaxy (Kalnajs 1991; Dehnen 2000; Antoja et al. 2011; Fragkoudi et al. 2019; Monari et al. 2019b) and/or attributed to ongoing phase mixing related to external perturbations (Minchev et al. 2009; Gómez et al. 2012; Antoja et al. 2018; Ramos et al. 2018; Hunt et al. 2018b; Khanna et al. 2019; Laporte et al. 2019, 2020).

The latest releases of the *Gaia* mission (Gaia Collaboration et al. 2018a, 2021b) have provided a full 6D phase-space catalogue of 7.2 million stars, increasing the size and precision of any previous survey by several orders of magnitude. This has been a game-changer in many fields of astrophysics. In the SN, the new high resolution velocity distribution has revealed a complex substructure, with several thin arches never observed before (Gaia Collaboration et al. 2018b). When extending the study to the entire disc, large ridges appeared in the R-V_ϕ (respectively, Galactocentric radius and azimuthal velocity) diagram covering several kiloparsecs (Antoja et al. 2018; Kawata et al. 2018; Fragkoudi et al. 2019).

Orbits in a barred potential can be trapped into resonances (Weinberg 1994). Dehnen (2000) showed that in a short/fast bar scenario (i.e. $\Omega_b = 50\,\mathrm{kms^{-1}kpc^{-1}}$) the transition between two types of non-axisymmetric orbital families across the bar's Outer Lindblad resonance (OLR) can explain the bi-modality formed by *Hercules* and the rest of the velocity distribution in the solar neighbourhood if the Sun is placed just outside the OLR of the bar ($R_{\mathrm{OLR}} \approx 7.2\,\mathrm{kpc}$). This scenario was consistent with the gas dynamics measurements of the inner MW at the time. Later on, studies of star counts and kinematics of the inner MW suggested that the the bar might be longer and slower than previously thought (Portail et al. 2017). In this case, the OLR would be placed further out ($R_{\mathrm{OLR}} \approx 10.5\,\mathrm{kpc}$, maybe matching other groups such as the *Arch/Hat* instead of *Hercules*) and co-rotation (CR) would be closer to the SN ($R_{\mathrm{CR}} \approx 6\,\mathrm{kpc}$). Pérez-Villegas et al. (2017) and Monari et al. (2019b) then explained *Hercules* as the overdensity formed by the orbits trapped at the CR, librating around the Lagrangian points of a long/slow bar. This moving group created by CR seems to be less pronounced than the one produced by the OLR (Binney 2018; Hunt et al. 2018a). However, Hunt et al. (2018b) showed that the addition of spiral structure in combination with the CR might create a strong distinct Hercules, and Chiba et al. (2021) showed that a decelerating Galactic bar could enhance the occupation on resonances, being able to reproduce Hercules thorugh the CR resonance. This shows that the value of the pattern speed (Ω_b) of the MW bar as well as the exact link between substructures and resonances are still a matter of debate, and more observables are needed to obtain a final answer.

In this direction, Ramos et al. (2018, hereafter R18), used the wavelet transform (WT, Starck & Murtagh 2002; Chereul et al. 1999) to detect and characterize the kinematics of the moving groups along the disc. They matched the spatial evolution of the groups with the ridges in the R-V_ϕ plane. They claimed that some of the arches follow lines of constant energy at a given volume –which could be related to phase mixing processes (Minchev et al. 2009; Gómez et al. 2012)– and others follow lines of common angular momentum in the radial direction, as expected approximately in the case of resonant kinematic substructures (e.g., Quillen et al. 2018a). They also claimed that the observed changes in the azimuthal direction for the Hercules moving group are consistent with being produced by the OLR of a short/fast bar (Dehnen 2000; Fux 2001; Antoja et al. 2014). The long/slow paradigm is relatively recent and there have been few analyses on the azimuthal variations of a substructure caused by CR. Monari et al. (2019a) found that the Hercules angular momentum changes significantly with azimuth as they predicted analytically for the co-rotation resonance of an old long/slow bar. They showed that the only way to obtain a similar change in azimuth for an OLR origin of Hercules would be if orbits are still far from phase-mixed in the bar potential (bar perturbation younger than 2 Gyr; see also Trick et al. 2021).

The link between the moving groups across the neighbourhoods in R18 was made visually, using a scatter plot of two variables and a third one as colour. Therefore, the analysis of the moving groups link was restricted to three variables. Since V_R and V_ϕ are compulsory to select the moving groups, this limitation restricted the analysis to one dimension in space (either radial or azimuthal). The vertical direction was not explored.

The correlation between the position of the moving groups (overdensities in $V_R - V_\phi$) and the ridges (overdensities in $R - V_\phi$) indicate that both are projections of the same substructure in the 6D phase-space onto different planes. The positions of these kinematic substructures –moving groups– can be described as continuous manifolds in the 6D phase space, and the ridges and arches as specific projections of these manifolds. Our goal in this article is to extend the idea introduced in R18 by automatising the n-dimensional link of the moving groups to avoid the limitation of projecting the data. With this, we intend to move from a ridge-moving group paradigm to a manifold paradigm, were we sample the position of these manifolds in the $(R, \phi, Z, V_R, V_\phi)$ space for each moving group.

We present a novel methodology to detect these manifolds in a dataset. It is based on the execution of the WT in independent small volumes, and the relation of these local solutions in global substructures with an algorithm based on the Breadth-first search (BFS) algorithm from Graph Theory. With this methodology, we process the Gaia EDR3 6D data and detect the positions of the groups across the MW disc. We also sample the manifolds of two test particle simulations with a fast ($\Omega_b = 50\,\mathrm{kms^{-1}kpc^{-1}}$) and a slow ($\Omega_b = 30\,\mathrm{kms^{-1}kpc^{-1}}$) bar, both to test our methodology and to compare it to the data.

The Gaia DR3 (Brown 2019) catalogue will include a larger and updated sample of radial velocities (33 M of stars, `https://www.cosmos.esa.int/web/gaia/dr3`), which will cover a larger region of the MW disc and increase the resolution (number of stars and precision) in the already sampled part. This will provide finer observables to untangle the different contributions in the complex dynamics of the Galaxy. To exploit these data in its totality, new strategies must be developed (e.g. Contardo et al. 2022) to avoid the current limitations in the analysis, which the present article contributes to.

This paper is organized as follows. In Section 2, we describe the observational data that we used. In Section 3, we introduce the methodology we developed. In Section 4, we show the results of the application of the method to Gaia EDR3 data. In Section 5, we present and analyse the simulations. In Section 6, we compare the results from the data and the simulations, and with previous results in the literature. Finally, in Section 7 we list the main conclusions of this work.

2. Data and sample preprocessing

The Early release of Gaia DR3 consists of an updated and enlarged source list, with improved astrometry and photometry. Besides proper motions, about 7.2 million stars have radial velocity (RV) measurements in the Gaia DR2, most of which are transferred to EDR3 (Seabroke et al. 2021; Torra et al. 2021). For this section, we use a subset of these stars with photo-geometric distances from Bailer-Jones et al. (2021), derived from a probabilistic approach including colour and apparent magnitude information.

Distance is a critical parameter in the computation of the motion and position of the star in the 6D study of the MW, and a major source of uncertainty. This is why, in order to improve the quality of the sample, we additionally apply a cut in relative parallax error:

$$\left|\frac{\varpi}{\sigma_\varpi}\right| > 5. \quad (1)$$

The resulting sample contains 6 059 648 sources.

We use a Cylindrical Galactocentric coordinate system, fixing the reference at the Galactic Centre (GC) with the radial direction (R) pointing outwards from it, the azimuthal (ϕ) negative in the direction of rotation, and the vertical component (Z) positive towards the North Galactic Pole. To transform Gaia observables to positions and velocities in this reference frame, we take

the Sun to be at $R_\odot = 8.178$ kpc (Gravity Collaboration et al. 2019), $\phi_\odot = 0$ and $Z_\odot = 0.0208$ kpc (Bennett & Bovy 2019). For the solar motion, we use $U_\odot = 11.1, v_{circ} + V_\odot = 248.5, W_\odot = 7.25\,\mathrm{km\,s^{-1}}$ (Schönrich et al. 2010; Reid & Brunthaler 2020).

3. Method

The data described in the previous section contains the 6D variables of position (R, ϕ, Z) and velocity (V_R, V_ϕ, V_Z) of the stars. Inside small volumes –cuts in (R, ϕ, Z)–, the moving groups appear as well defined overdensities in the velocity distribution V_R-V_ϕ (R18), which are easy to detect. However, we know that at large spatial scales the position of the overdensities in the velocity space changes (ridges in R-V_ϕ). Therefore, if we use larger volumes to construct the velocity distribution the overdensities will blur and become undetectable.

In this section, we present the novel method that we developed to extract these large kinematic substructures from a dataset. It is divided into two steps; the execution of the WT in independent small volumes of the MW disc, and the relation of these local solutions in global substructures, with an algorithm based on the Breadth-first search (BFS) algorithm from Graph Theory (Moore 1959, descrived in Section 3.2).

3.1. Local Wavelet Transform

We partition the data in a dense grid of small volumes (from now, *pixels*) in the spatial coordinates. We construct it as follows:

- Radial direction (R_i): [5, 14] kpc in steps of 0.04 kpc, $R_{bin} = \pm 0.24$ kpc around each centre
- Azimuthal direction (ϕ_j): $[-34, 34]$ deg in steps of 0.8 deg, $\phi_{bin} = \pm 2.4$ deg around each centre
- Vertical direction (Z_k): $[-1, 1]$ kpc in steps of 0.08 kpc, $Z_{bin} = \pm 0.24$ kpc around each centre

which produce a dense grid of 2 700 000 pixels, with a maximum volume overlap between consecutive pixels of 83.3%.

For each pixel, we construct the velocity distribution (V_R, V_ϕ) diagram of the stars in it as a 2D histogram with bins of $1\,\mathrm{kms^{-1}}$ (see background histogram in Fig. 1). R18 showed that the overdensities form thin arches elongated around large ranges of V_R, with a small variation in V_ϕ. The use of 2D peak detection algorithms (as the one in R18) is sub-optimal for arch-like structure detection. When analysing regions with few observations, the search for peaks is translated into a very noisy determination of V_R, and uncontrollable correlations between V_R and V_ϕ (movement along the arch).

To avoid this, we slice each $V_R - V_\phi$ diagram in vertical columns (bins in V_R), and run a 1D WT in the V_ϕ histogram of each column:

- Radial velocity (V_R): $-100 - 100\,\mathrm{kms^{-1}}$ in steps of $10\,\mathrm{kms^{-1}}$, $V_{R\,bin} = \pm 15\,\mathrm{kms^{-1}}$ around each centre

Since we are detecting each part of the arch separately, we avoid the movement along the arch of the overdensities, breaking the degeneracy between V_R and V_ϕ in the detection. To detect the peaks, we use the algorithm developed in Du et al. (2006) implemented in `scipy` (Virtanen et al. 2020) as `find_peaks_cwt`. This method performs the 1D WT in a range of length scales. A peak is then selected if it is present in enough scales consecutively. In our execution, we use a range of scales of $[5, 10]\,\mathrm{kms^{-1}}$, with steps of $1\,\mathrm{kms^{-1}}$. We keep the peak if it is present in more than two scales consecutively. With this configuration of scales, we loose the thin resolution that we could extract in regions with a large number of sources, but we gain robustness in the detection of the large structures in poorly sampled regions. Since the scope of this work is the large-scale behaviour of the groups, we consider this approach to be better.

At the end of the execution, the peak p inherits the spatial position from the pixel, V_R from the position of the radial velocity bin, and V_ϕ from the result of the WT detection. Therefore, a peak has the coordinates

$$p = (R, \phi, Z, V_R, V_\phi)_p. \tag{2}$$

3.2. Breadth-first search (BFS) resolution with online interpolator

We have defined the pixels to have a large overlap among them (two adjacent pixels will share 83.3% of their volume). Therefore, a given substructure in consecutive pixels will have an almost identical shape.

For a pair of peaks from consecutive pixels, we consider them to be adjacent if they are in the same V_R bin and their distance in V_ϕ is smaller than $4\,\mathrm{kms^{-1}}$. In R18, the maximum slope found in a moving group is $33\,\mathrm{kms^{-1}kpc^{-1}}$. In our grid the step is 0.04 kpc, which translates in a maximum change of $\approx 1\,\mathrm{kms^{-1}}$ between adjacent pixels. This $4\,\mathrm{kms^{-1}}$ limit in the adjacency is a compromise between including very steep groups (about 4 times the one detected in R18) and reducing the number of adjacencies, which will determine the computational cost of the next step.

In some occasions, especially in poorly sampled regions, a peak from one pixel can be exactly in the middle of two peaks in the other pixel. In these cases, we do not consider any of them adjacent. With this consideration, two adjacent peaks are always strong candidates to belong to the same substructure.

This adjacency information constructs an enormous net of linked peaks. Ideally, substructures will be isolated subsets of peaks in this net. These are groups of peaks with no adjacencies to any peak outside their group.

In Graph Theory, these nets of linked points are called Graphs and the isolated groups are the connected components of a Graph. A very common algorithm to extract these connected components is the Breadth-first search (BFS) algorithm, which proceeds as follows:

1. Add (enqueue) the initial peak p to the queue[1] Q.
2. Select (dequeue) the top peak p_{top} of the queue Q.
3. Visit all the peaks p_{adj} adjacent to p_{top}. For each adjacent peak, if we have already visited it, ignore the peak. If it is the first time we see the peak, enqueue it.
4. If there are still peaks in the queue, return to step 2.
5. If the queue is empty, our connected component is the list of visited peaks.

Given an initial peak p_0, Algorithm 1 (see below) returns the entire substructure to whom it belongs. By repeating the process for all the non-matched peaks we can extract all the substructures.

This solution would be enough in an ideal case, but in practice undersampling and Poisson noise especially in regions far from the Sun produce confusion and jumps between structures that a straightforward BFS implementation can not filter out.

[1] A queue is a data structure similar to an array with limited access to the positions. One end is always used to insert data (enqueue) and the other is used to remove data (dequeue). Queue follows First-In-First-Out methodology, i.e., the data item stored first will be accessed first.

Algorithm 1 – Breadth-first search

queue Q
list V
add p_0 to V and enqueue in Q
while Q not empty **do**
  $p_{it} \leftarrow$ dequeue Q *(remove and assign)*
  for all p_{adj} adjacent to p_{it} **do**
    if p_{adj} not in V **then**
      add p_{adj} to V, enqueue in Q
    end if
  end for
end while
return V

Algorithm 3 – Breadth-first search with online interpolator

queue Q
list V
add p_0 to V and enqueue in Q
while Q not empty **do**
  $p_{it} \leftarrow$ dequeue Q *(remove and assign)*
  for all p_{adj} adjacent to p_{it} **do**
    if p_{adj} not in V and **is_consistent_with**(p_{adj}, V) **then**
      add p_{adj} to V, enqueue in Q
    end if
  end for
end while
return V

In order to avoid these jumps between structures, we include an extra step in the algorithm. While the BFS is running, the peaks already matched give us information about the structure. Therefore, in order to accept a new peak, we will require it to be consistent with the current structure.

Let us suppose we have a group V of already visited peaks (the current substructure we are extracting). To see if a peak p is consistent with this substructure we will select all the peaks in V in a small subset $S \subset V$ around p. With this local sample we can compute a linear fit

$$V_\phi \approx a_0 + a_1 R + a_2 \phi + a_3 Z \quad (3)$$

of the subset S around p and predict the expected V_ϕ of the substructure in a given position. This works under the assumption that the manifold that follows the substructure is derivable and we can compute its first order approximation locally.

This prediction is already absorbing the offset in the structure position produced by its slope in a certain direction. Therefore, the criteria in the acceptance of a new peak should be more strict than the one in the first adjacency step. Our limit in the resolution is the $1\,\mathrm{km s^{-1}}$ bin in the V_ϕ histogram, and we include an extra tolerance of $0.5\,\mathrm{km s^{-1}}$. If the distance between the peak azimuthal velocity $V_{\phi,p}$ (Eq. 2) and the prediction is smaller than $1.5\,\mathrm{km s^{-1}}$, we consider the peak to be consistent with the structure. We encapsulate this in the **is_consistent_with** function (Algorithm 2). We provide a summary of the final algorithm in pseudocode (Algorithm 3).

Algorithm 2 – is_consistent_with(p_{adj}, V)

$S = V(|R_{p_{adj}} - R_V| < R_{fit} \quad \&$
$\quad |\phi_{p_{adj}} - \phi_V| < \phi_{fit} \quad \&$
$\quad |Z_{p_{adj}} - Z_V| < Z_{fit})$
$f(R, \phi, Z) = V_\phi \leftarrow linear\_fit(S|_{p_{adj}})$
if $|f((R, \phi, Z)_{p_{adj}}) - V_{\phi, p_{adj}}| < d$ **then**
  return True
else
  return False
end if
$R_{fit} = 1\,\mathrm{kpc}$, $\phi_{fit} = 4\,\mathrm{deg}$, $Z_{fit} = 0.2\,\mathrm{kpc}$, and $d = 1.5\,\mathrm{km s^{-1}}$.

4. Results

Within the 3D grid the method extracted hundreds of structures, covering 2.5 to 6 kpc in R and 30 to 60 deg in ϕ. In R18 the arches in the solar neighbourhood and the radial direction were carefully characterized, and matched to the groups previously studied in the literature. We rely on this matching to associate the results of our methodology with the different groups and arches.

We end up with a sample of 99 structures, each one associated with one of the nine main moving groups: *Acturus*, *Bobylev*, *Hercules*, *Horn*, *Hyades*, *Sirius*, *Coma Berenices*, *Arch/Hat* (R18, references therein), and *AC* (see Anti-Centre newridge 1 in Gaia Collaboration et al. 2021a). Each structure traces the position of the moving group along the space at a given V_R. Therefore, each group of structures traces the manifold of the position of the moving groups in the $(R, \phi, Z, V_R, V_\phi)$ space. For each moving group, we select its largest structure as its representative. These representatives will be used in the following sections to study the behaviour of the groups in $R - \phi$ and $R - Z$ projections.

In Fig. 1, we show the selected groups in several neighbourhoods in the radial direction. In each arch we highlight its representative with a larger black border. As explained in Section 3.1, our goal in this work is to be able to perform this analysis in a large extent of the disc, so we tuned the detection parameters to obtain a robust detection of the main structures in noisy regions (see $R > 10\,\mathrm{kpc}$ in Fig. 1), and this required to use larger spatial bins. Because of this, the thin arches observed in the Gaia velocity distribution in the SN are slightly washed out.

The methodology links the structures in a given V_R, but does not provide the link of the arches in V_R-V_ϕ. The complex nature of the arches formed by the moving groups at different positions in the disc and the high level of noise result in a sub-optimal global link of the arches in the velocity distribution. Therefore, we only provide a tentative manual linking of the structures, based on the study of R18. In the rest of the paper we use this arch link as a qualitative tool in the analysis, but the main conclusions are based on the properties of the individual parts of the arches, which are determined by the described methodology.

This linking provides interesting results, different than in previous studies. For instance, the evident link of the *Arch/Hat* at $R = 9.4\,\mathrm{kpc}$ creates an asymmetric arch shape for this structure at the SN. This could be an artifact of the detection of *Arch/Hat* at $V_R > 60\,\mathrm{km s^{-1}}$ or a physical evidence of an unknown behaviour related to its origin. Notice that tagging the groups in the the SN and assuming that they keep united across the disc is a clear oversimplification. In the data, we have seen that *Sirius* is formed by two arches at SN but these arches merge in a single one at the outer parts of the disc (pannels $R = 8.16, 9.4\,\mathrm{kpc}$ in Fig. 1). The same happens for *Arch/Hat* at $R = 10.4\,\mathrm{kpc}$. In the simulation (Sect. 5), we observe the same behaviour for overdensities related to the Outer Linblad Resonance. So far, this simplification is useful for the discussion and comparison to the state of the art. Moreover, the lack of data far away from the SN does not allow a robust arch characterization. In future releases, an automatized

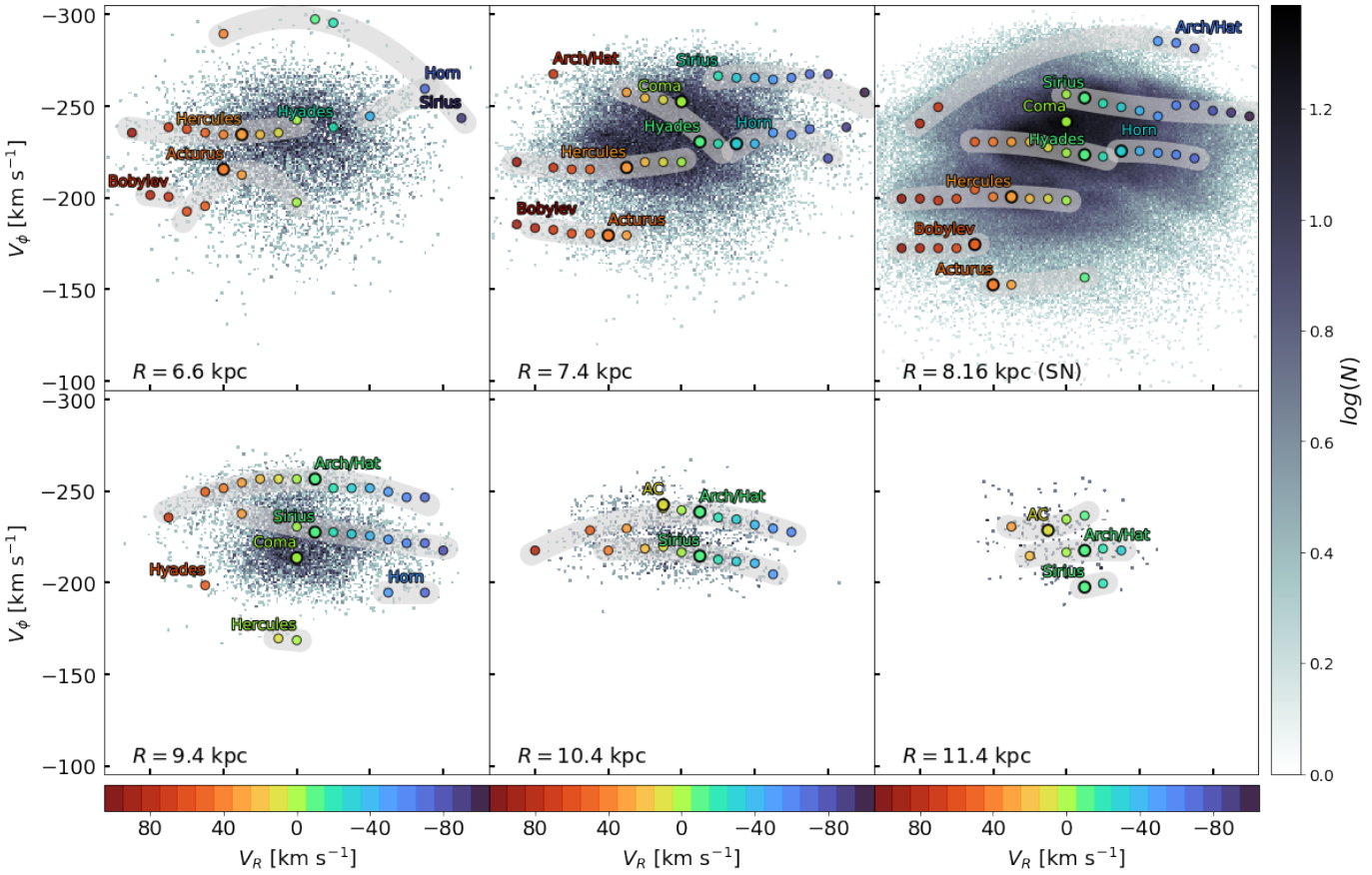

Fig. 1. Moving group detection in different neighbourhoods along the radial direction. For each moving group, we include a parabolic fitting of the substructures associated with each group in a thick grey line. Each moving group contains several structures, corresponding to different V_R bins. The largest structure in each group is used as its representative (dots with larger black contours and the moving group name on top). We can see two examples of bimodalities, which serve as evidences of the complex evolution of the arch morphology (*Sirius* at $R = 8.16$ kpc and *Arch/Hat* at $R = 10.4$ kpc).

arch detection will be needed to disentangle the complex orbit distribution.

4.1. Radial direction

The first evidence of large-scale substructure in the dynamics of the disc was the presence of ridges in the R-V_ϕ plane, directly related to the moving groups observed in the SN. Therefore, a first exercise we can do with the manifolds is to extract their subsets in the radial direction (i.e. $\phi = 0$ deg, $Z = 0$ kpc) and plot them in R-V_ϕ plane, colored by V_R (Fig. 2). In the top panel, we show the representative groups, tagged by their literature name. In the bottom panel, we show the rest of structures as beams of lines that define the morphology of the corresponding moving groups. As expected, when tracing the different moving groups along R we observe diagonal lines in R-V_ϕ, matching the already known ridges.

Comparing with R18, we detect the same moving groups but we manage to extend their detection several kiloparsecs. The results in the inner and outer part of the disc ($R < 6.5$ kpc and $R > 10$ kpc) are noisy due to Poisson noise. The Gaia DR3 release will improve the detection of groups in these regions, but even if we exclude this part the groups extend far beyond the range seen in other studies (see Fig. 6 in R18). This extension of the structures is due to both a major improvement of the methodology and the use of the updated astrometric Gaia EDR3 data. The lower error in proper motion and parallax increases the concentration of the moving groups in the undersampled regions.

In Fig. 2, we can observe how the slope of the lines in radius is not constant across the different groups. In the top plot, groups like *Acturus*, *Hercules*, and *Arch/Hat* present slopes significantly steeper than *Sirius* and *AC*. However, this slope is not a common characteristic in all the parts of the arch of a group. For instance, in the bottom plot we can see that *Acturus* is very steep at $V_R = 30-40$ kms^{-1} (orange lines) and flattens for the negative part of the arch ($V_R = -20$ kms^{-1}, blue lines). We observe that secondary peaks have very different azimuthal and radial velocities when they start to show up at inner radius, but end up having very similar azimuthal velocity at larger radius. This corresponds to a flattening of the arches in the velocity distribution as R increases. This is not observed in the simulations (Sect. 5), and could be an effect of the centroid of the distribution dominating in case of undersampling in these regions.

As for the global shape of the lines, the resonant effects of the bar and spiral arms are expected to create kinematic substructures that, from epicyclic approximation analysis of the first order effects, have an almost constant vertical angular momentum $L_Z = RV_\phi$ (Sellwood 2010; Quillen et al. 2018b). Thus, if the moving groups have a bar resonance origin, their azimuthal velocities would naively be expected to follow lines $\propto R^{-1}$ (dashed grey lines in Fig. 2 top panel). In Ramos et al. (2018) (their Fig. 6), this trend is observed for *Hercules* and *Hyades*. When extending the analysis to a larger region, we find that the groups

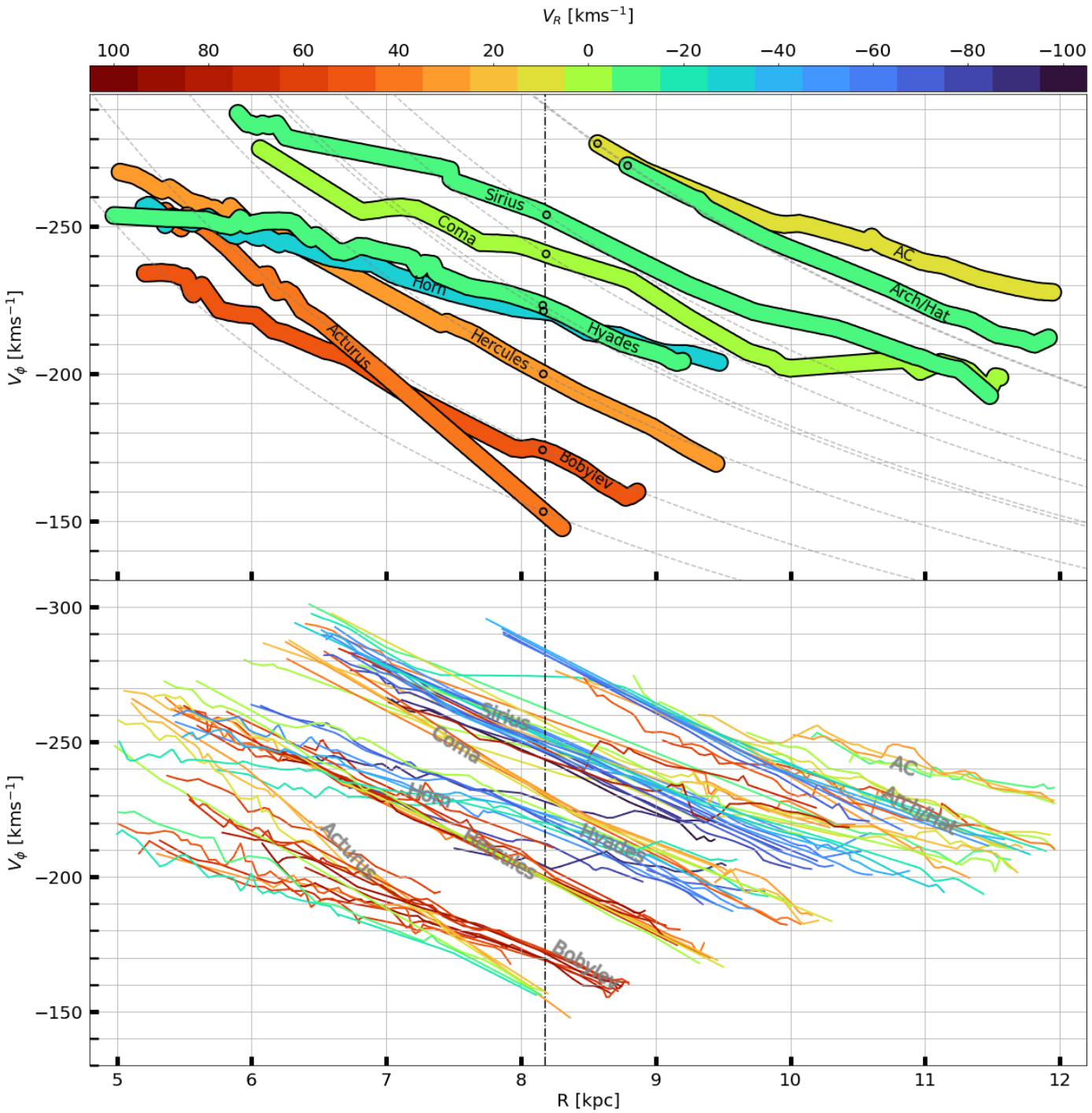

Fig. 2. Azimuthal velocity of the kinematic substructures in the radial direction, $\phi = 0°$, $Z = 0$ kpc, as a function of the radius, and coloured by their radial velocity. The dashed grey lines correspond to constant angular momentum lines, crossing the moving groups at solar radius. Top: Structures corresponding to the main peak of a moving group, tagged with the name in literature. Bottom: Secondary peaks of the moving groups. The usual way to observe this projection is using the number of stars or the mean V_R in each bin (see Fig. 1 in Fragkoudi et al. 2019). Using our methodology we can observe the skeleton of the distribution and its complexity. For instance, the slope of the moving groups at different V_R can be very different and the groups cross each other or share close regions in the diagram. In addition, the extension of the range of exploration shows that the moving group deviate from the constant vertical angular momentum predicted for small epicyclic amplitudes.

deviate from the lines of constant angular momentum. Not even *Hercules* and *Hyades* are well approximated globally by this $V_\phi \propto R^{-1}$ trend. We come back to this in Sect. 6.

The ridges are usually studied in R-V_ϕ diagrams colored by density or mean V_R (see Fig. 1 in Fragkoudi et al. 2019). By doing these projections, the complexity of the moving groups (arch curvature, bi-modalities, arch disruption, etc) is lost, offering only a partial understanding of the sample. With our methodology we can now visualize this complexity in a single plot. For instance, we can observe how the V_R-V_ϕ arch corresponding to the *Acturus* moving group is a horizontal arch at $R = 8$ kpc (structures with different V_R and common V_ϕ) but it curves as

we move to inner radius (the different structures fan out). This spreading clearly depends on the V_R, which is a sign of a curved arch. Mixed with *Acturus*, we are able to observe the morphology of *Bobylev* at $V_R > 50\,\mathrm{kms}^{-1}$. In the previously mentioned projections, the visualization of both structures is not possible, since the mean V_R blends both contributions.

Beyond the detection and characterization of ridges in the radial direction, the main contribution of our method is the blind search of these kinematic structures in the three spatial dimensions at the same time. Next we focus on the representative of each moving groups and study their kinematics in the 3D space, azimuth submanifold ($Z = 0\,\mathrm{kpc}$) in Sect. 4.2, and vertical submanifold ($\phi = 0\,\mathrm{deg}$) in Sect. 4.3.

4.2. Azimuth submanifold

We first do a cut in the structures around $Z = 0\,\mathrm{kpc}$ ($|Z| < 0.2\,\mathrm{kpc}$) to observe the behaviour of the different moving groups as a function of R and ϕ. We obtain surfaces covering up to ±25 deg (≈ 3.5 kpc at Solar Radius). This is the first time that the moving groups are traced along the $Z = 0\,\mathrm{kpc}$ plane with this completeness.

In Figure 3, apart from the already studied decrease of V_ϕ with R, we can see how *Acturus*, *Bobylev*, and *Hercules* moving groups present a slope in the azimuthal velocity along azimuth, whereas *Horn*, *Sirius* and *Arch/Hat* moving groups present an axisymmetrical behaviour of the azimuthal velocity along azimuth, as expected in an axisymmetric potential.

It is interesting to quantify the variation of V_ϕ with ϕ for the structures. We evaluate this slope[2] $\partial V_\phi/\partial\phi$ at a given R by restricting the structure to this R value and doing a linear fitting of the surfaces in $\phi - V_\phi$. We compute the slope in the radius that minimizes the error in the fitting. The resulting values are: $-0.40\,\mathrm{kms}^{-1}\mathrm{deg}^{-1}$ at $R = 7\,\mathrm{kpc}$ for *Acturus*, $-0.63\,\mathrm{kms}^{-1}\mathrm{deg}^{-1}$ at $R = 7\,\mathrm{kpc}$ for *Bobylev*, $-0.50\,\mathrm{kms}^{-1}\mathrm{deg}^{-1}$ at $R = 8\,\mathrm{kpc}$ for *Hercules*, $-0.04\,\mathrm{kms}^{-1}\mathrm{deg}^{-1}$ at $R = 10\,\mathrm{kpc}$ for *Sirius*, and $-0.01\,\mathrm{kms}^{-1}\mathrm{deg}^{-1}$ at $R = 10\,\mathrm{kpc}$ for *Arch*.

In Monari et al. (2019a) they study the mean angular momentum evolution in ϕ for *Hercules* in an analytical model. They predict that, in case of a co-rotation origin, the angular momentum J_ϕ of *Hercules* at the solar radius must significantly decrease with increasing azimuth. Their model predicts the slope to be around $-8\,\mathrm{kms}^{-1}\mathrm{kpc\,deg}^{-1}$, and they observe a similar trend in Gaia DR2 data. Our equivalent value in angular momentum would be $-4\,\mathrm{kms}^{-1}\mathrm{kpc\,deg}^{-1}$, which is smaller than the predicted value.

In some parts of the disc, the mean azimuthal velocity in the plane for the total 6D sample decreases with increasing azimuth at a constant radius (see Fig. 10 in Gaia Collaboration et al. 2018b, $R = 8 - 10\,\mathrm{kpc}$). This is the behaviour that we observe for *Acturus*, *Bobylev*, and *Hercules*. It would be worth investigating the relative contribution of each moving group to the total sample to understand the relation between these individual groups and the total average motion but we refer this to a future study.

4.3. Vertical submanifold

We also study the projection in the $R - Z$ plane ($|\phi| < 10\,\mathrm{deg}$, see Fig. 4). In all the structures but *Coma Berenices* (see below), we observe decreasing $|V_\phi|$ values for increasing $|Z|$. In addition, *Acturus*, *Bobylev*, and *Hercules* –the same structures that show steeper slope in azimuth– present a clear symmetry around $Z = 0\,\mathrm{kpc}$. *Arch* is also very simmetric in Z. In opposition, *Horn*, *Hyades*, and *Sirius* present an steeper decrease in

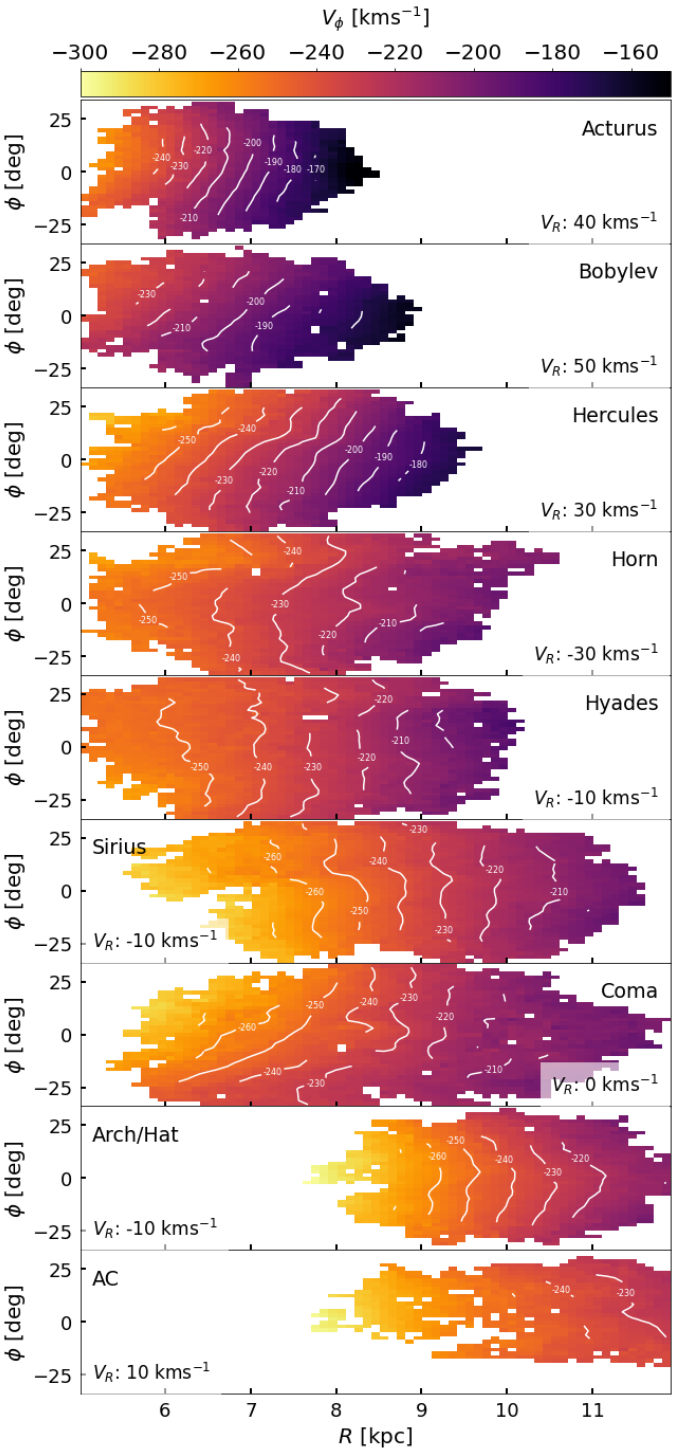

Fig. 3. Mean azimuthal velocity of the representative groups in the $R-\phi$ projection, for $|Z| < 0.2\,\mathrm{kpc}$. In white, the contours of regions with the same velocity are shown for clarity. *Acturus*, *Bobylev*, and *Hercules* moving groups present a constant slope in the variation of azimuthal velocity along azimuth, whereas *Horn*, *Sirius* and *Arch/Hat* moving groups present an axisymmetrical behaviour of the azimuthal velocity along azimuth.

[2] Note that in our reference system a negative $\partial V_\phi/\partial\phi$ slope corresponds to an increase of $|V_\phi|$ with ϕ (a moving group with negative $\partial V_\phi/\partial\phi$ moves upwards in the velocity distribution with ϕ).

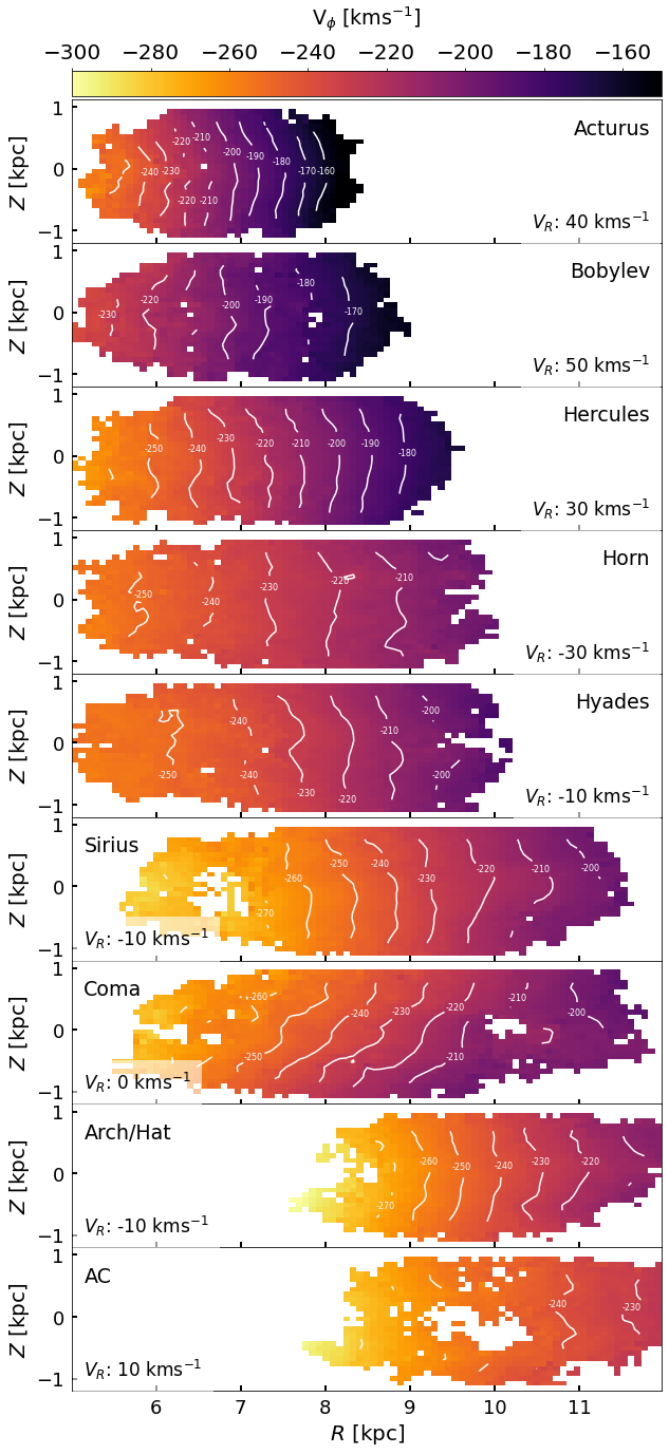

Fig. 4. Mean azimuthal velocity of the groups in the $R-Z$ projection, for $|\phi| < 10$ deg. In white, the contours of regions with the same velocity are shown for clarity. *Coma Berenices* clearly presents an increasing $|V_\phi|$ with Z, and thus, strong vertical asymmetry. We measure a constant vertical slope of $\partial V_\phi/\partial Z = -15\,\mathrm{kms^{-1}kpc^{-1}}$. The rest of structures show vertical symmetry.

$|V_\phi|$ for $Z > 0$ kpc with respect to the other moving groups, and a more constant value for $Z < 0$ kpc. Finally, *AC* has not enough signal at this point to analyse it properly.

Coma Berenices clearly presents an increasing $|V_\phi|$ with Z, and thus, strong vertical asymmetry. We note that outside the range of $R = [7, 10]$ kpc, this moving group shows a change of behaviour in all the spatial projections (Figs. 2, 3, 4) possibly because our methodology is linking it to other close structures. Therefore, focusing only on the $[7, 10]$ kpc, range, we measure a constant vertical slope of $\partial V_\phi/\partial Z = -15\,\mathrm{kms^{-1}kpc^{-1}}$, clearly different to the other groups and predictions from models with vertical symmetry.

It would be interesting to obtain a measurement of the vertical curvature of the moving groups at each radius, as done in the previous section with the slope in azimuth and with the vertical slope in *Coma Berenices*. With noisy data, each order of derivatives increases its uncertainty and the measurements we obtained were not significant enough. In the future, with better data and/or a robust analytical model to fit the curvature at all radius in the same time, this measurement could be produced.

5. Simulations

In this section we apply the same methodology to simulations. This has two main goals: evaluating the performance of our method in a case where there are no selection effects, and allowing a comparison of the data to a model where a particular and known perturbation is present. In our case, we used a series of test particle simulations with 60M particles. The initial conditions and the Galactic potential are described in Romero-Gómez et al. (2015). In particular, the disc has a local radial velocity dispersion of $\sigma_{V_R} = 30.3\,\mathrm{kms^{-1}}$ at the radius of 8.5 kpc. We integrate the initial conditions, first, in the axisymemtric potential of Allen & Santillan (1991) for 10 Gyr, and, secondly, we introduce the Galactic bar potential adiabatically during 4 bar rotations (2.46 Gyr for the slow bar and 1.47 Gyr for the fast bar), to finally integrate another 4 bar rotations. The Galactic bar consists of the superposition of two aligned Ferrers ellipsoids (Ferrers 1877), one modelling the triaxial bulge with semi-major axis of 3.13 kpc and the second modelling the long thin bar with semi-major axis of 4.5 kpc. We use two simulations, where the bar rotates as a rigid body with a constant pattern speed of 30 and 50 $\mathrm{kms\,kpc^{-1}}$. For the slow bar, the CR is located at 7.3 kpc and the OLR at 12.2 kpc. For the fast bar, the CR is located at 4.3 kpc and the OLR at 7.6 kpc. We use the final snapshot of the simulations, and assume that the bar is 30 deg in azimuth with respect to the Sun in the direction of rotation, close to the estimations for the MW (Bland-Hawthorn & Gerhard 2016, references therein).

In these final snapshots, we execute the methodology described in Section 3 and obtain an optimal detection of the moving groups in a large range of the sample. These robust results, matching the predictions from previous works, validate the performance of our methodology in a known dataset. However, we find some substructures related to the centroid of the velocity distribution whose changes with azimuth, radius and height are mostly related to the rotation curve of the model. In this section we only show the substructure related with bar resonances and ignore the rest of groups extracted by the methodology.

The selected moving groups are shown in the V_R-V_ϕ projection in Fig. 5 (same as done in Fig. 1 for the real data). In the simulation, the moving groups also show arches in this projection, which we are able to detect at several radii. Again, we can show the groups projected in the radial direction, (Fig. 6, analog to Fig. 2). In Figs. 5 and 6, the top panels show the structures of the fast bar model (depicting the effects of the *OLR* and *1:1* resonance). The bottom panels of the figures show the structures of the slow bar model (only the effects of the *OLR* appear). In the following sections, we analyse the fast bar model (Sect. 5.1) and the slow bar model (Sect. 5.2) in detail.

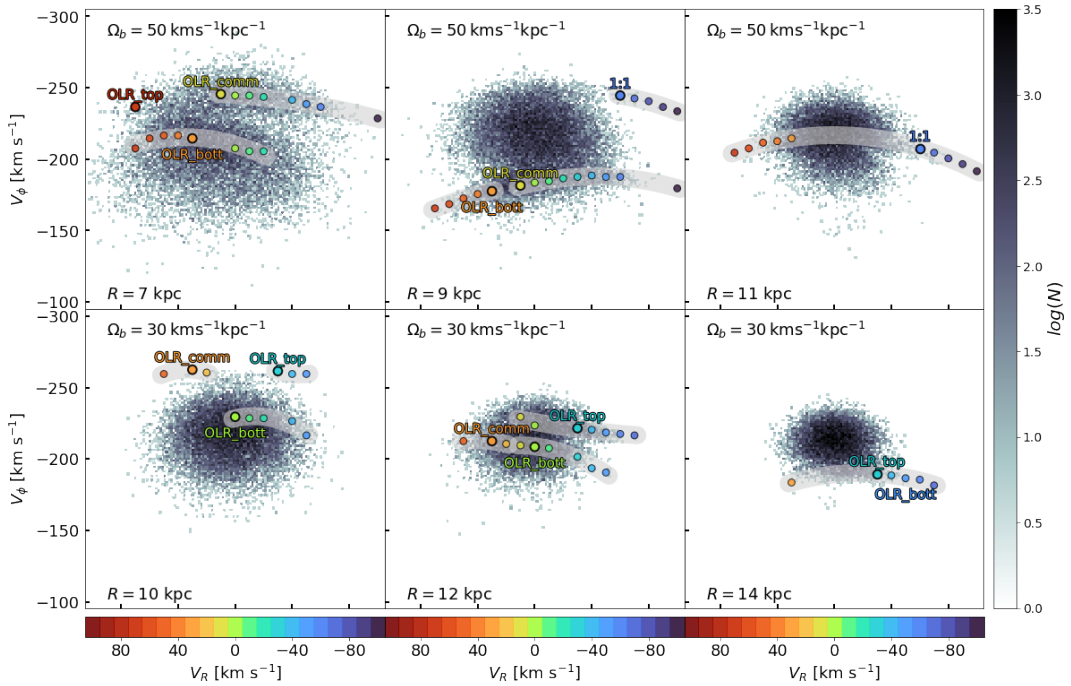

Fig. 5. Moving group detection in different neighbourhoods along the radial direction in the simulations, analog to Fig. 1. Top row: fast bar model. Bottom row: slow bar model.

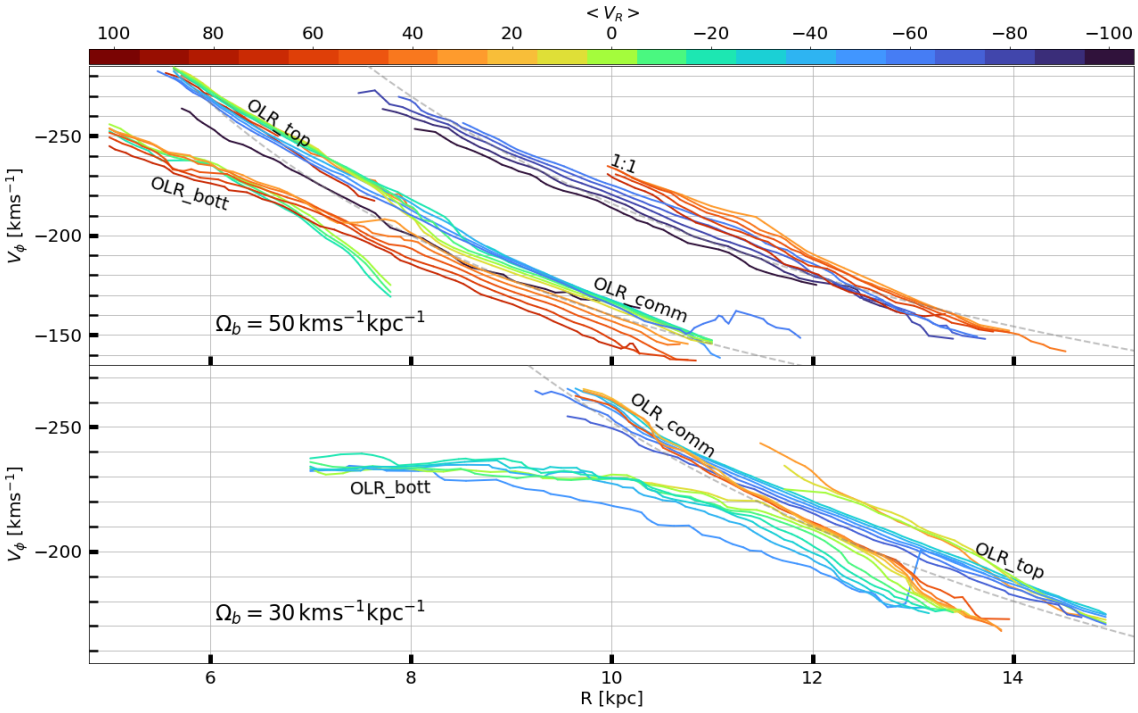

Fig. 6. Azimuthal velocity of the kinematic substructures in the radial direction ($\phi = 0^o$, $Z = 0$ kpc) for the test particle simulations, as a function of the radius, and coloured by their radial velocity. We include dashed grey lines corresponding to constant angular momentum lines as a guide. Top: Structures for the fast bar model. Bottom: Structures for the slow bar model. In the fast bar model, we are able to detect substructures related to the OLR and the 1 : 1 resonance, in the slow bar we only detect structures related with the OLR. See also Fig. B.1 for the mean radial velocity histogram. With our methodology, we are able to show the complex morphology of the arches in a single image.

As explained in the introduction, a fast bar model places *Hercules* near the OLR of the bar. In this model, *Arch/Hat* could be explained as the 1:1 resonance. Instead, the slow bar model places *Hercules* in the CR of the bar and *Arch/Hat* in the OLR. Therefore, in this article we refer as Hercules-like to structures in the simulation which can be related to *Hercules* in the data (i.e. generated by OLR for the fast bar model and by CR for the slow bar model), and Arch/Hat-like as the structures which can be related to the *Arch/hat* (i.e. induced by the 1:1 for the fast bar model and by the OLR for the slow bar model).

In Fig. 6, it is clear that the global position of the overdensities is not following exactly the lines of constant angular momentum predicted for small epicyclic amplitudes ($V_\phi \propto R^{-1}$). In the radial direction, the curvature of the *OLR_bott* structures is opposite in the two models. In addition, the fact that the structures merge at some radius is a clear evidence that they follow a trend different from $\propto R^{-1}$. The first order prediction for resonances is suboptimal for V_ϕ values far from the circular velocity. In Fig. 6, we observe how the radial slope of the structures differs more from the prediction at small and large V_ϕ values.

5.1. Fast bar model

In the fast rotating bar simulation ($\Omega_b = 50\,\mathrm{kms^{-1}kpc^{-1}}$), we are able to detect substructures related to the OLR and the 1:1 resonance with our methodology. As expected, both structures present an arch shape in the V_R-V_ϕ diagram (Fig. 5, top). The complete sampling and the simplicity of the simulation allows us to trace these arches unequivocally and observe their morphology in ranges up to 6 kpc in the radial and azimuthal directions, characterizing with strong robustness not only their position in the velocity space but the trend of the central and outer part of the arch separately. Note that the simulation has been integrated for 4 bar rotations, which places this model in the regime of a *young* fast bar, as defined in Monari et al. (2019a).

In the top part of Fig. 6, the bi-modality of the OLR and the 1:1 resonance are clearly observed. For the OLR, at $R < 7$ kpc we observe an Hercules-like arch (*OLR_bott*), extending to a maximum V_R of 40 $\mathrm{kms^{-1}}$ (orange line on top). In this same region, we also observe a symmetric arch on top of the distribution tagged as *OLR_top*, with a maximum in $V_R = 0\,\mathrm{kms^{-1}}$ (green line on top). At R between 7 and 8 kpc, the V_R-negative part of the bottom arch (V_R around $-10\,\mathrm{kms^{-1}}$) continues to decrease in $|V_\phi|$ and the positive part of the arch ($V_R > 20\,\mathrm{kms^{-1}}$) merges with the top arch (*OLT_top*) to form a unique structure covering the whole radial velocity range. This unique arch, *OLR_comm*, has its maximum at $V_R = -40\,\mathrm{kms^{-1}}$ (blue line on top). This arch configurations at $R = 7, 9$, and 11 kpc can also be seen in the top row of Fig. 5.

The signature of the *1:1* resonance (Arch/Hat-like structure) is less prominent than in the case of the *OLR*. In Fig. 5 (top row, $R = 11$ kpc), we observe a bi-modality in the histogram, with the upper part of the distribution being more prominent at negative V_R values and the lower part more prominent in the positive V_R range. In the R-V_ϕ diagram (Fig. 6, top panel) we see that at inner radius we mostly detect negative V_R and, at the outer parts, mostly positive V_R, giving more evidences of this bi-modality. Due to the small prominence of the resonance, we are not able to detect it when it is located in the centre of the distribution.

As we did with the real data, we exploit the 3D extent of the structures and show their trends in the azimuth submanifold. In Fig. 7 we show the $R-\phi$ projection of the azimuthal velocity for different parts of the arches (analog to Fig. 3). The black lines in these panels show the azimuthal slope of V_ϕ in each radius (right vertical axes).

The *OLR_comm* structures present a discontinuity around $R = 8$ kpc. In Fig. 6, this can be seen as the sudden drop in V_ϕ in the green-turquoise lines at $R \sim 8$ kpc ($V_R = -20, -10, 0\,\mathrm{km\,s^{-1}}$). A similar discontinuity is present in two panels of the *OLR_bott* structure in Fig. 7. The peak detection algorithm guarantees a minimum distance between peaks for robustness. Therefore, when two arches merge, it stops detecting one of them a while before the merge. Even with this, a few spurious detection can act as a bridge for the algorithm and and make it join both structures. Since the arches are merging, the algorithm described in Sect. 3.2 (Alg. 3) detects a continuity and the structures are detected together.

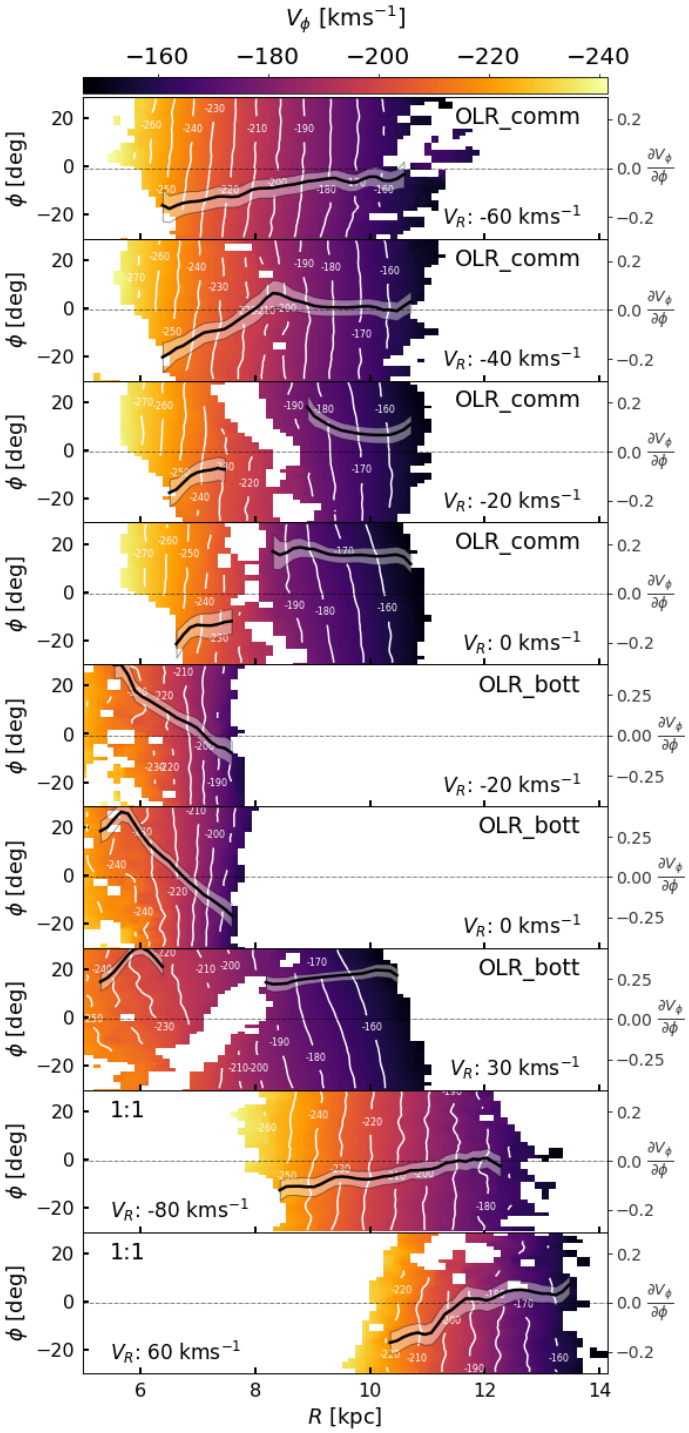

Fig. 7. Fast bar model. Mean azimuthal velocity of a selection of groups in the $R-\phi$ projection, for $|Z| < 0.5$ kpc. In white, the contours of regions with the same velocity are shown for clarity. In black, the slope of the linear fitting (ϕ, V_ϕ) is shown for every R column, in units of [$\mathrm{kms^{-1}deg^{-1}}$]. The 3σ error of the slope is shown in a translucent region around the line.

When looking at Fig. 7, it is important to remember that we are studying a *young* fast bar, which is known to introduce azimuth correlations, specially around the OLR (see Fig. A1 in

Trick et al. 2021). For most of the structures, we see an azimuth slope of V_ϕ that depends on radius. Interestingly, some structures have negative $\partial V_\phi/\partial\phi$, such as *Hercules* in the real data, and others have a positive slope. We observe three main structures with different patterns:

- Rows 1-4, and 7. Upper part of the OLR bimodality. Before crossing the rotation curve ($R \approx 8$ kpc), the $\partial V_\phi/\partial\phi$ slope of the structure is constant along all the V_R values. For $R > 8$ kpc, a correlation appears between $\partial V_\phi/\partial\phi$ and V_R. This is a sign that the *OLR_comm* arch shown in Fig. 5 (top row, $R = 9$ kpc) is moving to negative V_R values in the V_R-V_ϕ diagram as ϕ increases (when V_R is more positive, its $|V_\phi|$ decreases faster with ϕ).
- Rows 5, 6, and 7 ($R < 8$ kpc). Hercules-like part of the distribution. The slope in azimuth decreases as R increases. The contour lines merge when approaching the bar's long axis ($\phi_b = -30$ deg).
- Rows 8 and 9. Arch/Hat-like part of the distribution. The slope in azimuth is constant along the different detected parts of the arch, and tends to flatten for increasing R values.

5.2. Slow bar model

In the slow rotating bar simulation ($\Omega_b = 30\,\mathrm{kms^{-1}kpc^{-1}}$), we are able to detect the Arch/Hat-like overdensity caused by the OLR along a large range of radius, covering up to 6 kpc (Figs. 5 and 6, bottom panels). In the radial direction, we observe three different structures related with the OLR. Two of them have negative V_R and the other in the positive V_R. The negative V_R structures (*OLR_top* and *OLR_bott*) present a clear bi-modality in V_ϕ. In the V_R-V_ϕ diagram (Fig. 5, bottom), the *OLR_top* forms a flat arch and the *OLR_bott* forms a curved arch. In the positive V_R regime (orange-red lines), we observe one single structure (*OLR_comm*) compatible with *OLR_top* at $R = 10$ to 11 kpc which continues to decrease its azimuthal velocity with R in a constant slope and merges *OLR_bott* from $R = 12$ kpc to the outer parts of the disc.

Again, we can exploit the 3D extension of the manifolds to study how these groups are evolving in the $R-\phi$ projection. In Fig. 8 (analog to Fig. 7, but for the slow bar model) we observe two main structures, corresponding to the different parts of the OLR bi-modality (whose upper part corresponds now to the Arch-like group):

- Rows 1-3. Top part of the OLR bi-modality. It presents a constant slope in azimuth ($\partial V_\phi/\partial\phi = -0.1\,\mathrm{kms^{-1}deg^{-1}}$ at $R = 12$ kpc), flattening as R increases, similar to the Arch/Hat-like observed in Fig. 7 for the fast bar.
- Rows 4-7. Bottom part of the bi-modality. The slope is less constant, and we observe the same decrease in R as in the Hercules-like part of the fast bar model.

We do not detect overdensities caused by CR. In general, the expected Hercules-like moving group caused by CR is less prominent than when formed by the OLR (Binney 2018; Hunt et al. 2018a), especially if higher order modes are missing from the bar model. Also, if the velocity dispersion of the disc is too large in this region we could have less trapping and less resolution. Another explanation could be that the length of the bar in our models does not favour CR trapping. In the future, we aim to perform the same analysis with other models to analyse this effect (e.g. Sormani et al. 2022).

In Fig. B.1, we show the V_ϕ-R projection colored by mean V_R. In that figure we observe a very faint red overdensity in the CR region, but much weaker compared to the rest of the detected resonances in the fast and the slow bar models.

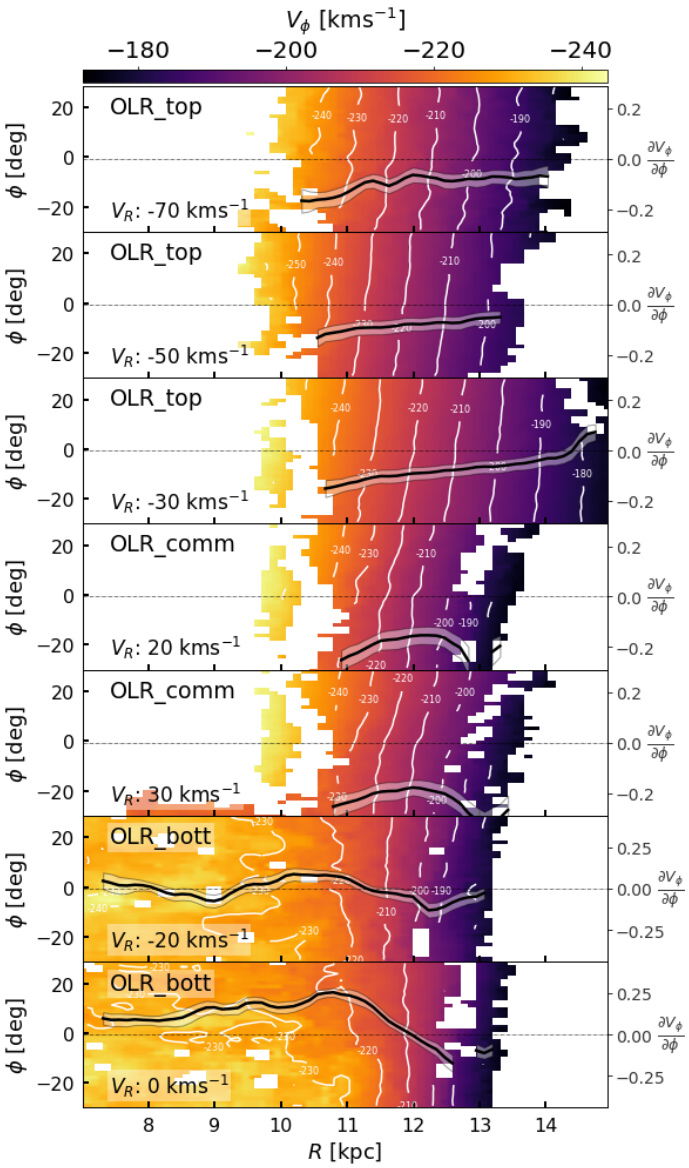

Fig. 8. Slow bar model. Mean azimuthal velocity of a selection of groups in the $R-\phi$ projection, for $|Z| < 0.5$ kpc, analog to Fig. 7. In this simulation, the shape of the arches is maintained along ϕ (same slope for all V_R values), with a constant displacement to bigger $|V_\phi|$ as ϕ increases.

6. Discussion

Simulations which contain only a bar perturber offer us the possibility to characterize its effects in a robust way. With it, we can then compare the manifolds extracted from the simulation with the ones seen in the data. As explained in the introduction, one of our goals with the characterization of the manifolds is to search for kinematic observables that distinguish resonances from short/fast or long/slow bars.

Radial direction. First, we focus on the slope, shape, and evolution of the moving groups in the data and the simulation along the radial direction (Figs. 2 and 6).

The global gradient of the structures in the radial direction deviates from the naive first order prediction for resonances (curves following $V_\phi \propto R^{-1}$) in the data and the simulations, as expected in more realistic cases, even if they have a resonance origin. In the simulations, we see that the lines are less curved than the simple prediction and some parts of the *OLR_bott* have even the opposite curvature. This is also observed in the data, where all the moving groups are less steep in the inner parts of the disc than the prediction, and *Hercules* and *Acturus* present the same opposite curvature pattern as the *OLR_bott*.

We see that, in the V_ϕ-R projection colored by mean V_R of the slow bar scenario of our simulations (Fig. B.1) the corotation overdensity is not significant enough. This has been already discussed in the introduction and in the previous section, and could be related to the specificities of the model considered here. In the fast bar scenario an Hercules-like structure is formed at $R = [6, 8]$ kpc, which shows an arch shape with a maximum in $V_R = 40\,\mathrm{kms}^{-1}$ (Fig. 5, top left panel), coherent with the *Hercules* moving group in the data. In this same radial region the top part of the OLR forms an arch in negative V_R, which can be related to *Horn*. Finally, from $R = 8$ kpc towards the outer parts of the disc, the OLR forms a single arch with a maximum in $V_R = -20\,\mathrm{kms}^{-1}$. A similar arch, present at all the radial velocities, was already observed in the models by Bovy (2010). In the data this region ($R > 9$ kpc, $V_\phi < -170\,\mathrm{kms}^{-1}$) contains very few stars and we did not detect any group there.

The other feature commonly associated with bar resonances is the *Arch/Hat* moving group. For a fast bar, it can be explained by the 1:1 resonance trapping region, and for a slow bar it matches the position of the OLR. In the data, the number of stars with $R > 10$ kpc is low. Therefore, the quality of the shape characterization of *Arch/Hat* moving group is poor. Even so, in the panel $R = 10.4$ kpc of Fig. 1 our method finds a tentative arch split around $V_R = 10\,\mathrm{kms}^{-1}$. This would match the split we detect between the *OLR_comm* and *OLR_top* structures in the slow bar model (Fig. 6, bottom panel at $R = 11$ kpc). In the fast bar simulation, the prominence of the 1:1 resonance is low and we can only detect it in regions far from the centroid of the distribution. Even with this limited detection, we do not observe a bi-modality in the negative V_R region, which would be a way to discriminate between resonances.

Azimuth submanifold. In both simulation models, for the Arch/Hat-like moving groups we observe a constant positive slope of $|V_\phi|$ in azimuth which tends to flatten (get closer to $0\,\mathrm{kms}^{-1}\mathrm{deg}^{-1}$) as R increases. In these Arch/Hat-like groups, the slope of the azimuthal velocity in azimuth does not depend on V_R (Figs. 7 and 8). In the data (Fig. 3), the *Arch/Hat* group is very noisy. Therefore, as discussed in the previous paragraph it is still complicated to use the *Arch/Hat* velocities for a final relation to a specific resonance.

In Fig. 7, we can observe the different parts of the OLR resonance in the fast bar. The Hercules-like overdensity ($R = [6, 8]$ kpc) shows a constant positive slope of $|V_\phi|$ in azimuth common along all V_R. In opposition, the trapping region of the resonance *OLR_comm* has a slope which depends on the V_R. This can be interpreted as the arch moving along V_R in the V_R-V_ϕ diagram when moving in azimuth, which is observed at the OLR in other simulations of a young bar far from phase-mixed (Dehnen 2000; Bovy 2010; Trick et al. 2021). Since we have the complete information of the moving groups in the data, we can reproduce the same analysis of the moving group slope at different V_R for some moving groups in the data. In Figures A.1 and A.2, we show this slope for *Hercules* and *Hyades*, respectively. We do not observe this dependence in V_R for any of the groups. In the velocity distribution, this can be observed as the moving group arches increasing their $|V_\phi|$ along azimuth, but no displacement along V_R.

Vertical submanifold. For the resonces of the bar, the vertical displacement of V_ϕ should be dominated to first order by the vertical potential of the Galaxy (Al Kazwini et al. 2022). In our results, the vertical curvature of all the moving groups (except for *Coma Berenices*) at a common radius is very similar, thus matching the analytical prediction. This means that this data is a good candidate to constrain the 3D structure of the potential. To second order, we could try to distinguish different curvatures of different resonances. In Al Kazwini et al. (2022), the displacement of the resonances at $Z = 1$ kpc with respect to the galactic plane is measured to be $8\,\mathrm{kms}^{-1}\mathrm{kpc}^{-1}$ for the corotation, $6\,\mathrm{kms}^{-1}\mathrm{kpc}^{-1}$ for the OLR, and $4\,\mathrm{kms}^{-1}\mathrm{kpc}^{-1}$ for the 1:1 resonance. Our maximum resolution, given by the V_ϕ histogram at each pixel, is $1\,\mathrm{kms}^{-1}\mathrm{kpc}^{-1}$. Therefore, disentangling which resonances create each moving group with the vertical information is beyond our current capabilities.

In the vertical behaviour of the moving groups, a clear outlier is *Coma Berenices*. In Quillen et al. (2018b) (also Monari et al. 2018; Laporte et al. 2019), the *Coma Berenices* moving group is observed to be present only at negative galactic latitudes, showing evidence for incomplete vertical phase-mixing. With the new EDR3 data and our methodology, we are able to detect the group in a larger extension and at positive and negative galactic latitudes but it does show a clear vertical asymmetry in its azimuthal velocity. We measure a constant vertical slope of $\partial V_\phi / \partial Z = -15\,\mathrm{kms}^{-1}\mathrm{kpc}^{-1}$. In the plots of a phase spiral colored by V_ϕ (Antoja et al. 2018), it is seen that there must be a correlation between Z and V_ϕ (higher $|V_\phi|$ values at positive Z). This slope in *Coma Berenices* could be a projection of this correlation.

7. Conclusions

We have sampled, with Gaia EDR3 6D data, the manifolds tracing the main moving groups in the solar neighbourhood along the $(R, \phi, Z, V_R, V_\phi)$ space, in an automatic way. We have revealed the skeleton of the velocity distribution in a multidimensional space that we can then explore along the radial direction, and characterize in the azimuth and vertical submanifolds. This methodology has been successfully tested with two simulations of the effects of a (dynamically young) bar. We have been able to observe and quantify the spatial evolution of the observed moving groups in a large range of about 3 kpc around the sun. Our main results and conclusions are:

- The azimuthal velocity of the moving groups in the radial direction does not follow lines of constant angular momentum, deviating from the naive first order prediction for resonances. In the simulations, resonant structures also deviate from this simple prediction, demanding more complex analytic predictions.
- The spatial evolution of the moving groups is complex. The moving groups configuration observed in the SN is not maintained throughout the disc. The relative position between the arches and their curvature changes across space, and the different moving groups split and merge several times. This is expected in a context of bifurcating orbital families, for example in the case of resonances.

- In our slow bar simulation, we observe a bi-modality created by the OLR in the outer parts of the disc. This bi-modality is also observed in the *Arch/Hat* moving group in the data. This intriguing agreement could favour the slow bar scenario, and opens the possibility of a test with future data.
- The *Acturus*, *Bobylev*, and *Hercules* moving groups present a positive slope of their V_ϕ location with the azimuth. We measure this slope to be $-0.50\,\mathrm{kms^{-1}deg^{-1}}$ at $R = 8\,\mathrm{kpc}$ for *Hercules*.
- The azimuthal velocity of the *Horn*, *Sirius* and *Arch/Hat* moving groups presents an axisymmetrical behaviour. In both our simulations, we observed a small azimuthal gradient in V_ϕ in the Arch/Hat-like structures, although it approches 0 as R increases. This could be related to the young bar model we are using.
- The vertical curvature of the moving groups is similar at the same R. These curvatures are dominated by the gravitational potential to first order, independently of the observed resonance. However, we notice that the *Coma Berenices* group deviates from this behaviour, which points to a different dynamical origin that deserves further investigation.
- In the fast bar simulation, a correlation between $\partial V_\phi/\partial\phi$ and V_R is observed for the OLR trapping region. The region where this correlation is observed in the simulation ($R > 9\,\mathrm{kpc}$, $V_\phi < -170\,\mathrm{kms^{-1}}$) is poorly sampled in Gaia EDR3, but this could potentially be used to give information on the pattern speed of the bar with better data.

Spiral arms, resonances with the bar, accretion events, and possibly other effects can contribute to the present phase space distribution from which we obtain our observables. Disentangling all the contributions of these dynamical processes is hard to address. In this work, we have shown the complexity of the phase-space structure that even a single mechanism (namely the bar) can produce. Our methodology allows to extract a quantitative and robust measurement of the observed phase space substructure that can be then compared and/or fit to different models.

In this paper, we have developed the methodology for the study of the disc with Gaia data, and its formulation is easily generalizable. The same approach can be exported to other substructures in astrophysics (e.g. blind search for streams and shells in the halo) and even datasets outside this field.

In the following months, Gaia DR3 will revolutionize once again our field of research. The new 6D sample will contain about 33M stars, covering a significantly larger region of the disc. With this work, we are ready to process this new data and extract its full potential.

Acknowledgements. This work has made use of data from the European Space Agency (ESA) mission *Gaia* (`https://www.cosmos.esa.int/gaia`), processed by the *Gaia* Data Processing and Analysis Consortium (DPAC, `https://www.cosmos.esa.int/web/gaia/dpac/consortium`). Funding for the DPAC has been provided by national institutions, in particular the institutions participating in the *Gaia* Multilateral Agreement. This work was (partially) funded by the Spanish MICIN/AEI/10.13039/501100011033 and by "ERDF A way of making Europe" by the "European Union" through grant RTI2018-095076-B-C21, and the Institute of Cosmos Sciences University of Barcelona (ICCUB, Unidad de Excelencia 'María de Maeztu') through grant CEX2019-000918-M. MB acknowledges funding from the University of Barcelona's official doctoral program for the development of a R+D+i project under the PREDOCS-UB grant. TA acknowledges the grant RYC2018-025968-I funded by MCIN/AEI/10.13039/501100011033 and by "ESF Investing in your future". BF, GM and PR acknowledge funding from the Agence Nationale de la Recherche (ANR project ANR-18-CE31-0006 and ANR-19-CE31- 0017) and from the European Research Council (ERC) under the European Union's Horizon 2020 research and innovation programme (grant agreement No. 834148).

References

Al Kazwini, H., Agobert, Q., Siebert, A., et al. 2022, A&A, 658, A50
Allen, C. & Santillan, A. 1991, Rev. Mexicana Astron. Astrofis., 22, 255
Antoja, T., Figueras, F., Fernández, D., & Torra, J. 2008, A&A, 490, 135
Antoja, T., Figueras, F., Romero-Gómez, M., et al. 2011, MNRAS, 418, 1423
Antoja, T., Helmi, A., Dehnen, W., et al. 2014, A&A, 563, A60
Antoja, T., Helmi, A., Romero-Gómez, M., et al. 2018, Nature, 561, 360
Bailer-Jones, C. A. L., Rybizki, J., Fouesneau, M., Demleitner, M., & Andrae, R. 2021, AJ, 161, 147
Bennett, M. & Bovy, J. 2019, MNRAS, 482, 1417
Binney, J. 2018, MNRAS, 474, 2706
Bland-Hawthorn, J. & Gerhard, O. 2016, ARA&A, 54, 529
Bovy, J. 2010, ApJ, 725, 1676
Brown, A. G. 2019, The Gaia Universe, 18
Chereul, E., Crézé, M., & Bienaymé, O. 1999, A&AS, 135, 5
Chiba, R., Friske, J. K. S., & Schönrich, R. 2021, MNRAS, 500, 4710
Contardo, G., Hogg, D. W., Hunt, J. A. S., Peek, J. E. G., & Chen, Y.-C. 2022, arXiv e-prints, arXiv:2201.10674
Dehnen, W. 2000, AJ, 119, 800
Dehnen, W. & Binney, J. J. 1998, MNRAS, 298, 387
Du, P., Kibbe, W. A., & Lin, S. M. 2006, Bioinformatics, 22, 2059
Famaey, B., Jorissen, A., Luri, X., et al. 2005, A&A, 430, 165
Ferrers, N. 1877, QJ Pure Appl. Math, 14, 1
Fragkoudi, F., Katz, D., Trick, W., et al. 2019, MNRAS, 488, 3324
Fux, R. 2001, A&A, 373, 511
Gaia Collaboration, Antoja, T., McMillan, P. J., et al. 2021a, A&A, 649, A8
Gaia Collaboration, Brown, A. G. A., Vallenari, A., et al. 2018a, A&A, 616, A1
Gaia Collaboration, Brown, A. G. A., Vallenari, A., et al. 2021b, A&A, 649, A1
Gaia Collaboration, Katz, D., Antoja, T., et al. 2018b, A&A, 616, A11
Gómez, F. A., Minchev, I., Villalobos, Á., O'Shea, B. W., & Williams, M. E. K. 2012, MNRAS, 419, 2163
Gravity Collaboration, Abuter, R., Amorim, A., et al. 2019, A&A, 625, L10
Hunt, J. A. S., Bovy, J., Pérez-Villegas, A., et al. 2018a, MNRAS, 474, 95
Hunt, J. A. S., Hong, J., Bovy, J., Kawata, D., & Grand, R. J. J. 2018b, MNRAS, 481, 3794
Kalnajs, A. J. 1991, 323
Kawata, D., Baba, J., Ciucă, I., et al. 2018, MNRAS, 479, L108
Khanna, S., Sharma, S., Tepper-Garcia, T., et al. 2019, MNRAS, 489, 4962
Laporte, C. F. P., Famaey, B., Monari, G., et al. 2020, A&A, 643, L3
Laporte, C. F. P., Minchev, I., Johnston, K. V., & Gómez, F. A. 2019, MNRAS, 485, 3134
Minchev, I., Quillen, A. C., Williams, M., et al. 2009, MNRAS, 396, L56
Monari, G., Famaey, B., Minchev, I., et al. 2018, Research Notes of the American Astronomical Society, 2, 32
Monari, G., Famaey, B., Siebert, A., et al. 2019a, A&A, 632, A107
Monari, G., Famaey, B., Siebert, A., Wegg, C., & Gerhard, O. 2019b, A&A, 626, A41
Moore, E. F. 1959, in Proc. Int. Symp. Switching Theory, 1959, 285–292
Pérez-Villegas, A., Portail, M., Wegg, C., & Gerhard, O. 2017, ApJ, 840, L2
Portail, M., Gerhard, O., Wegg, C., & Ness, M. 2017, MNRAS, 465, 1621
Quillen, A. C., Carrillo, I., Anders, F., et al. 2018a, MNRAS, 480, 3132
Quillen, A. C., De Silva, G., Sharma, S., et al. 2018b, MNRAS, 478, 228
Ramos, P., Antoja, T., & Figueras, F. 2018, A&A, 619, A72
Reid, M. J. & Brunthaler, A. 2020, ApJ, 892, 39
Romero-Gómez, M., Figueras, F., Antoja, T., Abedi, H., & Aguilar, L. 2015, MNRAS, 447, 218
Schönrich, R., Binney, J., & Dehnen, W. 2010, MNRAS, 403, 1829
Seabroke, G. M., Fabricius, C., Teyssier, D., et al. 2021, A&A, 653, A160
Sellwood, J. A. 2010, MNRAS, 409, 145
Skuljan, J., Hearnshaw, J. B., & Cottrell, P. L. 1999, MNRAS, 308, 731
Sormani, M. C., Gerhard, O., Portail, M., Vasiliev, E., & Clarke, J. 2022, arXiv e-prints, arXiv:2204.13114
Starck, J.-L. & Murtagh, F. 2002
Torra, F., Castañeda, J., Fabricius, C., et al. 2021, A&A, 649, A10
Trick, W. H., Fragkoudi, F., Hunt, J. A. S., Mackereth, J. T., & White, S. D. M. 2021, MNRAS, 500, 2645
Virtanen, P., Gommers, R., Oliphant, T. E., et al. 2020, Nature Methods, 17, 261
Weinberg, M. D. 1994, ApJ, 420, 597

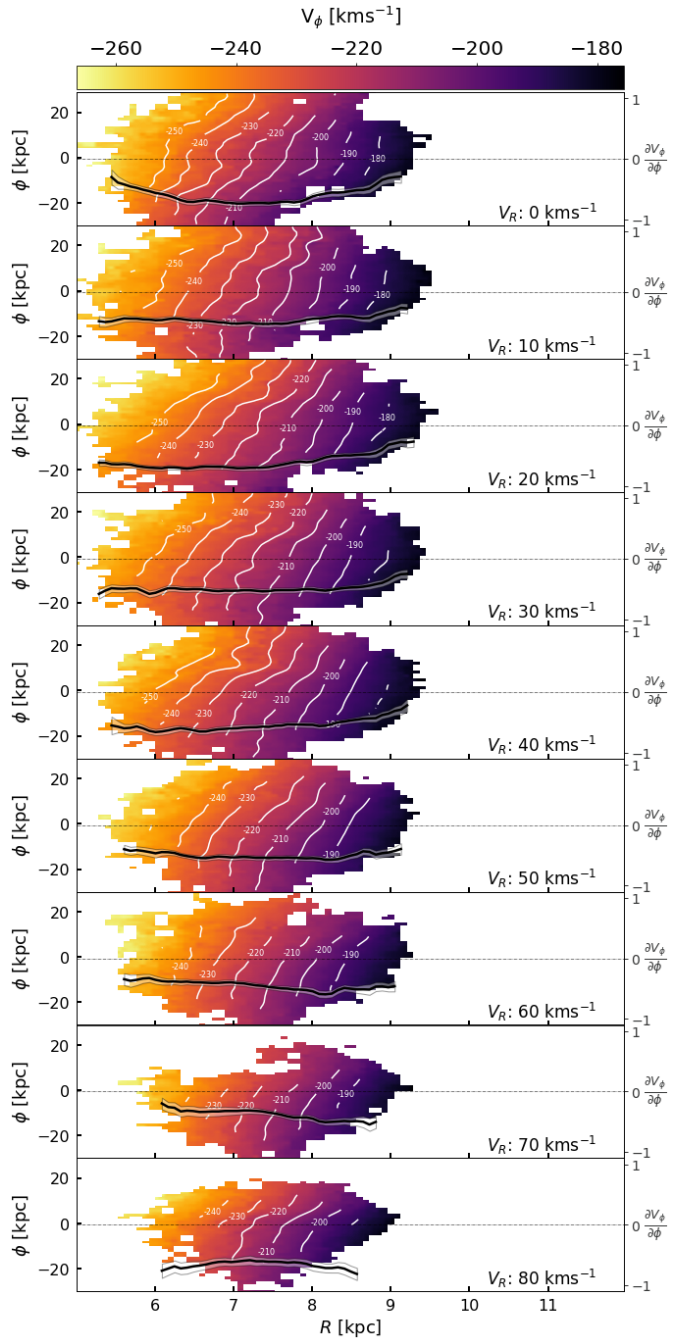

Fig. A.1. Mean azimuthal velocity of the groups in *Hercules* in the $R-\phi$ projection, for $|Z| < 0.2$ kpc. In white, the contours of regions with the same velocity are shown for clarity. In black, the slope of the linear fitting (ϕ, V_ϕ) is shown for every R column, in units of [kms^{-1}deg^{-1}]. The 3σ error of the slope is shown in a translucent region around the line. The group has the same slope at all V_R. This corresponds to a vertical displacement of the moving group in the V_R-V_ϕ diagram.

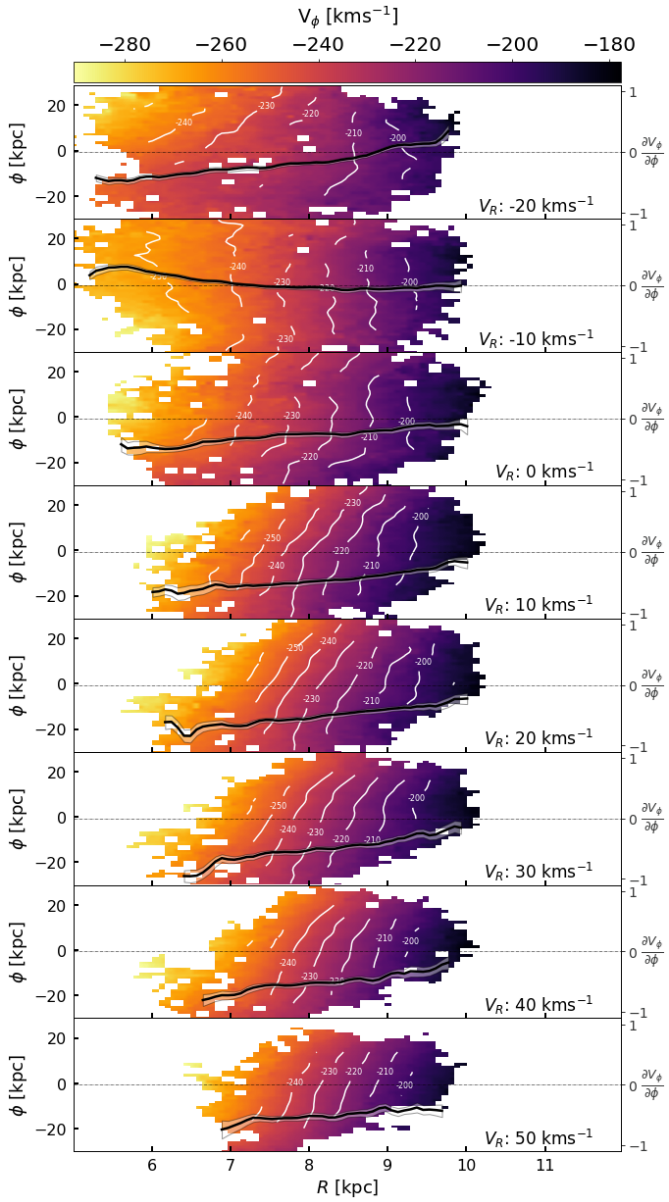

Fig. A.2. Mean azimuthal velocity of the groups in *Hyades* in the $R-\phi$ projection, for $|Z| < 0.2$ kpc. Analogus to Fig. A.1.

Appendix A: Azimuth submanifold along a group

In Figure 3 we show the azimuth submanifold of a representative for each group. In this appendix, we extend this analysis and show how each part of *Hercules* and *Hyades* arches is evolving. In addition, since we have already shown these plots we include the extra information on the slope of V_ϕ in azimuth at each radius. With it, we can compare this groups to the resonances studied in the simulations (Figs. 7 and 8).

The *Hercules* moving group (Fig. A.1) presents a stable and constant slope of V_ϕ in azimuth at the centre of the sample ($R = [6.5, 8]$ kpc). In the limits of the sample, where the significance of the group is smaller compared to the sample, this slope tends to flatten for the regions with $V_R \approx 0$ and to become more steep in the large V_R parts of the arch.

The *Hyades* moving group (Fig. A.2) also presents a stable behaviour at all V_R. In the negative V_R end of the arch (top two rows in the figure) the group has a very low significance, thus leading to a noisy detection.

Appendix B: Extra projections of the simulations

It is the first time that a simulation is studied using the projection shown in Fig. 6. In general, these studies are done in projections of $\langle V_R \rangle$. In order to compare both results, in Fig. B.1 we show this projection for the simulation.

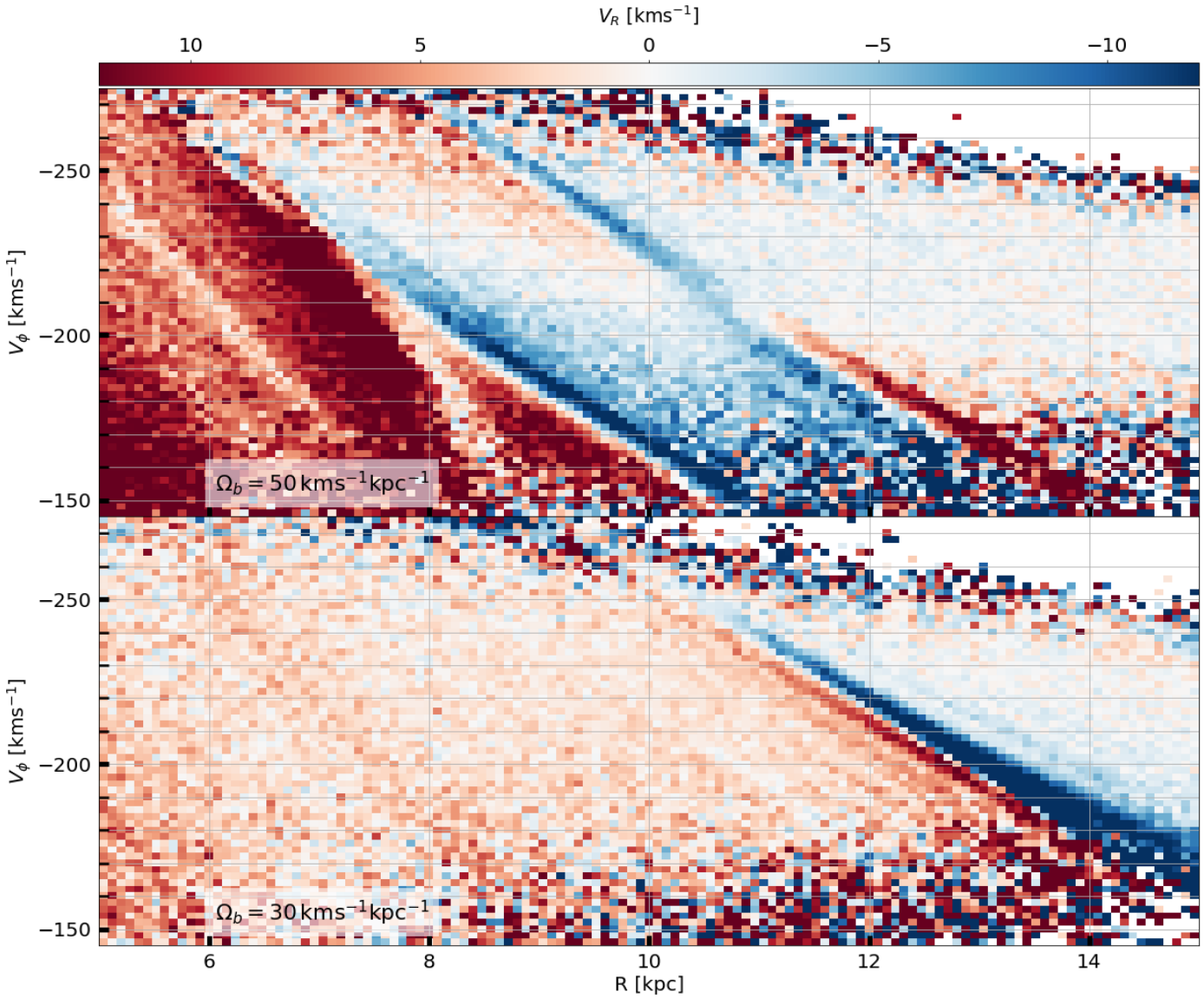

Fig. B.1. Mean radial velocity of the kinematic substructures in the radial direction (ϕ = 0º, Z = 0 kpc) for the test particle simulations, as a function of the radius, and the azimuthal velocity. Top: Fast bar simulation. Bottom: Slow bar simulation.

In the top panel of Fig. B.1, in red, we see the Hercules-like overdensity, which steeply decreases in V_ϕ around R = 8 kpc. The upper part of the OLR bi-modality continues to decrease in a less steep trend, with negative $\langle V_R \rangle$ values on top and negatives in the bottom of the resonance. Finally, in the outer part of the disc we observe the effect of the 1:1 resonance, which shows a swap in $\langle V_R \rangle$ sign when crossing the rotation curve.

As for the bottom panel of Fig. B.1, co-rotation should appear at R = 7.3 kpc, but we can not see any significant structure in this region. In the outer parts of the disc we do observe the OLR placed at 12.2 kpc. Bottom: Fast bar simulation. We observe a lot more substructure. CR (R_{CR} = 4.3 kpc) can be seen as a stripe at inner radius, although not significant enough to be detected by our methodology. At solar radius, we observe the effect of the OLR (R_{OLR} = 7.6 kpc).

Chapter 9

Conclusions

In this thesis, we proposed an accurate way to determine the DF of the Galactic disc perturbed to linear order by a non-axisymmetric perturbation, using a more accurate action-angle coordinate system than in previous similar works.

First, we used the torus mapping from `AGAMA` to numerically compute the perturbing potential in action-angle coordinates as a Fourier series expansion over the angles. We showed that we could estimate typical non-axisymmetric perturbing potentials with an accuracy at the per cent level. The algorithm can be applied to any perturbing potential, including non-plane symmetric vertical perturbations, which will be particularly important when studying the vertical perturbations of the disc with similar methods (Rozier et al., in prep.).

We then computed the DF perturbed to linear order by a typical bar or spiral potential (or a linear combination of both), and computed the local stellar velocity distribution by converting velocities to actions and angles through the Stäckel fudge implemented in `AGAMA`. The results were compared to those obtained by using the epicyclic approximation. The linear deformation due to the bar is generally stronger in the `AGAMA` case, and that due to the spiral is weaker in the `AGAMA` case. This means that reproducing the effect of spiral arms on the local velocity distribution might require a higher amplitude when considering an accurate estimate of the action-angle variables rather than the epicyclic approximation. Most importantly, the epicyclic approximation is inadequate at large heights and does not change the azimuthal velocity location of the resonances due to the hypothesis of complete decoupling of vertical motions. In the `AGAMA` case instead, the locations of resonances are displaced to lower azimuthal v at larger heights. With the background potential used in this paper, we found a displacement in v of 8 $\mathrm{kms}^{-1}\mathrm{kpc}^{-1}$ for the corotation, 6 $\mathrm{kms}^{-1}\mathrm{kpc}^{-1}$ for the OLR and 4 $\mathrm{kms}^{-1}\mathrm{kpc}^{-1}$ for the $1:1$ resonance. Thus, the position of moving groups in the uv-plane as a function of z can be a powerful way to constrain the 3D structure of the Galactic potential. The key to exploring this will be the DR3 of Gaia (Brown, 2019) with its $\sim$ 35 million radial velocities allowing us to better probe the z-axis above and below the Milky Way plane.

The temporal treatment is also an improvement over M16. We applied it to the case of a bar of growing amplitude, with an analytic evolution of the amplitude. As the bar progressively grows, the two linear modes in the DF separate, and lead to a velocity plane already very much resembling the stationary form of the perturbed DF once the perturbation is half-formed. In the absence of a pattern speed variation, it is therefore not necessarily obvious to disentangle the effect of a bar whose amplitude is growing from that of a fully formed bar with larger and constant amplitude. We explored here a peculiar form of the growth function motivated by its analytic

simplicity. If the perturbation grows by linear instability, exponential growth will be more realistic. Numerical experiments are usually well fitted by a logistic function (exponential growth at the beginning and saturation to the plateau). One problem for our treatment is that the logistic function is never strictly equal to 0. In addition, there is hope that similar analytical simplifications such as those for the amplitude growth studied here can also be made with this function, which we will investigate in the future.

While the form of the DF is not well estimated in the resonant zones with the linear perturbations presented above, the signature of the resonances (and thus their location in velocity space) can clearly be identified with this linear perturbation method. The more rigorous approach is to treat the DF with a method like that of Monari et al. (2017a) in these regions, patching these results over the linear deformation computed here. As a first step, by adapting that method to compute the response in space of trapped orbital velocities to a resonance of the bar and replacing the epicyclic approximation with the Stäckel method using AGAMA, we were able in principle to obtain a more accurate outline of the deformation of the distribution function in the resonant zones.

Another caveat is that the torus mapping was used to express the perturbing potential in actions and angles, but for the estimate of the local stellar velocity field, we made use of the less precise Stäckel fudge method. Therefore, another promising way for improvement would be to use the new `ACTIONFINDER` deep-learning algorithm (Ibata et al., 2021) to make the reverse transformation. Finally, these results were obtained in 3D action and velocity spaces, and were mostly presented in 2D slices: it would therefore be particularly useful to improve our algorithm by including a marginalization over any axis, for instance marginalizing over vertical velocities. This is computationally more intensive but should not, a priori, pose any conceptual problem.

Finally, we were able to predict radial velocity maps of stars in the disc of the Galaxy in the presence of a bar using backwards orbit integrations, to be compared to the Gaia data. Even if the median radial velocity maps are not a priori consistent with the data, it should be noted that only the perturbation caused by the bar is taken into account. By adding a spiral, in principle the results can be improved, which will be the topic of further works.

Bibliography

Abuter, R. et al. (May 2019). "A geometric distance measurement to the Galactic center black hole with 0.3% uncertainty". In: *Astronomy and Astrophysics* 625. URL: https://www.aanda.org/articles/aa/full_html/2019/05/aa35656-19/aa35656-19.html.

Antoja, T. et al. (2018). "A dynamically young and perturbed Milky Way disk". In: 561.7723, pp. 360–362. DOI: 10.1038/s41586-018-0510-7. arXiv: 1804.10196 [astro-ph.GA].

Bensby, T. et al. (June 2011). "A First Constraint on the Thick Disk Scale Length: Differential Radial Abundances in K Giants at Galactocentric Radii 4, 8, and 12 kpc". In: *The Astrophysical Journal Letters* 735. URL: https://iopscience.iop.org/article/10.1088/2041-8205/735/2/L46/meta.

Binney, J. and T. Piffl (2015). "The distribution function of the Galaxy's dark halo". In: 454.4, pp. 3653–3663. DOI: 10.1093/mnras/stv2225. arXiv: 1509.06877 [astro-ph.GA].

Binney, James (Oct. 2012). "Actions for axisymmetric potentials". In: 426.2, pp. 1324–1327. DOI: 10.1111/j.1365-2966.2012.21757.x. arXiv: 1207.4910 [astro-ph.GA].

— (May 2020a). "Angle-action variables for orbits trapped at a Lindblad resonance". In: 495.1, pp. 886–894. DOI: 10.1093/mnras/staa092. arXiv: 1912.07026 [astro-ph.GA].

— (May 2020b). "Trapped orbits and solar-neighbourhood kinematics". In: 495.1, pp. 895–904. DOI: 10.1093/mnras/staa1103. arXiv: 1912.07023 [astro-ph.GA].

Binney, James and Paul McMillan (2011). "Models of our Galaxy - II". In: 413.3, pp. 1889–1898. DOI: 10.1111/j.1365-2966.2011.18268.x. arXiv: 1101.0747 [astro-ph.GA].

Binney, James and Paul J. McMillan (2016). "Torus mapper: a code for dynamical models of galaxies". In: 456.2, pp. 1982–1998. DOI: 10.1093/mnras/stv2734. arXiv: 1511.07754 [astro-ph.GA].

Binney, James and Ralph Schönrich (2018). "The origin of the Gaia phase-plane spiral". In: 481.2, pp. 1501–1506. DOI: 10.1093/mnras/sty2378. arXiv: 1807.09819 [astro-ph.GA].

Binney, James and Scott Tremaine (2008). *Galactic Dynamics: Second Edition*. Princeton University Press.

Bland-Hawthorn, Joss and Thor Tepper-García (July 2021). "Galactic seismology: the evolving 'phase spiral' after the Sagittarius dwarf impact". In: 504.3, pp. 3168–3186. DOI: 10.1093/mnras/stab704. arXiv: 2009.02434 [astro-ph.GA].

Blitz, L., M. Fich, and A. A. Stark (June 1982). "Catalogue of CO radial velocities toward galactic HII regions." In: *Astrophysical Journal, Suppl. Ser.* 49. URL: https://ui.adsabs.harvard.edu/abs/1982ApJS...49..183B/abstract.

Brown, Anthony G. A. (Apr. 2019). "The Future of the Gaia Universe". In: *The Gaia Universe*, 18, p. 18. DOI: 10.5281/zenodo.2637972.

Burton, W. B. and M. A. Gordon (Feb. 1978). "Carbon monoxide in the Galaxy. III. The overall nature of its distribution in the equatorial plane." In: *Astronomy and Astrophysics* 63. URL: https://ui.adsabs.harvard.edu/abs/1978A%26A....63....7B/abstract.

Carollo, D. et al. (Mar. 2010). "Structure and kinematics of the stellar halo and thick disks of the Milky Way based on calibration from Sloan Digital Sky Survey DR7". In: *The Astrophysical Journal* 712. URL: https://iopscience.iop.org/article/10.1088/0004-637X/712/1/692.

Clemens, D. P. (Aug. 1985). "Massachusetts–Stony Brook Galactic Plane CO Survey: The Galactic Disk Rotation Curve". In: *The Astrophysical Journal* 295. URL: https://people.bu.edu/clemens/publications/clemens_1985.pdf.

Cole, D. R. and James Binney (2017). "A centrally heated dark halo for our Galaxy". In: 465.1, pp. 798–810. DOI: 10.1093/mnras/stw2775. arXiv: 1610.07818 [astro-ph.GA].

Cooper, A. P. et al. (Aug. 2010). "Galactic stellar haloes in the CDM model". In: *MNRAS* 406. URL: https://ui.adsabs.harvard.edu/abs/2010MNRAS.406..744C/abstract.

Cox, Donald P. and Gilberto C. Gómez (2002). "Analytical Expressions for Spiral Arm Gravitational Potential and Density". In: 142.2, pp. 261–267. DOI: 10.1086/341946. arXiv: astro-ph/0207635 [astro-ph].

Deason, A. J. et al. (May 2019). "The local high velocity tail and the Galactic escape speed." In: *MNRAS* 485. URL: https://ui.adsabs.harvard.edu/abs/2019MNRAS.485.3514D/abstract.

Dehnen, Walter (June 1998). "The Distribution of Nearby Stars in Velocity Space Inferred from HIPPARCOS Data". In: 115.6, pp. 2384–2396. DOI: 10.1086/300364. arXiv: astro-ph/9803110 [astro-ph].

— (2000). "The Effect of the Outer Lindblad Resonance of the Galactic Bar on the Local Stellar Velocity Distribution". In: 119.2, pp. 800–812. DOI: 10.1086/301226. arXiv: astro-ph/9911161 [astro-ph].

Demers, S. and P. Battinelli (July 2007). "C stars as kinematic probes of the Milky Way disk from 9 to 15 kpc*". In: *Astronomy and Astrophysics* 473. URL: https://www.aanda.org/articles/aa/abs/2007/37/aa7691-07/aa7691-07.html.

D'Onghia, E. and J. A. L. Aguerri (Feb. 2020). "Trojans in the Solar Neighborhood". In: *The Astrophysical Journal* 890. URL: https://ui.adsabs.harvard.edu/abs/2020ApJ...890..117D/abstract.

Drimmel, R. (June 2000). "Evidence for a two-armed spiral in the Milky Way". In: *Astronomy and Astrophysics* 358. URL: https://ui.adsabs.harvard.edu/abs/2000A%26A...358L..13D/abstract.

Famaey, B. and H. Dejonghe (2003). "Three-component Stäckel potentials satisfying recent estimates of Milky Way parameters". In: 340.3, pp. 752–762. DOI: 10.1046/j.1365-8711.2003.06322.x. arXiv: astro-ph/0212059 [astro-ph].

Famaey, B. et al. (Jan. 2005). "Local kinematics of K and M giants from CORAVEL/Hipparcos/Tycho-2 data. Revisiting the concept of superclusters". In: 430, pp. 165–186. DOI: 10.1051/0004-6361:20041272. arXiv: astro-ph/0409579 [astro-ph].

Famaey, Benoit and Stacy S. McGaugh (2012). *Modified Newtonian Dynamics (MOND): Observational Phenomenology and Relativistic Extensions*. Living Reviews in Relativity.

Fich, M., L. Blitz, and A. A. Stark (July 1989). "The Rotation Curve of the Milky Way to 2R 0". In: *Astrophysical Journal* 342. URL: https://ui.adsabs.harvard.edu/abs/1989ApJ...342..272F/abstract.

Fragkoudi, F. et al. (Sept. 2019). "On the ridges, undulations, and streams in Gaia DR2: linking the topography of phase space to the orbital structure of an N-body bar". In: 488.3, pp. 3324–3339. DOI: 10.1093/mnras/stz1875. arXiv: 1901.07568 [astro-ph.GA].

Gaia Collaboration et al. (2018a). "Gaia Data Release 2. Mapping the Milky Way disc kinematics". In: 616, A11, A11. DOI: 10.1051/0004-6361/201832865. arXiv: 1804.09380 [astro-ph.GA].

Gaia Collaboration et al. (Aug. 2018b). "Gaia Data Release 2. Summary of the contents and survey properties". In: 616, A1, A1. DOI: 10.1051/0004-6361/201833051. arXiv: 1804.09365 [astro-ph.GA].

Gaia Collaboration et al. (May 2021). "Gaia Early Data Release 3. Summary of the contents and survey properties". In: 649, A1, A1. DOI: 10.1051/0004-6361/202039657. arXiv: 2012.01533 [astro-ph.GA].

Ghez, A. M. et al. (Dec. 2008). "Measuring Distance and Properties of the Milky Way's Central Supermassive Black Hole with Stellar Orbits". In: *The Astrophysical Journal* 689. URL: https://ui.adsabs.harvard.edu/abs/2008ApJ...689.1044G/abstract.

Gilmore, G. and N. Reid (Mar. 1983). "New light on faint stars - III. Galactic structure towards the South Pole and the Galactic thick disc." In: *MNRAS* 202. URL: https://ui.adsabs.harvard.edu/abs/1983MNRAS.202.1025G/abstract.

Gonzalez, O. A. and D. Gadotti (Aug. 2016). "The Milky Way Bulge: Observed Properties and a Comparison to External Galaxies". In: *Galactic Bulges, Astrophysics and Space Science Library* 418. URL: https://ui.adsabs.harvard.edu/abs/2016ASSL..418..199G/abstract.

Gupta, A. et al. (Sept. 2012). "A huge reservoir of ionized gas around the Milky Way: Accounting for the Missing Mass?" In: *The Astrophysical Journal Letters* 756. URL: https://ui.adsabs.harvard.edu/abs/2012ApJ...756L...8G/abstract.

Haines, T. et al. (July 2019). "Implications of a Time-varying Galactic Potential for Determinations of the Dynamical Surface Density". In: *The Astrophysical Journal Letters* 879. URL: https://ui.adsabs.harvard.edu/abs/2019ApJ...879L..15H/abstract.

Harris, W. E. (Oct. 1996). "A Catalog of Parameters for Globular Clusters in the Milky Way". In: *Astronomical Journal* 112. URL: https://adsabs.harvard.edu/full/1996AJ....112.1487H.

Haywood, M. et al. (Dec. 2013). "The age structure of stellar populations in the solar vicinity". In: *Astronomy and Astrophysics* 560. URL: https://www.aanda.org/articles/aa/full_html/2013/12/aa21397-13/aa21397-13.html.

Helmi, A. et al. (Oct. 2018). "The merger that led to the formation of the Milky Way's inner stellar halo and thick disk". In: *Nature* 563. URL: https://ui.adsabs.harvard.edu/abs/2018Natur.563...85H/abstract.

Honma, M. and Y. Sofue (Aug. 1997a). "Rotation Curve of the Galaxy". In: *Publications of the Astronomical Society of Japan* 49. URL: https://ui.adsabs.harvard.edu/abs/1997PASJ...49..453H/abstract.

— (Aug. 1997b). "On the Keplerian Rotation Curves of Galaxies". In: *Publications of the Astronomical Society of Japan* 49. URL: https://academic.oup.comâĂžpasjâĂž49âĂž539âĂžpasj49-0539.

Honma, M. et al. (Oct. 2007). "Astrometry of Galactic Star-Forming Region Sharpless 269 with VERA: Parallax Measurements and Constraint on Outer Rotation Curve". In: *Publications of the Astronomical Society of Japan* 59. URL: https://academic.oup.com/pasj/article/59/5/889/2898125.

Hou, L. G. and J. L. Han (Sept. 2015). "Offset between stellar spiral arms and gas arms of the Milky Way". In: *MNRAS*. URL: https://academic.oup.com/mnras/article/454/1/626/1122941.

Hubble, E. P. (May 1926a). "A spiral nebula as a stellar system: Messier 33." In: *Astrophysical Journal* 63. URL: https://ui.adsabs.harvard.edu/abs/1926ApJ....63..236H/abstract.

— (Dec. 1926b). "Extra-galactic nebulae". In: *Astrophysical Journal* 64. URL: https://ui.adsabs.harvard.edu/abs/1926ApJ....64..321H/abstract.

Ibata, Rodrigo et al. (July 2021). "The ACTIONFINDER: An Unsupervised Deep Learning Algorithm for Calculating Actions and the Acceleration Field from a Set of Orbit Segments". In: 915.1, 5, p. 5. DOI: 10.3847/1538-4357/abfda9. arXiv: 2012.05250 [astro-ph.GA].

Laird, J. B. et al. (Sept. 1988). "A survey of proper-motion stars. VII-The halo metallicity distribution function". In: *Astronomical Journal* 96. URL: https://adsabs.harvard.edu/pdf/1988AJ.....96.1908L.

Laporte, Chervin F. P. et al. (May 2019). "Footprints of the Sagittarius dwarf galaxy in the Gaia data set". In: 485.3, pp. 3134–3152. DOI: 10.1093/mnras/stz583. arXiv: 1808.00451 [astro-ph.GA].

Laporte, Chervin F. P. et al. (Nov. 2020). "Bar resonances and low angular momentum moving groups in the Galaxy revealed by their stellar ages". In: 643, L3, p. L3. DOI: 10.1051/0004-6361/202038740. arXiv: 2006.13876 [astro-ph.GA].

Lucchini, S. et al. (June 2022). "Moving Groups Across Galactocentric Radius with Gaia DR3". In: *eprint arXiv:2206.10633*. URL: arXiv:2206.10633.

Malhan, K. et al. (Feb. 2022). "The Global Dynamical Atlas of the Milky Way Mergers: Constraints from Gaia EDR3-based Orbits of Globular Clusters, Stellar Streams, and Satellite Galaxies". In: *The Astrophysical Journal* 926. URL: https://ui.adsabs.harvard.edu/abs/2022ApJ...926..107M/abstract.

Matteo, P. Di et al. (Dec. 2019). "The Milky Way has no in-situ halo other than the heated thick disc. Composition of the stellar halo and age-dating the last significant merger with Gaia DR2 and APOGEE". In: *Astronomy Astrophysics* 632.

URL: https://ui.adsabs.harvard.edu/abs/2019A%26A...632A...4D/abstract.

McCarthy, I. G. et al. (Mar. 2012). "Global structure and kinematics of stellar haloes in cosmological hydrodynamic simulations". In: *MNRAS* 420. URL: https://academic.oup.com/mnras/article/420/3/2245/979122?login=true.

McGill, Colin and James Binney (1990). "Torus construction in general gravitational potentials". In: 244, pp. 634–645.

McMillan, P. J. (Feb. 2017). "The mass distribution and gravitational potential of the Milky Way". In: *MNRAS* 465. URL: https://academic.oup.com/mnras/article/465/1/76/2417479.

Minchev, I., J. Nordhaus, and A. C. Quillen (July 2007). "New Constraints on the Galactic Bar". In: 664.1, pp. L31–L34. DOI: 10.1086/520578. arXiv: astro-ph/0703805 [astro-ph].

Minchev, I. et al. (June 2009). "Is the Milky Way ringing? The hunt for high-velocity streams". In: *MNRAS* 396. URL: https://academic.oup.com/mnrasl/article/396/1/L56/980043.

Monari, G., B. Famaey, and A. Siebert (Apr. 2016). "Modelling the Galactic disc: perturbed distribution functions in the presence of spiral arms". In: 457, pp. 2569–2582. DOI: 10.1093/mnras/stw171. arXiv: 1601.04714.

Monari, G. et al. (Aug. 2018). "The escape speed curve of the Galaxy obtained from Gaia DR2 implies a heavy Milky Way". In: *Astronomy Astrophysics* 616. URL: https://ui.adsabs.harvard.edu/abs/2018A%26A...616L...9M/abstract.

Monari, G. et al. (June 2019a). "Signatures of the resonances of a large Galactic bar in local velocity space". In: 626, A41, A41. DOI: 10.1051/0004-6361/201834820. arXiv: 1812.04151 [astro-ph.GA].

Monari, G. et al. (Dec. 2019b). "Tracing Hercules in Galactic azimuth with Gaia DR2". In: 632, A107, A107. DOI: 10.1051/0004-6361/201936455. arXiv: 1908.01318 [astro-ph.GA].

Monari, Giacomo et al. (2017a). "Distribution functions for resonantly trapped orbits in the Galactic disc". In: 471.4, pp. 4314–4322. DOI: 10.1093/mnras/stx1825. arXiv: 1707.05306 [astro-ph.GA].

Monari, Giacomo et al. (Feb. 2017b). "Staying away from the bar: the local dynamical signature of slow and fast bars in the Milky Way". In: 465.2, pp. 1443–1453. DOI: 10.1093/mnras/stw2807. arXiv: 1609.02557 [astro-ph.GA].

Naidu, R. P. et al. (Sept. 2020). "Evidence from the H3 Survey That the Stellar Halo Is Entirely Comprised of Substructure". In: *The Astrophysical Journal* 901. URL: https://ui.adsabs.harvard.edu/abs/2020ApJ...901...48N/abstract.

Peñarrubia, J. et al. (Sept. 2014). "A dynamical model of the local cosmic expansion." In: *MNRAS* 443. URL: https://academic.oup.com/mnras/article/443/3/2204/1751478.

Poggio, E. et al. (Nov. 2021). "Measuring the vertical response of the Galactic disc to an infalling satellite". In: *MNRAS* 508. URL: https://ui.adsabs.harvard.edu/abs/2021MNRAS.508..541P/abstract.

Portail, M. et al. (Nov. 2016). "Dynamical modelling of the galactic bulge and bar: the Milky Way's pattern speed, stellar and dark matter mass distribution". In:

MNRAS 465. URL: https://academic.oup.com/mnras/article/465/2/1621/2417047.

Portail, M. et al. (Feb. 2017). "Dynamical modelling of the Galactic bulge and bar: the Milky Way's bar pattern speed, stellar, and dark matter mass distribution". In: *MNRAS* 465. URL: https://academic.oup.com/mnras/article/465/2/1621/2417047.

Pouliasis, E., P. Di Matteo, and M. Haywood (Feb. 2017). "A Milky Way with a massive, centrally concentrated thick disc: new Galactic mass models for orbit computations". In: *Astronomy and Astrophysics* 598. URL: https://www.aanda.org/articles/aa/full_html/2017/02/aa27346-15/aa27346-15.html.

Press, William H. et al. (1992). *Numerical Recipes in C: Second Edition*. Cambridge University Press.

Ramos, P., T. Antoja, and F. Figueras (Nov. 2018). "Riding the kinematic waves in the Milky Way disk with Gaia". In: 619, A72, A72. DOI: 10.1051/0004-6361/201833494. arXiv: 1805.09790 [astro-ph.GA].

Recio-Blanco, A. et al. (July 2014). "The Gaia-ESO Survey: the Galactic Thick to Thin Disc transition". In: *Astronomy and Astrophysics* 567. URL: https://ui.adsabs.harvard.edu/abs/2014A%26A...567A...5R/abstract.

Robin, A.C. et al. (Sept. 2014). "Constraining the thick disc formation scenario of the Milky Way". In: *Astronomy and Astrophysics* 569. URL: https://www.aanda.org/articles/aa/abs/2014/09/aa23415-14/aa23415-14.html.

Sanders, Jason L. and James Binney (2016). "A review of action estimation methods for galactic dynamics". In: 457.2, pp. 2107–2121. DOI: 10.1093/mnras/stw106. arXiv: 1511.08213 [astro-ph.GA].

Seabroke, G. M. and G. Gilmore (Sept. 2007). "Revisiting the relations: Galactic thin disc age–velocity dispersion relation". In: *MNRAS* 380. URL: https://onlinelibrary.wiley.com/doi/abs/10.1111/j.1365-2966.2007.12210.x.

Sofue, Y., M. Honma, and T. Omodaka (Feb. 2009). "Unified Rotation Curve of the Galaxy – Decomposition into de Vaucouleurs Bulge, Disk, Dark Halo, and the 9-kpc Rotation Dip –". In: *Publications of the Astronomical Society of Japan* 61. URL: https://ui.adsabs.harvard.edu/abs/2009PASJ...61..227S/abstract.

Trick, Wilma H., Johanna Coronado, and Hans-Walter Rix (Apr. 2019). "The Galactic disc in action space as seen by Gaia DR2". In: 484.3, pp. 3291–3306. DOI: 10.1093/mnras/stz209. arXiv: 1805.03653 [astro-ph.GA].

Urquhart, J. S. et al. (Nov. 2013). "The RMS survey: galactic distribution of massive star formation". In: *MNRAS* 437. URL: https://academic.oup.com/mnras/article/437/2/1791/1111987?login=true.

Vasiliev, E. (May 2018). *AGAMA: Action-based galaxy modeling framework*. Astrophysics Source Code Library. ascl: 1805.008.

Vasiliev, Eugene (Jan. 2019). "AGAMA: action-based galaxy modelling architecture". In: 482.2, pp. 1525–1544. DOI: 10.1093/mnras/sty2672. arXiv: 1802.08239 [astro-ph.GA].

Vaucouleurs, G. de and W. D. Pence (Oct. 1978). "An outsider's view of the Galaxy: photometric parameters, scale lengths, and absolute magnitudes of the spheroidal

and disk components of our Galaxy." In: *Astronomical Journal* 83. URL: https://ui.adsabs.harvard.edu/abs/1978AJ.....83.1163D/abstract.

Weinberg, Martin D. (1994). "Kinematic Signature of a Rotating Bar near a Resonance". In: 420, p. 597. DOI: 10.1086/173589. arXiv: astro-ph/9304026 [astro-ph].